UNIVERSITÀ DEGLI STUDI DI PARMA

DOTTORATO DI RICERCA IN
SCIENZA E TECNOLOGIA DEI MATERIALI

CICLO XXIX

Self-diagnostic polymers through host-guest interactions

Coordinatore:
Prof. Enrico Dalcanale

Supervisore:
Prof. Enrico Dalcanale

Dottorando: Andreas E. Früh

Anni 2014/2017

This research has been financially supported through the Hierarchical Self Assembly of Polymeric Soft Systems Innovative Training Network (SASSYPOL-ITN) Marie Skłodowska-Curie action, funded through the European Union Seventh Framework Programme (FP7-PEOPLE-2013-ITN) under grant agreement № 607602.

Contents

1 General Introduction

1.1 Supramolecular chemistry

Supramolecular chemistry is defined by the International Union of Pure and Applied Chemistry (IUPAC) as the "field of chemistry related to species of greater complexity than molecules, that are held together and organised by means of intermolecular interactions"[1]. Until very recent, chemistry was the "science of substances: their structure, their properties, and the reactions that change them into other substance"[2]. It was not until the late 1970s, when Jean-Marie Lehn coined the term "supramolecular chemistry" that chemists started to look beyond the molecule, giving birth to a new field of chemistry, which, according to Steed and Atwood in 2000, "everybody's doing [now]"[3].

The first cornerstone of supramolecular chemistry was laid in 1873 by Johannes Diderik van der Waals in his Ph.D. thesis with the postulation of the first noncovalent intermolecular interactions[4], later named the *van der Waals' interactions*, while the first discription of a supramolecular system was made in the 'lock and key hypothesis' by Emil Fischer in 1895.[5] Discovery of other intermolecular forces such as the hydrogen bond[6, 7], the ionic bond[8, 9], dipole-interactions[10, 11] and the π-interactions[12] and Richard P. Feynman's famous 1959 talk *There's plenty of room at the bottom*[13] were other important steps in the formation of the field.

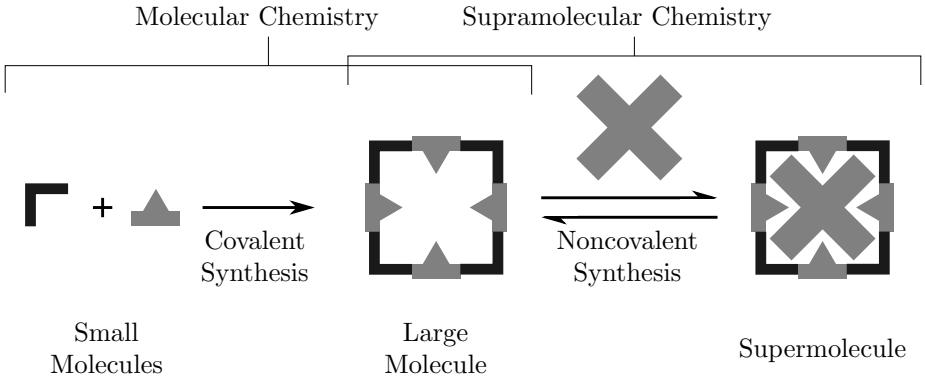

Figure 1: Distinction beween molecular and supramolecular chemistry according to Lehn.[14]

A large part of supramolecular chemistry is dedicated to the binding or complexation of a molecule, called 'host', to another molecule, called 'guest', forming a host-guest complex. While in principle an unlimited number of host-guest complexes are imaginable, only a limited number of hosts has been investigated so far, most of them belonging to the class of macrocycles. Typical examples for host molecules are cryptands[15, 16], cyclodextrins[17–19], calixarenes[20, 21], cavitands[22–26] or cucurbiturils[27–33].

Supramolecular chemistry is a highly interdisciplinary field[3], borrowing techniques not only from chemistry, but from a whole range of other fields such as biochemistry, biology, physics and engineering. Those fields on the other hand profit from the developments of supramolecular chemistry, by developments such as highly specific dyes for biochemistry[34], methods for cell surface functionalisation in biology[35], mediators for solar cell physics[36] or improved materials such as impact resistant epoxys for engineering[37].

1.2 Supramolecular chemistry and polymers

One of the fields benefiting from the developments in supramolecular chemistry is polymers science. In this field, a whole new class of materials, the so called supramolecular polymers, which per definition are "based on monomeric units held together with directional and reversible secondary interactions"[38], has been developed. The most relevant issues for the development of supramolecular polymers are: To achieve macroscopic expression of molecular recognition, to trigger stimuli specific responses in polymeric systems and to move self-assembly from the nano to the meso and macro scale. Beyond this, supramolecular chemistry has also been used to improve the properties of existing, 'classical' polymers, by addition of new interactions.[39] Example for the later are supramolecular block copolymers[40–42], self-healing polymers[43–45], or polymers with vastly improved electronic[46, 47], thermal[48] or other properties.

This thesis focuses on the improvement of existing 'classical' polymers. Part I deals with the development of so called self-diagnostic polymers, *i.e.*, polymers with an intrinsic ability to highlight areas where damage is present or about to develop. Part II demonstrates the use of supramolecular chemistry to compatibilise otherwise immiscible polymers, giving rise to new, formerly inaccessible polymer blends. Furthermore, it has been demonstrated that these interactions can be 'turned off', leading to decompatibilisation and subsequently separation of the blend.

Part I

Self-diagnostic polymers

2 Introduction

Polymers are desirable materials for high-performance applications, due to their affordable price, light weight and processability. However, small damages, which are difficult to detect, can compromise the mechanical integrity of the material and subsequently lead to failure. Molecular probes are ideal candidates to facilitate the detection of such damages and thus to prevent catastrophic failure, visualising mechanical strain and/or damage as an easily detectable alert signal at a very early stage. A range of mechanochemical reporters, based on force induced redistributions of a chemical equilibrium have been published,[49–53] including spiropyran[54–57], and dioxetanes[58–60] based systems. Other systems are based on physical effects such as aggregation or separation-induced emission,[61, 62] alteration of the band gap by physical deformation of single-walled carbon nanotubes (SWCNT),[63, 64] or mechanochromism[65]. However, those methods come with the drawback that relatively large quantities of the active system are needed, which alter the mechanical properties of the polymer and significantly increase the price of the material. For example, probes based on the force induced redistributions of a chemical equilibria add covalent crosslinks to the system. Systems based on physical effects, like the ones for aggregation or separation-induced emission, while relatively sensitive, need specially engineered polymers, in the form of solvent-filled microcapsules or the layering of different materials.

In hydrostatic stress-sensitive materials like soft polymers, the volumetric strain (corresponding physically to the mean strain value obtained by averaging the strain components with respect to all the 3D space directions) is fundamental for their safety level assessment, yet very hard to determine.[66] In such materials, micro voids and inclusions typically exist and the presence of a hydrostatic stress state, which is related to the mean strain value, can lead to an expansion and coalescence of the imperfections (often identified as cavitation-like failure mechanism), triggering the subsequent crack appearance and growth.[67]

The above described mechanism becomes much more relevant in case of materials withstanding repeated loads (fatigue). The capability to monitor the maximum volumetric strain occurred in the element under service enables to optimise the design and to enhance the safety level. As a matter of fact, the direct measure of the average strain is not feasible and the determination of the volumetric strain requires strain measurements in multiple directions, an operation that can be prohibitive in small or thin elements. The availability of a detection tool to identify highly volumetric strained regions without the need of any complex measurement device and without interacting with the microstructure bearing mechanism of the material, would be highly desirable. Further, self-diagnostic capability allowed by molecular interactions (*i.e.*, at the nanoscale level), entails no restrictions on the scale of the element to be analysed and opens the way to the monitoring of objects of any size, spanning from

Parts of this chapter are in preparation for publication: Andreas E. Früh, Federico Artoni, Roberto Brighenti, and Enrico Dalcanale. Strain field self-diagnostic PDMS elastomers. *Advanced Functional Materials*, in preparation.

nano- to meso- and macro-scale applications.

This thesis reports a variety of different self-diagnostic probes, which are able to report areas of high strain in different polymeric matrices by fluorescence turn-on. The proposed reporting principle is sketched in Figure 2. The reporting probes are host-guest complexes, acting as crosslinks, which will be broken preferentially upon mechanical stress. The dissociation of those crosslinks leads to a fluorescence turn-on. Turn-on fluorescence, which is easily detectable with suitable equipment, offers an excellent contrast between affected and unaffected regions, providing a very sensitive tool for the monitoring of structural elements. Since very small quantities of these reporting systems are needed, the physical properties of the resulting self-diagnostic polymers are not altered compared to the pristine material.

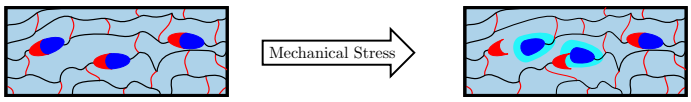

Figure 2: Schematic representation of a self-diagnostic polymer exploiting supramolecular host-guest complexes (shown as red-blue ovals). Mechanical force separates the complexes, restoring the fluorescence which is quenched in the intact complex.

3 Phosphonate cavitands as hosts structures for probes in self-diagnostic epoxy thermosets

3.1 Introduction

Cavitands are programmable abiotic receptors capable of hosting shape complementary guests through specific weak interactions, such as hydrogen bonding, π-π stacking, and CH-π and cation-π interactions. Both the upper and the lower rim of cavitands can be decorated with proper functional groups to modulate the complexation properties, to impart solubility or to graft them on solid surfaces.

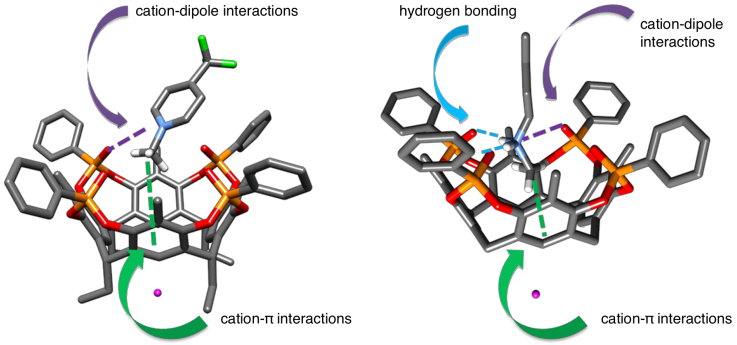

Figure 3: Interactions of tetraphosphonate cavitands with *N*-methyl pyridinium (left) and *N*-methyl ammonium salts (right). Adapted from Reference [68].

In the design of cavitands, the choice of the bridging groups connecting the phenolic hydroxyls of the resorcinarene scaffold is pivotal, since it determines shape, dimensions and complexation properties of the resulting cavity. Tetraphosphonate cavitands, presenting four H-bonding acceptor P=O groups at the upper rim of the cavity, are particularly appealing for the complexation of *N*-methyl pyridinium[68, 69] and *N*-methyl ammonium salts[70] (Figure 3). The presence of P(V) stereocenters brings configurational properties into play, since the relative orientation of the P=O groups with respect to the cavity (inward or outward) determines the number of possible stereoisomers. Figure 4 reports the general structure of tetraphosphonate cavitands with their general acronym below. The first capital letter defines number of the bridges, the second lower case letters define the in-out stereochemistry at each P(V) center, R_1, R_2 and R_3 in brackets define respectively the substituents at the lower rim, in the apical positions and on the P(V) stereocenters. Only the inward facing stereoisomers (i), having the P=O groups pointing toward the cavity, are efficient receptors. A stereoselective procedure for the preparation of in isomers via oxidation of the corresponding P(III) precursors is available.[70]

The presence of 3 different types of substitutes, marked as R_1, R_2 and R_3

in Figure 4, makes tetraphosphonate cavitands highly versatile host structures: modifications of R_2 and R_3 have thereby mainly an impact on the complexation of specific guests, while R_1 can be used to tune solubility, for the incorporation in polymeric matrices[71, 72] or to attach the system on to surfaces.

The origin of the receptor selectivity towards *N*-methyl pyridinium salts, is attributed to the presence of two synergistic interaction modes: (i) $N^+ \bullet\bullet\bullet O{=}P$ cation-dipole interactions; (ii) cation-π interactions of the acidic N^+-CH_3 group with the π basic cavity. It has furthermore been demonstrated that the complexation of a suitable guest has an impact on the fluorescence of the guest[68, 73], making cavitands and interesting platform for the development of a probe for self-diagnostic polymers.

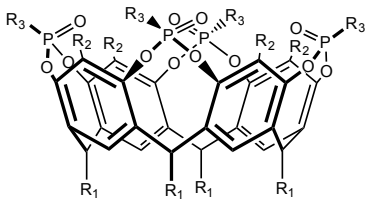

Figure 4: General formula of a tetraphosphonate cavitand Tiiii[R_1,R_2,R_3].

3.2 Ditopic *N*-methylated guests

The incorporation of tetraphosphonate cavitands into the polymer chain followed by supramolecular crosslinking by the ditopic guest is one of the possible ways to obtain self-diagnostic polymers. Compounds shown in Figure 5 are examples of highly fluorescent, ditopic guests, which, thanks to the presence of an aromatic *N*-methyl ammonium salt, are possible guests for tetraphosphonate cavitands.

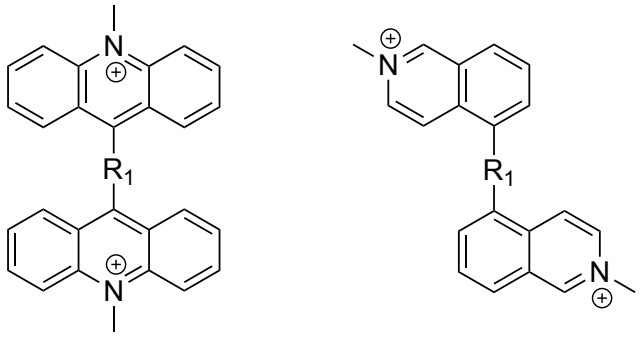

Figure 5: Proposed ditopic guests based on *N*-methylacridinium (left) and *N*-methylisoquinolinium (right) salts.

Wang *et al.* [74] showed that *N*-methylacridinium iodide (shown in Figure 6 top left) can be quenched by supramolecular interactions (in their case by the complexation with a pillar[5]arene). However, as visible in Figure 6 (bottom left), tetraphosphonate cavitand Tiiii[C_3H_7,CH_3,C_2H_5] does not alter the optical properties of *N*-methylacridinium iodide, making it unsuitable as guest for self-diagnostic systems.

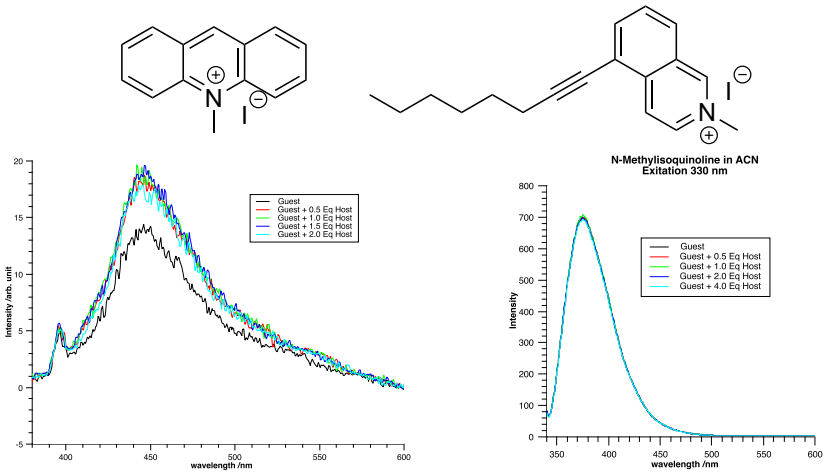

Figure 6: Structures of *N*-methylacridinium iodide (top, left) and *N*-Methyl-5-(oct-1-yn-1-yl)isoquinolin-2-ium iodide (top, right). Titration of *N*-methylacridinium iodide with Tiiii[C_3H_7,CH_3,C_2H_5] ($c = 5 \times 10^{-6}\,\mathrm{mol\,dm^{-3}}$ in dichloromethane (DCM), $\lambda_{ex} = 355\,\mathrm{nm}$) (bottom, left). Titration of *N*-methylisoquinolinium iodide with Tiiii[C_3H_7,CH_3,C_2H_5] ($c = 5 \times 10^{-6}\,\mathrm{mol\,dm^{-3}}$ in acetonitrile (ACN), $\lambda_{ex} = 330\,\mathrm{nm}$) (bottom, right).

Modelling of the system using Spartan[75], results shown in Figure 7, shows that *N*-methylacridinium is, due to the relatively bulky nature of the acridine, not able to enter the cavity with the methyl group, showing therefore only very weak interactions. Based on those findings, the *N*-methylisoquinolinium salt, shown in Figure 6, was used since it can penetrate the cavity deeper and as a result gives rise to more significant interactions. In fact, nuclear magnetic resonance spectroscopy (NMR) titrations, as shown in Figure 6 and Appendix A, showed a strong interaction between *N*-Methyl-5-(oct-1-yn-1-yl)isoquinolin-2-ium iodide and Tiiii[C_3H_7,CH_3,C_2H_5]. In particular, a strong shift is observed for the *N*-methyl group, indicating a deep penetration of the guest into the cavity of the host, as shown on the right side of Figure 7. However, fluorescence measurements, presented in Figure 6, showed also for this type of guest no change in optical properties upon complexation, making also this guest unsuitable for self-diagnostic systems.

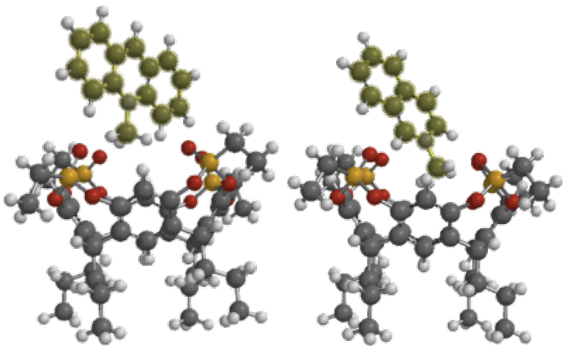

Figure 7: Tiiii[C_3H_7,H,C_2H_5] with *N*-methylacridinium (left) and *N*-methylisoquinolinium (right) as guest at STO-3G level of theory.

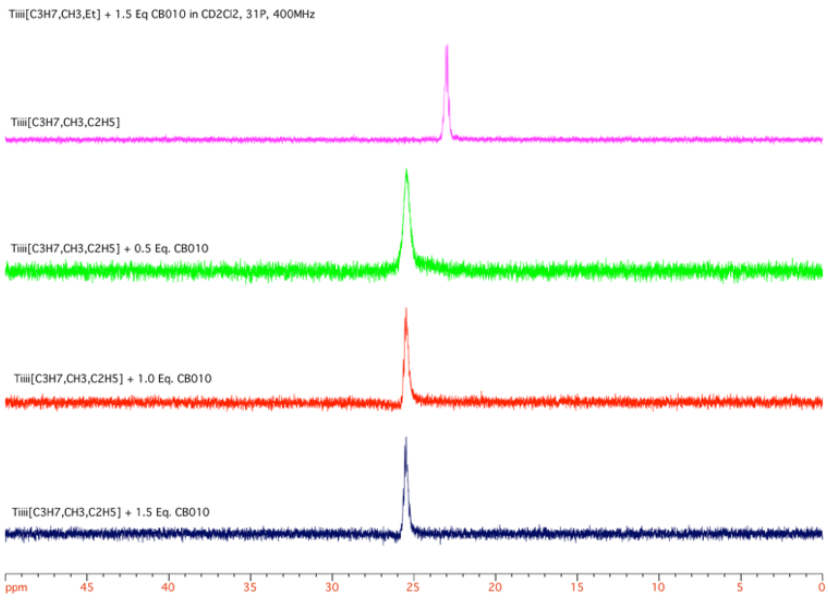

Figure 8: ^{31}P NMR titration of Tiiii[C_3H_7,H,C_2H_5] with *N*-Methyl-5-(oct-1-yn-1-yl)isoquinolin-2-ium iodide (shown in Figure 6) as guest.

3.3 *N*-methylated pyridinium salts for epoxy thermosets

A paper by Koh *et al.* [76] demonstrated to use of the complex formed by (*E*)-1-methyl-4-(2-(pyren-1-yl)vinyl)pyridin-1-ium (PyPyr) as a guest and calix[6]-arene-p-sulfonates as host as fluorescence based detection system for acetylcholine. In this complex, the fluorescence of the PyPyr guest, which is highly fluorescent when not complexed and in solution, is quenched.

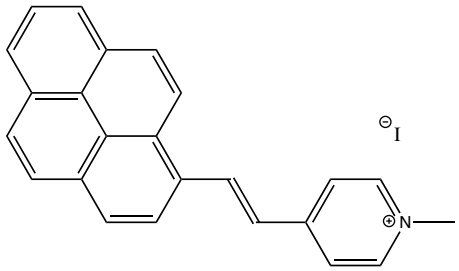

Figure 9: Structure of PyPyr.

To test the suitability of a PyPyr based system, PyPyr was prepared according to literature procedures[76] and titrations with Tiiii[C_3H_7,CH_3,C_2H_5] as host where performed in DCM. The absorption spectrum, present in Appendix G, showed several absorption maxima. Fluorescence titrations, performed at all maxima, as shown in Figure 10, showed a clear change in emission upon complexation at all wavelengths.

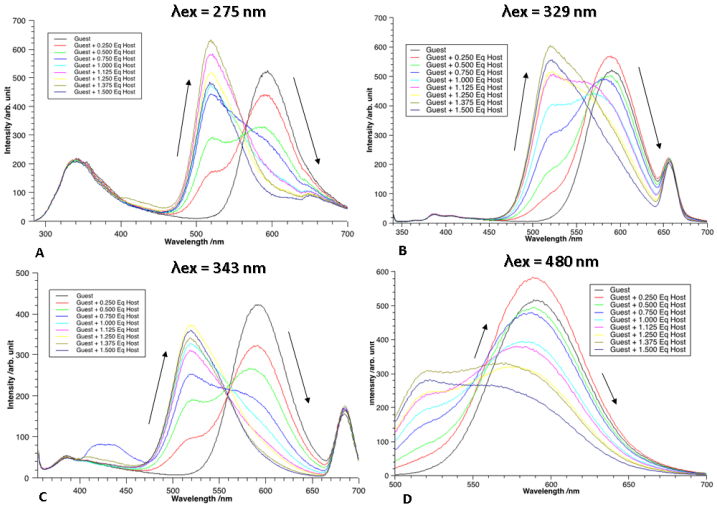

Figure 10: Fluorescence emission of PyPyr upon complexation with Tiiii[C_3H_7, CH_3,C_2H_5] in DCM ($c(PyPyr) = 5 \times 10^{-6}\,\mathrm{mol\,dm^{-3}}$, c(Tiiii[C_3H_7,CH_3,C_2H_5]) $= 0\,\mathrm{mol\,dm^{-3}}$ to $7.5 \times 10^{-6}\,\mathrm{mol\,dm^{-3}}$).

EC141NF and W241, provided by Elantas Europe s.r.l., were chosen as epoxy resin and curing agent (see Appendix D for data sheet). This combination was chosen for its optical transparency and low curing temperature. After incorporation of the of the system in the epoxy system EC141NF/W241, as described in section 3.7.2, however, no change in fluorescence was observed upon complexation, as visible in Figure 11.

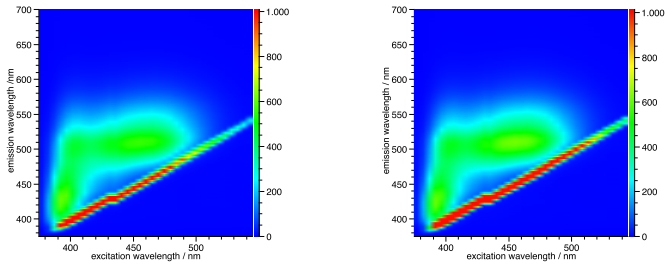

Figure 11: Fluorescence emission of PyPyr ($c(PyPyr) = 1 \times 10^{-5}\,\mathrm{mol\,kg^{-1}}$ in EC141NF/W241) in the absence (left) and presence (right) of Tiiii[$C_7H_{14}C_2H_3O$,H,Ph] (c(Tiiii[$C_7H_{14}C_2H_3O$,H,Ph]) $= 2 \times 10^{-5}\,\mathrm{mol\,kg^{-1}}$).

Literature studies revealed that pyridinium salts, such as the used PyPyr, when functionalised with a suitable leaving group, react in the so called Zincke reaction[77–79] with primary amines. Furthermore, reactions between 3-cyano-*N*-methylpyridinium iodides and amines have been demonstrated in literature. [80] Based on this knowledge, a hypothetical mechanism for the distruction of the fluorophore, shown in Scheme 1, was formulated analogous to the Zincke reaction. Being the curing agent W241 composed by primary amines, it is reasonable to assume that the guest is not compatible with the curing agent.

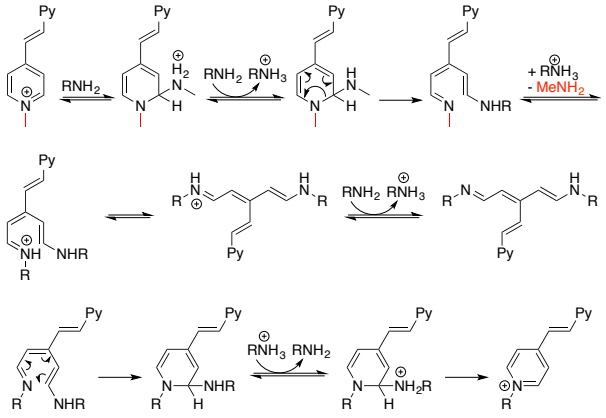

Scheme 1: Proposed mechanism for the destruction of PyPyr by exchange of the methyl group in the presence of primary amines.

In order to validate the hypothetical mechanism, PyPyr was treated over night with *N*-butylamine. After removal of the amine, the fluorescence in DCM solution in the presence and absence of phosphonate cavitand was compared to the fluorescence of untreated PyPyr. The measurements, shown in Figure 12, revealed a completely different fluorescence emission after the treatment, indicating that the decomposition of PyPyr is taking place in the presence of primary amines.

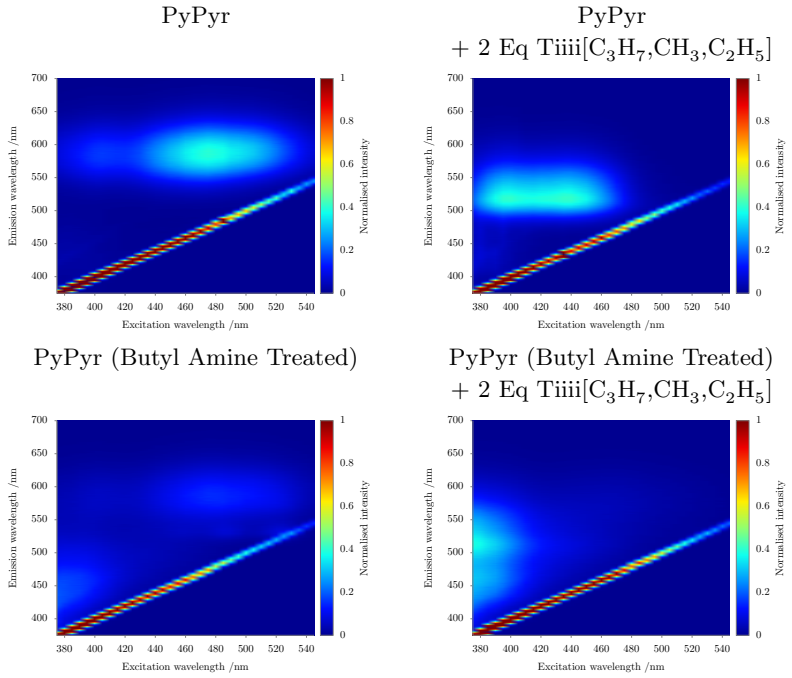

Figure 12: Fluorescence emission of PyPyr ($c(PyPyr) = 1 \times 10^{-6}\,\mathrm{mol\,dm^{-3}}$ in DCM) in the presence and absence of Tiiii[C_3H_7,CH_3,C_2H_5], before and after treatment with butyl amine.

3.4 Testing of catalytically cured epoxy thermosets

In order to test the suitability of catalytically curing agents for the use in self-diagnostic polymers, three non-primary amine based curing agents and one non-aromatic resin were obtained from Elantas s.r.l. and cured, also with the previously used, bisphenol A (BPA)-based EF141NF, according to the conditions given by Elantas. Characterisation of the optical window and fluorescence were performed for all samples. All samples showed thereby a strong fluorescence in the region of emission of the probe, making them unsuitable as matrix for this self-diagnostic system.

3.5 Alternative Fluorophores

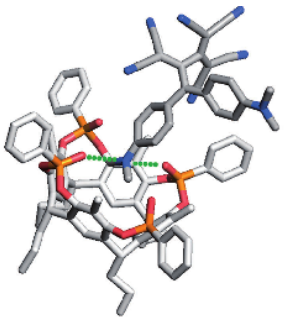

Figure 13: Crystal structure showing the dipole-cation interactions between a phosphonate cavitand and an imminium-type nitrogen. Taken from Reference [81].

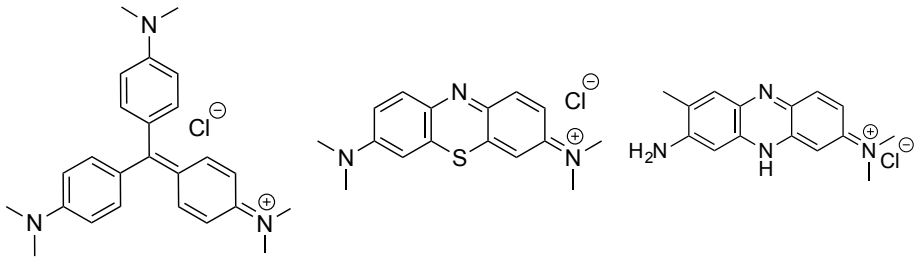

Figure 14: Structures of crystal violet (left), methylene blue (centre) and neutral red (right).

Pervious work in the group [81] showed that phosphonate cavitands are good hosts for *N,N*-dimethyliminium salts (see crystal structure in Figure 13). The three dyes shown in Figure 14 have this functional group and were therfore selected for further investigations. In a first step, ^{1}H and ^{31}P NMR titrations were performed to make sure complexation is taking place. As visible in Appendix B, in all cases, a clear shift in both spectra indicates that the complexation in fact is taking place. Fluorescence measurements however, as shown in Appendix C, showed no or only minor changes upon complexation, making all three guests unsuitable as probes for self-diagnostic polymers. This means, that in these cases, the complexation is not accompanied by fluorescence changes.

3.6 Conclusions

As shown in this section, while a wide variety of suitable guests for phosphonate cavitands exist, only very few display a significant change in their optical properties upon complexation. For suitable guests, such as PyPyr, another major

challenge is the reactivity of the epoxy resin components. Tests performed in this section show that the use of PyPyr as probe for self-diagnostic polymers is in principal possible, but a suitable matrix could not be identified. Such a matrix must possess a transparency window at least ranging from 400 nm to 550 nm, being non-fluorescent in that range and must be cured by other means than a primary amine. However, also the tested catalytic curing agents are not suitable. As alternative, different types of host-guest complexes were investigated, as shown in Sections 6 and 7.

3.7 Experimental

3.7.1 Synthesis

(*E*)-1-methyl-4-(2-(pyren-1-yl)vinyl)pyridin-1-ium (PyPyr)
PyPyr was prepared according to literature procedures[76].

3.7.2 General Procedure for the Transfer of Cavitand Complexes into Epoxy Systems

DCM solutions of the components with a concentration of $5 \times 10^{-4}\,\mathrm{mol\,dm^{-3}}$ for PyPyr and the relative phosphonate cavitand were prepared. Suitable amounts of those solutions where mixed together, then thoroughly mixed with a suitable amount of one of the epoxy components, usually the curing agent. The amount of the epoxy component was calculated in order to obtain the desired concentration in the final, cured thermoset, usually $5 \times 10^{-6}\,\mathrm{mol\,kg^{-1}}$. The obtained solution was placed in the oven at 60 °C and homogenised frequently during the evaporation process. Once the solvent was completely evaporated, the sample was removed from the oven and cooled to room temperature. The component containing the complex was subsequently used as directed by the manufacturer.

4 Strain field self-diagnostic PDMS elastomers

4.1 Introduction

The working mechanism of the proposed stress self-diagnostic polymeric system is sketched in Figure 15.

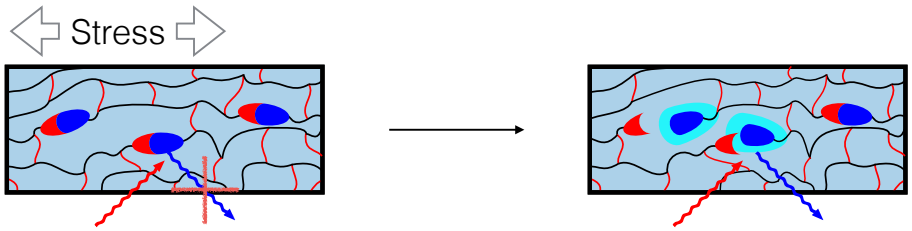

Figure 15: Schematic representation of the self-diagnostic polymer working system.

Its operation is based on the introduction of a tiny amount of fluorescence silent host-guest complexes in the polymer matrix as supramolecular crosslinks, which break apart upon mechanical stress in the strained zone, leading to localised fluorescence emission. Since host-guest interactions are considerably weaker than covalent bonds, the disconnection of the supramolecular crosslinks takes place well before the covalent bonds are broken, providing an early signal prior the mechanical integrity of the polymer is compromised. Very small quantities of the reporting system are needed, therefore physical and mechanical properties of the resulting self-diagnostic polymer are not altered.

4.2 Design and synthesis of the host-guest reporting probe

The chosen host-guest complex, shown in Figure 16, consists of a tetraphosphonate cavitand as host and a *N*-methylated pyridinium salt as guest. Both the guest and the host are functionalised with terminal double bonds (one in case of the guest, four in case of the host), over which the complex is randomly incorporated into polydimethylsiloxane (PDMS) chains, thereby adding supramolecular crosslinks to the system. Tetraphosphonate cavitands are, as explained in Section 3.1, versatile molecular receptors capable of binding *N*-methyl pyridinium[82] and *N*-methyl ammonium salts[83] with remarkable selectivity. Tetraphosphonate cavitands form highly stable complexes with *N*-methylpyridinium salts in apolar environments ($K_a = 5.8 \times 10^6\,\mathrm{mol}^{-1}\,\mathrm{dm}^{-3}$ in 1,2-dichloroethane)[69] via synergistic cation-dipole interactions between the charged nitrogen and the P=O groups and cation-π interactions between the same nitrogen and the π-basic cavity.[84] The guest design is inspired by another

Parts of this chapter are in preparation for publication: Andreas E. Früh, Federico Artoni, Roberto Brighenti, and Enrico Dalcanale. Strain field self-diagnostic PDMS elastomers. *Advanced Functional Materials*, in preparation.

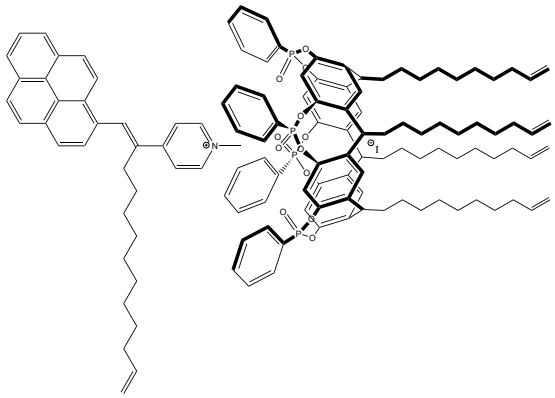

Figure 16: Reporting system, consisting of an N-methylated pyridinium salt (guest, left), and a tetraphosphonate cavitand (host, right), held together by specific host-guest interactions.

system reported in literature by Koh *et al.* [76]. They reported the quenching of a similar guest consisting of a N-methylated pyridinium without lateral chain conjugated to a pyrene in combination with calix[n]arene-p-sulfonates as artificial acetylcholine detection system.

The incorporation strategy requires the insertion of the reporting system as preformed complex in the polymer precursors before polymerisation, in order to have complete fluorescence quenching of all guests before mechanical tests. Moreover, the complex must be indefinitely stable in the unstressed polymer. The polymeric matrix compatible with the host-guest complex is a commercial RTV silicone rubber (PDMS), obtained by the platinum catalysed reaction of a vinyl PDMS pre-polymer with a silicon hydride component (H-PDMS, Figure 17), via formation of ethyl crosslinking bridges between the two.[85]

In order to incorporate the host-guest complex into the polymer system, both the host and the guest are functionalised with terminal alkenyl chains. The terminal double bonds are able to react during the curing of the used PDMS system, inserting the reporting complex randomly into the PDMS matrix. The alkenyl chain are long enough to permit sufficient conformational flexibility to the complex to avoid its mechanical dissociation during the curing of the matrix. The preformed complex is soluble and stable into the PDMS matrix.

The synthesis of the tetraphosphonate cavitand bearing four ω-undecenyl chains is described in the literature.[86, 87] Preparation of the guest was performed starting from 4-picoline, which was first alkylated with the double bond terminated linker chain in the benzylic position using N-butyllithium. The obtained pyridine was subsequently methylated using iodomethane and the obtained pyridinium salt condensed with 1-pyrenecarboxaldehyde in a Knoevenagel condensation, yielding the desired guest molecule. The host and the guest are then mixed together in DCM solution in a 2:1 ratio to form the desired complex. This solution is added to the vinyl-PDMS component and the resid-

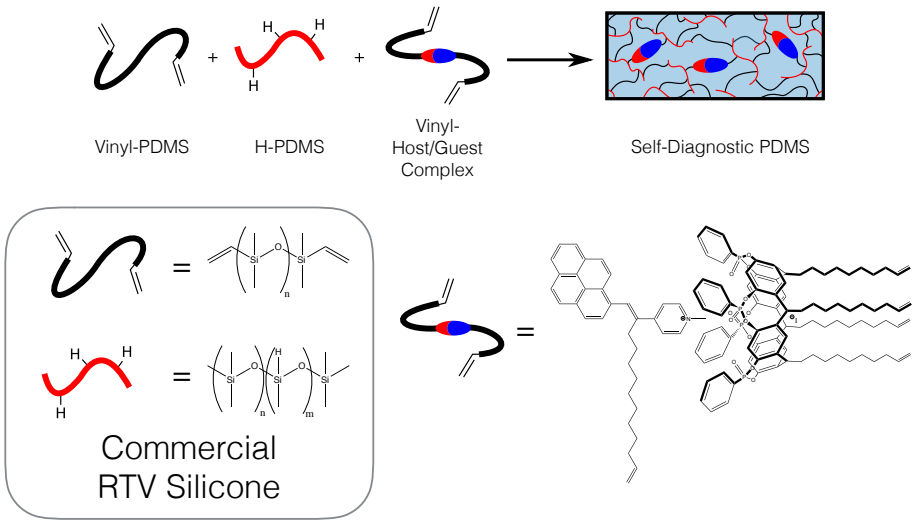

Figure 17: Schematic sketch of the self-diagnostic polymer system (top) and the respective chemical structures of the components (bottom).

ual DCM is removed by heating, giving an homogeneous mixture. Then the H-PDMS and the catalyst are added to the mixture, homogenised and poured into cuvettes for fluorescent measurements, or in molds for mechanical tests. The curing is performed directly in the cuvettes and molds by heating them in the oven to 40 °C overnight.

4.3 Fluorescence characterisation

The reporting complex is designed in a way that its dissociation leads to fluorescence emission. The *N*-methylated pyridinium salt alone, consisting of a pyrene conjugated with the pyridinium system, is highly fluorescent in solution as well as in the PDMS polymer matrix. Upon complexation, this fluorescence is quenched. This provides an easy and very sensitive way of detection for the dissociation of the complex. In solution, complete complexation of the fluorescent guest is ensured using a two-fold excess of the host.

The fluorescence of the guest was measured in DCM solution with a concentration of $c = 10^{-6}\,\mathrm{mol\,dm^{-3}}$ as well as in PDMS matrix with a concentration $b = 10^{-6}\,\mathrm{mol\,kg^{-1}}$, both in the presence and absence of the cavitand host (see Section 4.7.3). As clearly visible in Figure 18, the guest alone shows an intense fluorescence in the PDMS matrix when excited with ultraviolet light of about $\lambda = 345\,\mathrm{nm}$ with emission maximas at $\lambda = 380\,\mathrm{nm}$ and $\lambda = 400\,\mathrm{nm}$. In the complexed state, this is almost completely quenched. Unfunctionalised PDMS, as well as PDMS containing only the host, show no fluorescence emission in the measured range.

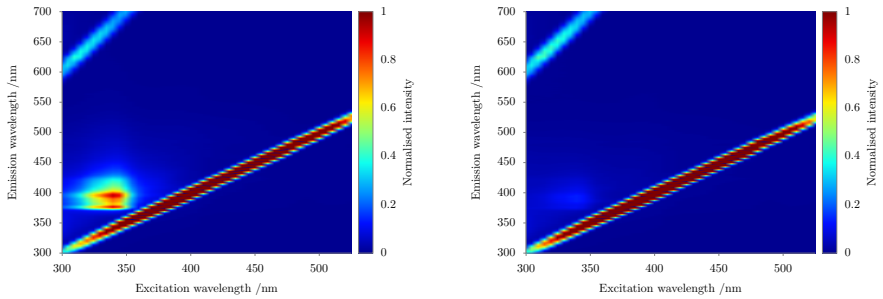

Figure 18: Steady-state fluorescence spectra of free guest (left) and the complex in PDMS (right). Both samples contain the guest in a concentration of $b = 10^{-6}\,\mathrm{mol\,kg^{-1}}$. The two lines are caused by first and second order Rayleigh scattering.

4.4 Mechanical testing and theoretical analysis

The proposed complex, being joined to the polymeric chains uniformly and isotropically, can upon detachmentupon detachment provide information related to the volumetric strain state in the material, *i.e.*, to its average volume stretch. Thus, when mechanical stress is applied to the system, it is expected that the complex will be separated before any damage is done to the material.

4.4.1 Preliminary tests

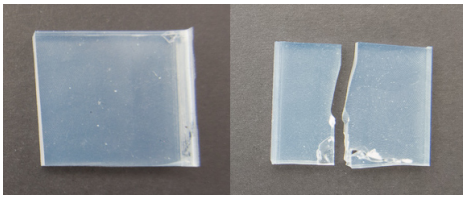

Figure 19: PDMS samples before and after breaking.

In order to test the suitability of the separation of the complex in the PDMS matrix by strain, specimens containing $10^{-6}\,\mathrm{mol\,kg^{-1}}$ of the reporting system were prepared (Figure 19). The tiny amount of reporting complex added does not alter the colour or transparency of the samples. These specimens were investigated under the fluorescence microscope, and subsequently first stretched and then broken. After every step, the fluorescence of each sample was reassessed. As shown in Figure 20, the samples shows no fluorescence in the pristine state. However, after stretching, clearly detectable fluorescence features appear, which were even more prominent after breaking the sample, and the most intense along the breaking edge.

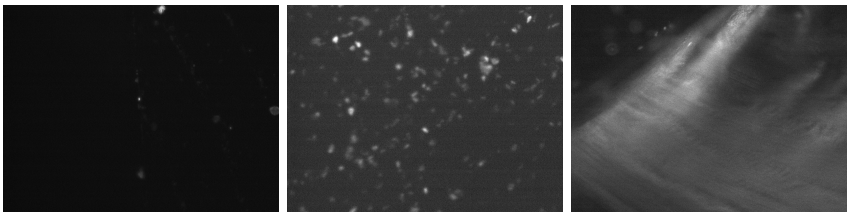

Figure 20: Fluorescence images of the sample before treatmen (left), after stretching (middle) and after breaking (right).

Interestingly, most of the fluorescence is not observed at the fracture edge, but in the nearby stressed region. Based on those findings, it was decided to investigate the fluorescence emission as function of strain induction both theoretically and experimentally. An additional picture can be found in Appendix E.

4.4.2 Mechanical characterisation

PDMS specimens, with and without self-diagnostic complexes, have been characterised (Table 1). Because of the chosen geometry of the specimen and the test procedure, the crack grows in a stable fashion along the middle cross-section of the precracked beam. As can be observed, the geometrical and the mechanical parameters of the various specimens are almost identical; this confirms that the addition of the host-guest complex to the matrix does not alter the micromechanical structure of the material. In Table 1 the geometrical and mechanical characteristics of the tested specimens (see Figure 21) are reported; it can be easily noticed that the addition of the host-guest complex to the matrix does not modify the elastic modulus and the Poissons ratio of the polymer, the two main mechanical characteristics of materials. Their values, together with the materials strength, must fulfil the design requirements in real applications in order to guarantee the desired mechanical response to external actions.

Table 1: Geometrical and mechanical characteristics of the tested specimens. (E = elastic modulus; ν = Poissons ratio; G_c = fracture energy; K_c = fracture toughness.

Sample	L	W	a_0	t	ρ	Self-diagnostic	E	ν	G_c	K_c
	mm^{-1}	mm^{-1}	mm^{-1}	mm^{-1}	μm^{-1}		MPa^{-1}		$m\,N^{-1}$	$/MPa\sqrt{m}$
1a	102	25	5	6	150	NO	0.99	0.43	110	16.2
1b	102	25	5	6	150	YES	0.98	0.43	110	16.2
1c	102	25	5	6	150	YES	1.01	0.43	110	16.2

For sake of completeness, in Table 1 the geometrical parameters (length L, width W, initial crack depth a_0, thickness t and curvature radius ρ at the notch tip) characterising the pre-cracked beam specimen are reported (Figure 21); moreover, the energy G_c necessary for the formation of the unit area of fracture

and the fracture toughness related parameter, K_c, are also given for the tested materials.

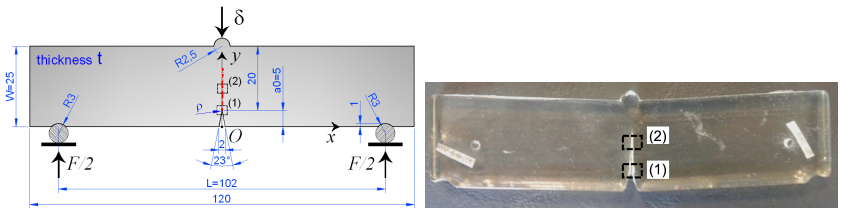

Figure 21: Dimensions of the samples used for three-point bending mechanical stress tests (all lengths are given in millimeters, left). Side view of the specimen after the propagation of the initial crack (after finishing the test). Locations (1) and (2) where the fluorescence picture have been taken are shown (right).

4.4.3 Experimental mechanical tests and finite element analysis

Besides the experimental tests, an accurate material linear elastic and geometrically nonlinear finite element (FE) analysis of the specimen has been performed in order to get the stress and strain field around the crack tip before the crack growth; being the material behaviour roughly elastic up to the first crack growth, a mechanically linear elastic analysis can be considered to be reasonable to provide the stress and strain values close to the crack tip.

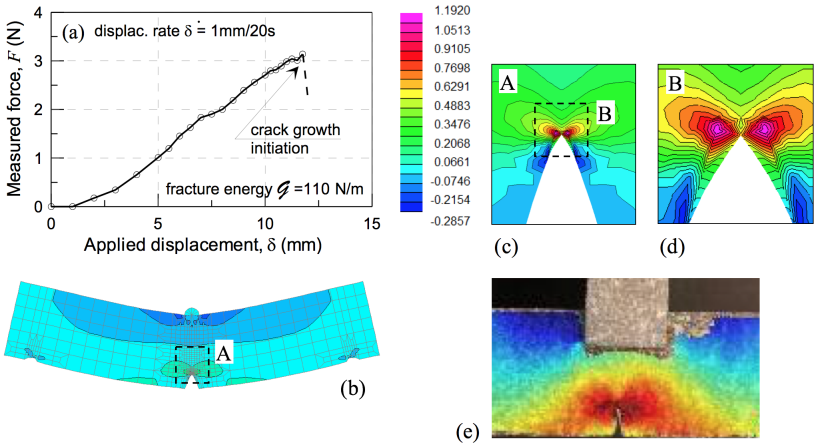

Figure 22: Load-displacement curve for the specimen 1b (a). Map of the strain ϵ_{xx} in the deformed beam obtained through the linear elastic FE analysis (b), related details (c, d) and digital image correlation (DIC) analysis results (e) of the crack tip region for an applied downward displacement $\delta = 12\,\text{mm}$.

In Figure 22a the experimental load versus displacement curve is illustrated, while in Figure 22b-d the evolution of the strained zone extension ahead of the

crack tip during the loading process is shown as obtained from the FE analysis while in Figure 22e the corresponding strain obtained through the DIC analysis is shown. In Figure 22b-d the numerically obtained ϵ_{xx} strain field map is shown at the instant just before the crack growth. Figure 22b shows the whole beam, while Figure 22c and 22d show some details taken around the crack tip by increasing the magnification. In Figure 23 the fluorescence measurement and the relative colour map are shown for the blank specimen 1a (see Table 1) in the area around the initial crack tip after the crack started to grow, while in Figure 24 the fluorescence pictures and their colour maps are shown for the specimen 1b (the self-diagnostic specimen 1c showed similar results).

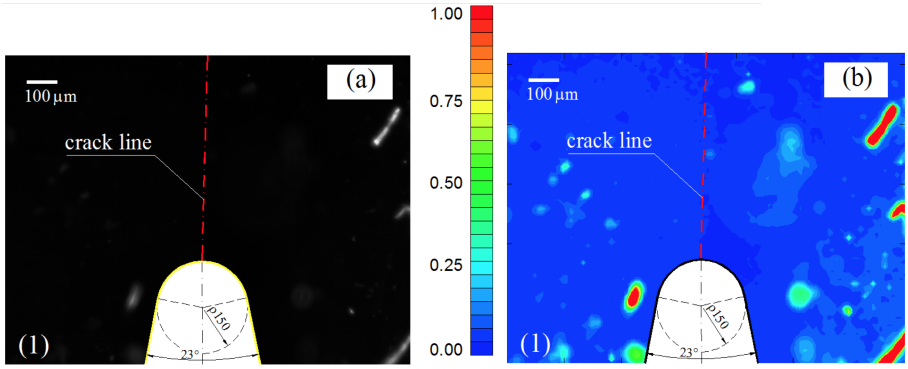

Figure 23: (a) Fluorescence image of the crack tip region (1) for the blank specimen 1a. Colour map of the measured fluorescence in the same region (b).

Both the initial crack tip region (1) (Figure 24c and 24d) and the area along the crack path (2) (Figures 24a and 24b) have been considered; it can be clearly noted that the fluorescence appears in highly stretched regions. In particular the stretched area around the initial crack tip shows the highest fluorescence evidence, since the localised strain arising before the crack growth is related to an initial blunted crack rather than to a perfectly sharp crack.

In fact, due to geometrical limitations in sample preparation (the initial fluid material is poured in a mold and then cured as explained in the experimental section), the initial crack has a finite curvature radius ρ at its tip (which has been measured to be equal to about 150 µm), so the initial geometry of the defect is that of a notch rather that of a crack; after initiation of the crack growth, the defects propagates with a perfectly sharp tip and so the stress and strain field is different to that of the initial notch.

In other words, the highest strain values are much more concentrated in a narrow region in the case of a perfect sharp crack than in the case of a notch and so the propagation needs a highest strain level to reach the crack growth condition.

After the crack started to growth, the highest strained region has a small size compared to the crack, and a tiny narrow trace of the propagating straight defect can only be appreciated in Figure 24a,b. Some small spot-like fluorescent

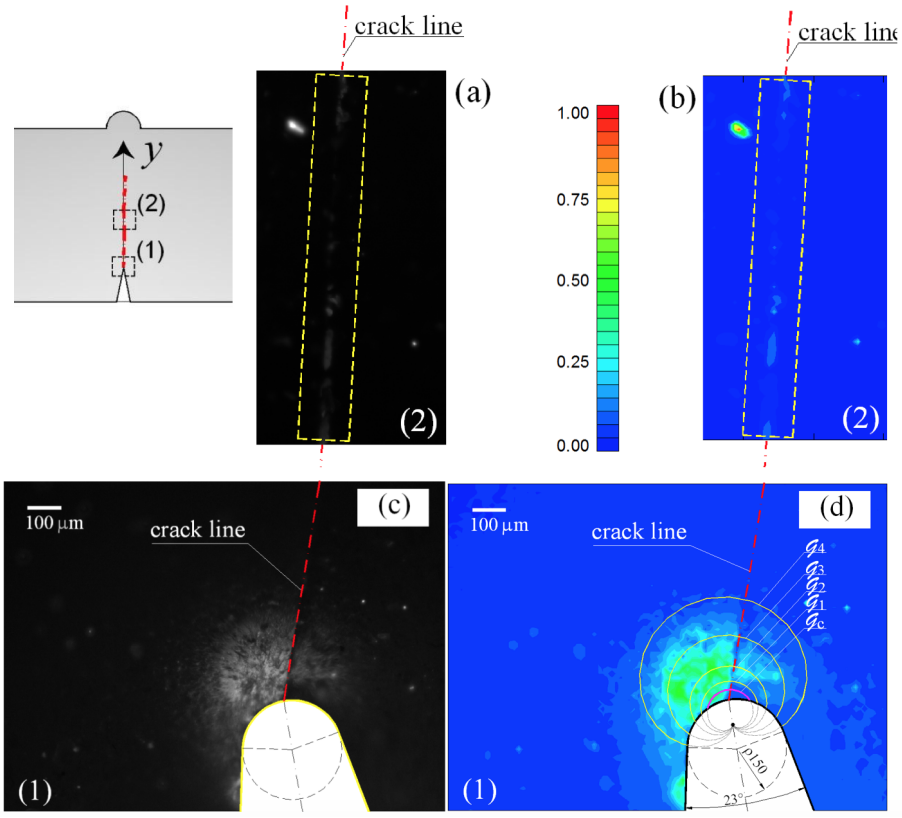

Figure 24: (a) Fluorescence images (a, c) and corresponding fluorescence colour maps (b, d) of the crack tip region (1) and along the crack growth path (2). In Figure (d) the tensile iso-hydrostatic stress curves are plotted and correspond to the energy values $G_c = 110\,\mathrm{N\,m^{-1}}$ (critical energy corresponding to material damage), and $G_1 = 85\,\mathrm{N\,m^{-1}}$, $G_2 = 55\,\mathrm{N\,m^{-1}}$, $G_3 = 27\,\mathrm{N\,m^{-1}}$, $G_4 = 11\,\mathrm{N\,m^{-1}}$.

regions can be also appreciated in Figure 23 and 24; they are not strain-related fluorescence since such high values are due to dust or small inclusions embedded in the material that provide a false brightness in the pictures taken under UV light.

In Figures 23 and 24 the colour scale indicates the fluorescence intensity in order to quantify the fluorescent response and relate it to the strain level experienced by the material; the scale has been made to vary between 0 and 1, where the 0 level indicates no fluorescence, while the intensity level 1 indicates the maximum fluorescence intensity provided by the measurements.

In order to correlate the fluorescence regions of the stretched specimen to the mechanical tension or deformation, some strain or stress-related quantity needs to be properly defined. As explained in the Section 4.5, a damage-related

parameter can be defined according to the so-called cavitation criterion [67, 88] which assumes as the primary cause of damage the tensile hydrostatic stress beyond a certain critical value. The hydrostatic stress (or equivalently strain) represents the volume average value of the stress acting in all directions of the 3D space in a given point of the material; since the host-guest molecular system (see Figure 15) is isotropically oriented inside the polymeric matrix, such a volumetric strain well represents the average deformation occurring in the cavitand-based complex and so it is reasonable to assume that the observed fluorescence level provides a measure of the density of the broken supramolecular system inside the polymer.

In Figure 24d the iso-hydrostatic stress curves are displayed (see yellow lines) for different values of the energy ($G_c > G_1 > G_2 > G_3 > G_4$, see Section 4.5); in particular the smallest region identified by the pink curve corresponds to the critical energy G_c (see Table 1) that identifies the damaged region of the material produced by the previously applied mechanical stress. Outside the curve corresponding to the critical energy G_c the material is still elastic and recover completely its initial free-strain state after unloading; however the cavitand-based sensing system provides a clear trace of the strains previously occurred in the material during the applied loading. It's worth noting that the fluorescence picture and the corresponding map show a certain asymmetry with respect to the crack axis; this can be explained by the very small amount of the cavitand-based sensing complexes embedded in the polymer (less than 0.0036 % w/w), besides also experimental uncertainties, that does not provide an homogeneously brightness in the strained area. Despite such a not perfectly shaped bright region, the developed supramolecular system provides precious information about the strains experienced by the material and has shown to be a promising and innovative tool for mechanical self-sensing in materials where strain values are needed without complex testing equipment.

4.5 Quantitative modelling of the damage-related fluorescence

The aim of this section is to provide a quantitative basis of the fluorescence measurements and to relate them to some deformation parameter of the material.

On the basis of experimental observation, the failure of elastomeric materials, such as the PDMS one, has been explained to be driven by the expansion and growth of spherical-like cavities initially present in the bulk of the material at the mesoscale level; because of their very low elastic modulus value with respect to the cohesive strength, a noticeable pressure sensitivity, in presence of voids or initial embedded defects, arises for this class of materials.[67, 88]

The damage development in elastomers typically corresponds to the coalescence and growth of microscopic voids into macroscopic ones preferentially triggered by tensile hydrostatic stress states leading to a failure mechanism also known as cavitation.[89]

Thanks to the capability of elastomers to withstand very high deformation value, allowing to smooth out the most severe peak stress, it can be assumed that the tensile hydrostatic pressure represent the most sensible stress state for the material.

Since the damaged material is very localised in a narrow region close to the crack tip, outside which the material behaves practically in an elastic fashion, the energy balance written according to the Griffiths approach for a penny shaped circular crack with radius ρ can be stated as:

$$\partial(W + \Psi + G)/\partial\rho < 0 \tag{1}$$

where $W, \Psi, G = 4\pi\rho^2\gamma$ are the potential energy of the applied forces, the deformation energy stored in the material and the fracture energy, respectively, while γ represents the fracture energy per unit surface. By assuming that the external forces are statically applied, no others dissipation effects exist and that the failure cavitation takes place instantaneously when the critical condition is fulfilled, the energy of the external load is zero, $W = 0$ and the energy balance leads to the classical fracture criterion

$$\partial\Psi/\partial\rho > 4\pi\rho^2\gamma \tag{2}$$

By using the above inequality, the relationship between the materials fracture energy and the critical tensile pressure leading to the unstable expansion of a spherical cavity, embedded in an infinite elastic neo-Hookean medium, with radius ρ can be expressed by considering the energy G released when an initial crack with radius ρ growths to a bigger one with radius[90]:

$$G = \lim_{d\rho\to 0}[(\Psi(\rho) - \Psi(\rho + d\rho))/(2\pi\rho d\rho)] \tag{3}$$

By assuming that the initial penny-shaped crack expands in a spherical cavity having the same radius without any further energy, the term $\Psi(\rho)$ can be evaluated by solving the elastic problem of an infinite elastic medium containing a spherical void inflated by a pressure p.[90] This leads to:

$$G = 2E\rho\frac{1 + \lambda_S^2 - 2\lambda_S^{-1}}{3} \tag{4}$$

where λ_S is the surface stretch and E the Young modulus of the material. Finally, by relating the surface stretch λ_S to the applied pressure p as $p(\lambda_S) = E \times (5 - 4\lambda_S^{-1} - \lambda_S^{-4})/6$, with $\lambda_S = S'/S = 1 + 2d\eta \times \eta^{-1}$ (with S, S' the external surfaces of the initial and final spherical void, respectively), the previous equation can be explicitly rewritten as a function of the pressure p; in cases of sufficiently high pressure, namely $p > 11E/18$ [88], we have:

$$G \cong \frac{2E\rho}{3}[\frac{16/25}{[1 - (6p/5E)]^2} - \frac{3}{2} + \frac{3p}{E}] \tag{5}$$

and by taking the fracture energy G equal to the materials fracture energy, $G_c = \gamma$, the critical pressure p_c responsible for the cavitation rupture can be

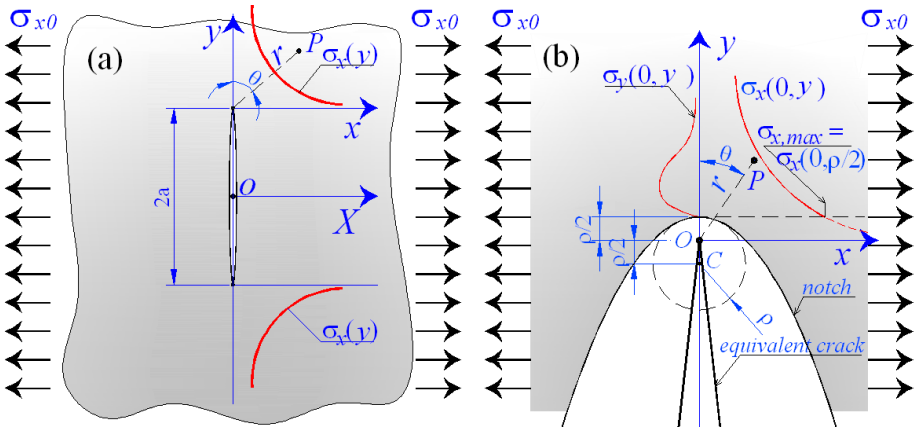

Figure 25: Scheme of the standard cracked infinite plane with a crack with length 2a (a) and that of a rounded crack tip (notch) (b).

determined as that fulfilling the inequality:

$$[\frac{16/25}{[1-(6p_c/5E)]^2} - \frac{3}{2} + \frac{3p}{E}] \geq \frac{3G_c}{2E\rho}, p \neq 5E/6 \tag{6}$$

The previous relation allows to determine the critical pressure value p_c once the radius of the initial intrinsic defect, the elastic modulus and the materials fracture energy are known.

Equation 6 can be easily employed to relate the hydrostatic pressure to the stress field arising close to the crack tip.

By considering only the Mode I of fracture in a purely linear elastic cracked 2D infinite plate, the stress field arising close to the crack tip is characterised by the following expressions of its components [91]:

$$\sigma_{ij} = \begin{Bmatrix} \sigma_{11} \\ \sigma_{22} \\ \sigma_{12} \end{Bmatrix} = \begin{Bmatrix} \sigma_x \\ \sigma_y \\ \tau_{xy} \end{Bmatrix} = \frac{K_I}{\sqrt{2\pi r}} \begin{Bmatrix} \cos\varphi(1+\sin\phi\sin 3\phi) \\ \cos\varphi(1-\sin\phi\sin 3\phi) \\ \sin\varphi\cos\varphi\cos 3\varphi \end{Bmatrix}, \varphi = \frac{\theta}{2} \tag{7}$$

where the Mode I Stress-Intensity Factor K_I (SIF) has been introduced; in general it is written as $K_I = Y_I \times \sigma_{x0}\sqrt{\pi a}$, where Y_I is the so-called geometric correction factor (that depends on the geometry, loading and boundary conditions applied to the body), σ_{xO}, a are the remote applied stress and the crack size, respectively, while θ represent the angular coordinate as shown in Figure 25. The crack extension takes place as soon as the critical value of the SIF, K_c, is reached; such a value is also related to the fracture energy of the material through the relation: $G_c = K_c^2/E$.

The corresponding strain field obtainable by inverting the elastic stress-strain constitutive equations for an elastic isotropic material, $\sigma_{ij} = C_{ijhk}\epsilon_{hk}$ (being $C_{ijhk} = k\delta_{ij}\delta_{hk} + \mu(\delta_{ih}\delta_{jk} + \delta_{ik}\delta_{jh} - 2\delta_{ij}\delta_{hk}/3)$ the components of the

fourth-order elastic tensor of the material, being μ, $k = E/(3(1-2\nu))$, E, ν the shear, bulk, elastic modulus and Poissons ratio, respectively) is given by:

$$\begin{Bmatrix} \epsilon_{11} \\ \epsilon_{22} \\ 2\epsilon_{12} \end{Bmatrix} = \begin{Bmatrix} \epsilon_x \\ \epsilon_y \\ \gamma_{xy} \end{Bmatrix} = \frac{K_I}{\sqrt{2\pi r}} \begin{Bmatrix} \cos\varphi[(1-\nu)+(1+\nu)\sin\varphi\sin 3\varphi] \\ \cos\varphi[(1+\nu)(1+\sin\varphi\sin 3\varphi)] \\ 2(1+\nu)\sin\varphi\cos\varphi\sin 3\varphi] \end{Bmatrix} = \frac{K_I}{\sqrt{2\pi r}} \begin{Bmatrix} 1-\nu \\ 1+\nu \\ 0 \end{Bmatrix} \quad (8)$$

The above expressions have been written by considering the plane stress condition that effectively arises in the thin tested beam.

The above expressions of the stress and strain fields are valid only in a limited region around the crack tip; for this reason such a region is also termed to be SIF-dominated because everything (stress, strain, deformation energy, etc.) depends only on the K_I factor.

On the other hand, it has been recalled that the initial crack tip presents a finite curvature radius, namely ρ; in this case Creager and Paris [92] determined the stress field around the notch root by observing that it is well described by the singular stress field of a crack with the same notch centerline axis but properly shifted of an amount $\rho/2$.

In particular, for a notched structural component under a remote uniform stress acting parallel to the x-axis, $\sigma_{nom} = \sigma_{x0}$, the plane stress tensor components are given by the following expressions:

$$\begin{Bmatrix} \sigma_x \\ \sigma_y \\ \tau_{xy} \end{Bmatrix} = \begin{Bmatrix} \sigma_{x0} \\ 0 \\ 0 \end{Bmatrix} + \frac{K_I}{\sqrt{2\pi r}} \begin{Bmatrix} \cos\varphi(1+\sin\phi\sin 3\phi) + (\frac{\rho}{2r}\cos 3\varphi) \\ \cos\varphi(1-\sin\phi\sin 3\phi) - (\frac{\rho}{2r}\cos 3\varphi) \\ \sin\varphi\cos\varphi\cos 3\varphi - (\frac{\rho}{2r}\cos 3\varphi) \end{Bmatrix}, \varphi = \frac{\theta}{2} \quad (9)$$

where $K_1 = \sigma_{x0} Y \sqrt{\pi a}$ is the standard SIF of the equivalent crack having its tip placed at $\rho/2$ from the notch root. Along the y-axis (vertical line identified by $\theta = 0°$, Figure 25b having its origin O at the equivalent crack tip position, the stresses can be simply expressed as follows:

$$\sigma_x = \sigma_{x0} + \frac{K_I}{\sqrt{2\pi r}}(1 + \frac{\rho}{2r}, \sigma_y = \frac{K_I}{\sqrt{2\pi r}}(1 - \frac{\rho}{2r}, \tau_{x,y} = 0 \quad (10)$$

$$\sigma_z = 0(\text{plane stress}), \sigma_z = \nu(\sigma_{x'} + \sigma_y)(\text{plane stress})$$

Making use of the Equation 9, the hydrostatic pressure can be determined as $p = \sigma_{ii}/3$, and the critical condition for damage Equation 12 can be solved with respect to the distance r, *i.e.*, the region where the tensile hydrostatic stress is beyond the cavitation limit can be identified (see Figure 24).

In Figure 24, the curves of iso-tensile hydrostatic stress, corresponding to different energy values ($G_c > G_1 > G_2 > G_3 > G_4$), are shown around the crack tip; those regions can be compared to the fluorescence bright areas provided by the supramolecular system, in order to verify if the hydrostatic stress (or equivalently the hydrostatic strain, since they are proportional each other in an isotropic material) corresponds to the observed fluorescence brightness values.

The comparisons made confirm quite well that the chemical cavitand-based sensing system provides the hydrostatic strain field occurred in the material, even after the materials recovers its initial free-strain (or equivalently free-stress state) after elastic unloading.

4.6 Conclusions and outlook

In conclusion, we prepared and characterised a self-diagnostic PDMS polymer, exploiting the fluorescence properties of a pyrene conjugated *N*-methylpyridinium salt guest in combination with a tetraphosphonate cavitand host. The polymer exhibits no fluorescence when the intact complex is present, but a clear fluorescence emission of the guest when dissociated from the host. In this way, it is possible to detect regions of increased volumetric strain during the controlled cracking under a three-point bending system of bar shaped PDMS samples. Comparison of the so obtained fluorescence maps of the crack tip region with numerical models of the volumetric strain showed good alignment between the measured fluorescence and the numerical model. It is therefore reasonale to believe that the presented system is suitable for the detection of regions of high volumetric strain in soft polymeric matrices and thus can be used predict the failure of such materials, increasing their applicability.

Further it can be relevant to observe that such a self-sensing strain system can be easily applicable to any structural element by simply coating it with a thin film of the polymer charged with the host-guest cavitand system. If the base material and the coating adhere perfectly under the application of the the mechanical loading, the strain values experienced by the structural material will be nearly the same occurred in the self-sensing coating layer and so the self-diagnoistic layer provides a driect and simple way of quantitatively detect the strain values.

4.7 Experimental section

4.7.1 Synthesis

4-(Dodec-11-en-1-yl)pyridine

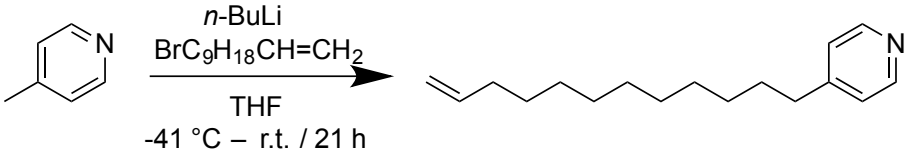

4-Picoline (2.6 mℓ, 29.17 mmol) was dissolved in dry THF (12 mℓ) and the solution was cooled to −41 °C with an acetonitrile-liquid nitrogen slush bath.[93] *N*-Butyllithium in hexanes (2.5 mol dm^{-3}, 13.5 mℓ, 33.75 mmol) was added over 30 min. The reaction was stirred for additional 5 min at −41 °C, then the bath was removed and the reaction allowed to warm up to room temperature. After 1 h, additional dry THF (12 mℓ) was added to dilute the 4-picolyllithium slurry and the obtained solution stirred for 1 h more. The solution was cooled with an ice bath to 0 °C and added over 30 min into a solution of 11-bromo-l-undecene (7.0 mℓ, 31.91 mmol) in THF (5 mℓ) at −41 °C. The reaction was allowed to warm up to room temperature and stirred for 1 h. Water (1.5 mℓ) was added,

the obtained mixture filtered over a silica pad and the pad washed with ethyl acetate (6× 30 mℓ). The organic phases were combined, the solvent removed and the residue was further purified by flash chromatography (Hex/EtOAc 1.5/1), yielding a yellow oil (4.15 g, 50 %). ^{1}H NMR (300 MHz, $CDCl_3$) δ: 8.42 (d, J = 6.0 Hz, 2H), 7.03 (d, J = 6.0 Hz, 2H), 5.75 (ddt, J = 17.0, 10.3, 6.7 Hz, 1H), 4.97-4.85 (m, 2H), 2.53 (t, J = 7.7 Hz, 2H), 1.98 (q, J = 7.0 Hz, 2H), 1.55 (q, J = 7.3 Hz, 2H), 1.34-1.22 (m, 15H); ^{13}C NMR (75 MHz, $CDCl_3$) δ: 151.5, 149.5, 139.0, 123.8, 114.1, 35.2, 33.7, 30.2, 29.50, 29.44, 29.42, 29.34, 29.12, 29.07, 28.87; MS (ESI) m/z: $[M + H]^+$ calcd for $C_{17}H_{28}N$, 246.22; found, 246.28.

_N_-methyl-4-(dodec-11-en-1-yl)pyridinium iodide

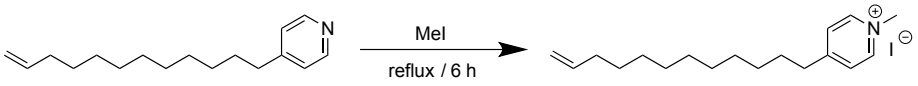

4-(Dodec-11-en-1-yl)pyridine (561 mg, 2.29 mmol) was dissolved in iodomethane (4.0 mℓ, 46.3 mmol) and refluxed under nitrogen for 6 h. The product was precipitated with diethyl ether, filtered off, washed with diethyl ether and dried *in vacuo*, yielding an off-white solid (884 mg, 100 %). ^{1}H (300 MHz, $CDCl_3$) δ: 9.24 (d, J = 6.6 Hz, 2H), 7.84-7.80 (m, 2H), 5.87-5.71 (m, 1H), 5.01-4.84 (m, 2H), 4.63 (s, 3H), 2.90-2.81 (m, 2H), 2.06-1.94 (m, 2H), 1.74-1.60 (m, 2H), 1.32-1.18 (m, 15H); MS (ESI) m/z: $[M - \text{Iodine}]^+$ calcd for $C_{18}H_{30}N$, 260.24; found, 260.27.

_N_-methyl-4-(1-(pyren-1-yl)trideca-1,12-dien-2-yl)pyridinium iodide

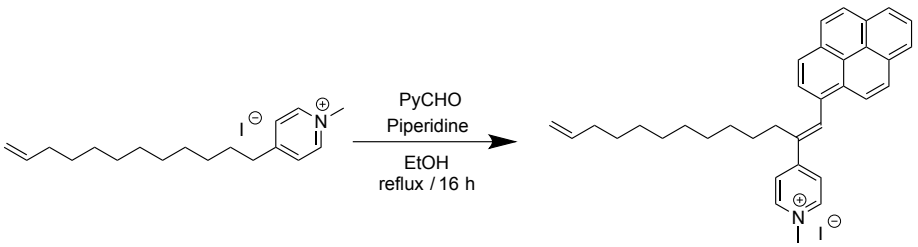

1-Pyrenecarboxaldehyde (400 mg, 1.74 mmol) dissolved in ethanol (3.0 mℓ) and *N*-methyl-4-(dodec-11-en-1-yl)pyridinium iodide (236 mg, 0.61 mmol) and piperidine (200 µℓ) were added. The reaction was stirred under reflux for 16 h, then the solvent removed and the obtained crude purified by flash chromatography (DCM/MeOH 95/5), yielding a orange solid (44 mg, 12 %). ^{1}H (300 MHz, $CDCl_3$) δ: 9.27 (d, J = 6.7 Hz, 2H), 8.82 (d, J = 6.7 Hz, 2H), 8.23-7.96 (m, 8H), 7.56 (d, J = 6.4, 2H), 5.83-7.72 (m, 1H), 5.05-4.90 (m, 2H), 4.70 (s, 3H), 2.89-2.2.71 (m, 2H), 2.09-1.91 (m, 2H), 1.64-1.60 (m, 2H), 1.44-1.04 (m, 15H); MS (ESI) m/z: $[M - \text{Iodine}]^+$ calcd for $C_{35}H_{38}N$, 472.30; found, 472.34.

Tetraphosphonate cavitand host
The phosphonate cavitand was prepared according to literature procedures[87].

4.7.2 PDMS preparation

A commercially available room temperature vulcanisation silicone kit, RTV 615 (Momentive Performance Materials Inc., Waterford, NY) was used to prepare the matrix. Dichloromethane solution of guest ($c = 1 \times 10^{-5}\,\mathrm{mol\,dm^{-3}}$) and host ($c = 2 \times 10^{-5}\,\mathrm{mol\,dm^{-3}}$) were prepared in order to preform the supramolecular complex and to easily measure the desired quantities. The required quantities of the solutions or a mixture thereof were added to component A of RTV 615 and the solvent subsequently removed by warming the component to 60 °C. Mixing of the preloaded component A with component B and subsequent curing at 40 °C overnight yielded the used polymer samples.

4.7.3 Fluorescence characterisation

Samples for fluorescence characterisation were prepared using the required amount of guest solution with or without an equivolumar amount host solution in order to obtain samples with a concentration of $b(guest) = 1 \times 10^{-6}\,\mathrm{mol\,dm^{-3}}$. Preparation was performed as described above and the obtained samples cured at 40 °C overnight directly in cuvettes (poly(methyl methacrylate), path length 10 mm, Sigma-Aldrich Z188018). Spectra were recorded on a PerkinElmer LS 55 Fluorescence spectrometer using FL WinLab.[94] Data was plotted using Gnuplot.[95]

4.7.4 Stress Test Samples

Samples for mechanical stress tests were prepared using the required amount of guest solution mixed with an equivolumar amount of host solution in order to obtain samples with a concentration of $b(guest) = 1 \times 10^{-6}\,\mathrm{mol\,dm^{-3}}$. Blank samples were prepared without any additions. Samples were cured in a custom made aluminum mold, yielding specimens with the dimensions shown in Figure 21.

The obtained pre-cracked samples were tested under a three-point bending system; a vertical controlled downward displacement δ were applied to the top central point of the beam at a rate equal to about $\delta = 5 \times 10^{-5}\,\mathrm{m\,s^{-1}}$; the corresponding restraint force F (see Figure 21) was measured during the test. The applied displacement δ was increased until the crack started growing upward (leading roughly to a crack along the middle cross-section of the beam specimen, see Figures 23, 24), and continuously increased until the crack reached a final length equal to about 3 times its initial size before the final failure. Beside mechanical and kinematic measurements, the specimen was also monitored through the Digital Image Correlation (DIC) technique in order to obtain quantitatively the displacement and the strain field of the side surface of the specimen.

High resolution pictures ware taken for some increments of the applied displacement at a step equal to and processed through the freely available DIC analyzer NCORR software.[96]

Following the mechanical treatment, the samples were examined using a Nikon XXX (Nikon Corp., Tokyo, Japan) equipped with an UV-1A ultraviolet excitation filter block (Nikon Corp., Tokyo, Japan; Excitation filter wavelengths: 360-370 nm (bandpass, 365 CWL); Dichromatic mirror cut-on wavelength: 380 nm (longpass, LP); Barrier filter wavelengths: 420 nm cut-on (longpass, LP)) and a XYZ camera (Nikon Corp., Tokyo, Japan). Pictures were taken and processed using ImageJ.[97]

5 Carbon fibre nanohybrids

5.1 Introduction

Polymer composites are, thanks to their mechanical properties, corrosion resistance, flexibility and ease of fabrication, an important class of engineering materials. As special class thereof are the so called fibre-reinforced polymers (FRP), consisting of a polymeric continuous-phase or matrix, reinforced with fibrous material such as glass-, carbon-, aramid- or asbestos-fibres.[98] Carbon fibre reinforced epoxy composites are widely used in the aeronautic sector, but more and more also in the automotive and and civil engineering industries. They allow, by comparable mechanical properties, a weight reduction of more than 20 % compared to aluminium and more than 50 % compared to steel, making them a very attractive material for high performance materials.[99] However, the integrity of the material is very important for such applications, as sudden failure could lead to disastrous consequences.

Despite the many applications, very little is published about carbon fibres (CF) and their application in carbon fibre reinforced composite (CFRC).

CFs are defined by the IUPAC as "fibres (filaments, tows, yarns, rovings) consisting of at least 92 % (mass fraction) carbon, usually in the non-graphitic state"[1], but little research has been published about the microstructure, which also depends on the raw material, process, treatment and many more factors. On of the most thorough investigations of CF-microstructure was published by Johnson [100], and a schematic representation of the microstructure of a poly(1-acrylonitrile) (PAN)-based CF taken thereof is shown in Figure 26.

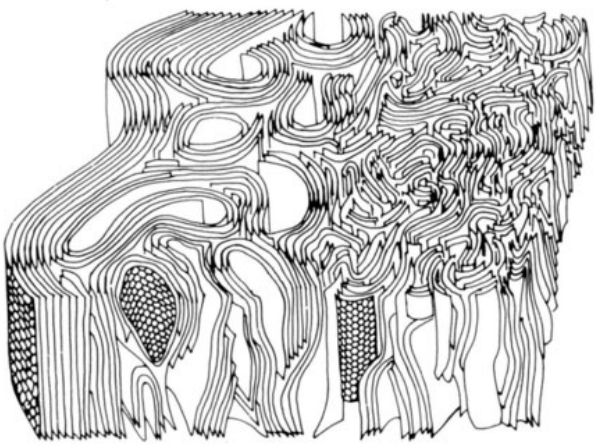

Figure 26: Schematic three-dimensional representation of structure in PAN-based CF. Taken from Reference [100].

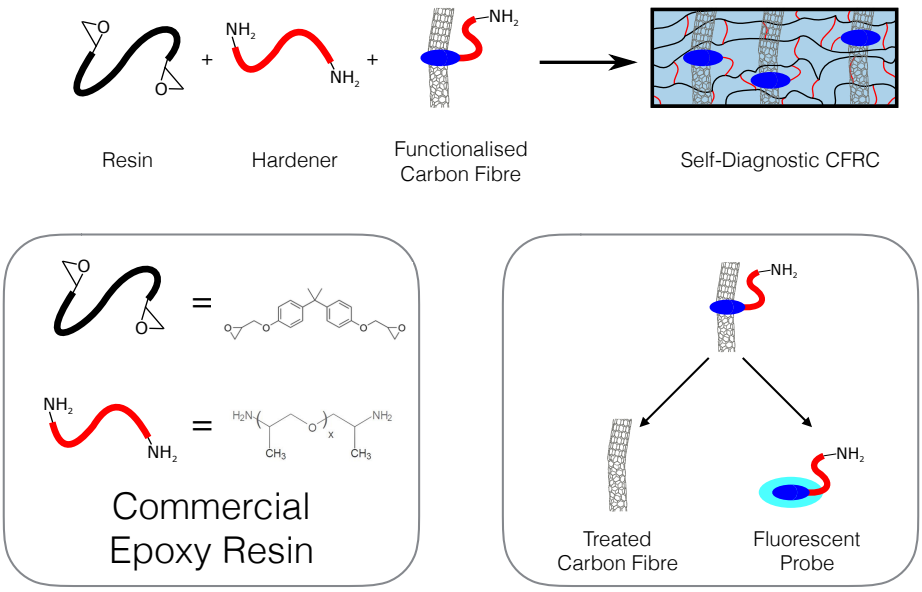

Figure 27: Schematic representation of a CF-nanohybrid based system for self-diagnostic CFRCs.

As clearly visible, the fibre consists of imperfect graphene sheets, ordered in an imperfect, but graphite-like, structure. Other materials with graphite-like microstructures, such as graphene,[101] fullerenes,[102] single-walled carbon nanotubes SWCNTs,[103, 104] multi-walled carbon nanotubes (MWCNTs)[105] and graphite[106] are known to form nanohybrids with polycyclic aromatic hydrocarbons (PAHs), thereby altering the photophysical properties of the involved PAH. Those nanohybrides are hold together by strong π-π stacking interactions between the extended π-electron system of the graphitic structure and the π system of the PAH. This leads to strongly altered electronic structure of the absorbed PAH, and as a result in a very different optical behaviour.[106]

No such system has been reported for CFs and PAHs, but based on the similarity to the known nanohybrid systems, it is reasonable to believe that such systems can be formed and that they behave in a similar manner. By using a PAH which is functionalised with a linker chain and a reactive end group, as shown in Figure 27, a self-diagnostic CFRC can be obtained. The fact that the self-diagnostic function in this case is located on the fibre/matrix interface makes this system interesting not only for the detection of damage in CFRCs, but also as probe for the investigation of debonding in CFRCs. Many fundamental questions in that field are still subject to research,[99] giving such a probe applications beyond the use in commercial materials.

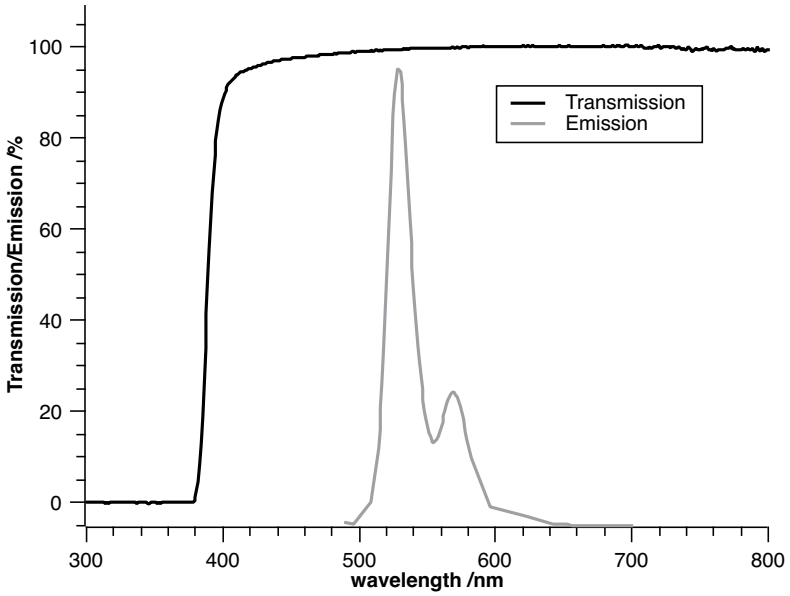

Figure 28: Transmission of epoxy resin EC 141 NF cured with curing agent W 241 (black) and fluorescence emission of PTCDA (grey).

5.2 Probe Design

As mentioned in section 5.1, a probe has to consist of a PAH, functionalised with a suitable linker chain and a reactive end group. For the PAH, beside the ability to form nanohybrides, the optical properties are of major importance. The absorbance and fluorescence emission need to be compatible with the transparency window of the used matrix. A transmission spectrum of a common, commercial epoxy system, based on BPA, is shown in Figure 28. The transmission rapidly decreases below 400 nm. Therefore, small PAH such as pyrene, who only absorb below 400 nm,[107] are not suitable in this case. Perylene on the other hand shows two of it's absorption maxima above 400 nm (at 408 nm and 435 nm in cyclohexane[107]), making it an ideal candidate for a fluorescent probe. Perylene-3,4,9,10-tetracarboxylic dianhydride (PTCDA) is, due to its use for the production of pigments[108] and as organic semiconductor,[109] readily available and affordable, and can be easily functionalised, thanks to the presence of two reactive carboxylic anhydrides. The functionalisation can take place on either one or both anhydrides, the double functionalisation being easier and therefore preferable.

As functional end groups, either a primary amine or an epoxide are suitable for the incorporation into epoxy thermosets. The linker group must be long enough to add some flexibility to avoid detachment of the probe during curing, but short enough to effectively transfer forces inside the polymer, resulting in detachment of the probe in those situations, and thereby turning on a fluo-

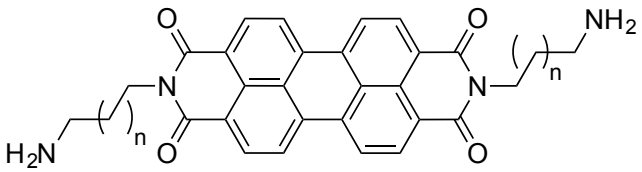

Figure 29: Structure of the proposed perylene probe for CF-nanohybrid based system for self-diagnostic CFRCs.

rescent signal. The functionalisation of PTCDA with an α,ω-diaminoalkane, such as 1,6-hexanediamine, is therefore an effective way to prepare a suitable probe for CF-nanohybrid based system for self-diagnostic CFRCs, such as the one shown in Figure 29. An effective, quick and high yield procedure for this functionalisation has been developed and can be found in section 5.5.1.

5.3 Nanohybrid formation

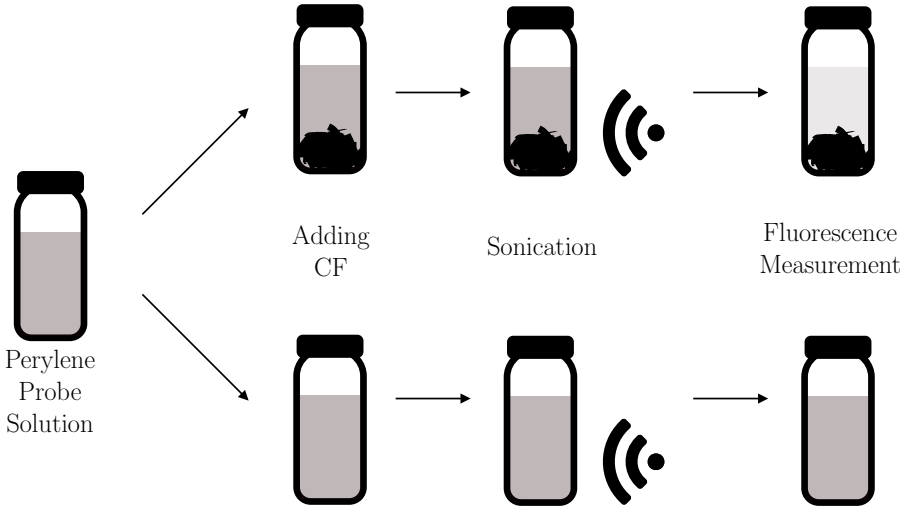

Figure 30: Procedure for the preparation CF-nanohybrids. A blank solution is treated in the same way as control.

Since CF-nanohybrids are unknown in literature, no readily available method for the preparation of such systems exits. However, due to the similarity with other carbon allotropes, it can be assumed that similar methods can be used. The newly developed method is therefore based on the one used by group of Dirk M. Guldi at the University of Erlangen-Nuremberg for the preparation of SWCNT-nanohybrids, documented for example in the PhD thesis of

Christian Ehli.[110] The method, consiting of separation of dye aggregates in tetrahydrofuran (THF) solution by ultrasound and subsequent absorption by π-π-interactions onto the fibres from the solvent is shown in Figure 30 and described detail in section 5.5.2. The absorption process can thereby easily be monitored by fluorescence measurements of the solution.

5.3.1 Inital tests

Different types of CFs, all of them obtained from ELANTAS Europe s.r.l. and of unknown type (type 1-3), where tested for their suitability for the preparation of CF-nanohybrids. The fibres where cut into small pieces and treated according to the procedure described in section 5.5.2. Monitoring the fluorescence of the PTCDA solutions and in this way the formation of nanohybrides showed for all tested fibres an increase of fluorescence emission, as visible in Figure 31.

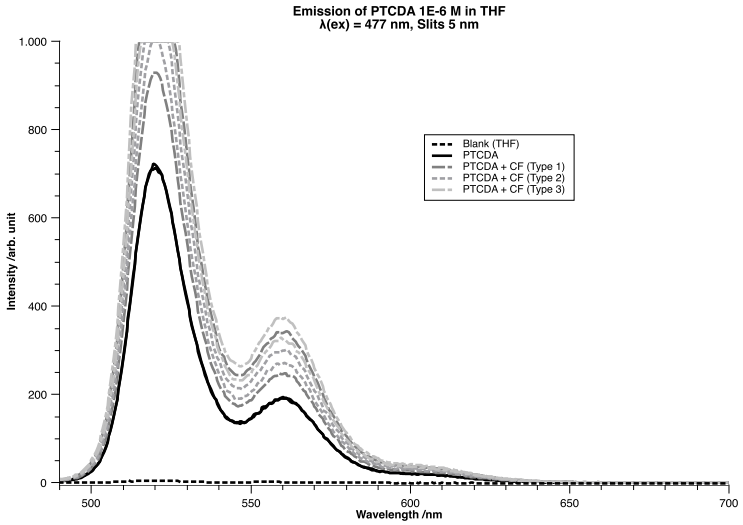

Figure 31: Emission spectra of PTCDA solutions used for the treatment of different types of CFs. In all cases, an increase of the fluorescence emission was observed after the treatment of the fibres.

This results lead to the conclusion that for all the obtained CFs no formation of nanohybrides is taking place. The observed increase in emission is likely due to the further separation of dye aggregates during the absorption process.

5.3.2 Fibre treatment

Based on the results shown in section 5.3.1, the formation of CF-nanohybrids with perylene based systems seems not possible. However, a thorough investigation of the literature showed that commercially available CFs are, as shown in Figure 32, surface treated in order to increase the interaction between the fibres and the matrix. This treatment is usually an oxidation process[111], leaving surface of the fibres functionalised with hydroxyl groups. While this functionalisation is beneficial for the interaction between the fibres and the matrix, it is interfering with the formation of CF-nanohybrids.

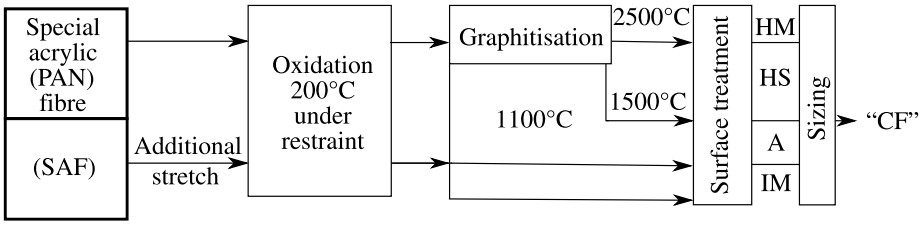

Figure 32: Schematic of the manufacture of high strength CF from PAN precursor. HM = high modulus (7 µm diameter), HS = high strength (7 µm), A = Type A (7 m), IM = intermediate modulus (5 µm). Taken from [112].

Attempts to obtain more details from literature about the manufacturing process of CFs or to obtain untreated fibres remained unsuccessful. Therefore, reduction of treated CFs offered a relatively simple way to obtain fibre without an oxidised surfaces, in order to test this hypothesis. No procedures for the reduction of CFs are published in literature, but due to the similarity to other carbon nanomaterials, procedures published for those material could be adapted. A vast number of procedures for the reduction of graphene oxide to graphene are available in literature.[113–115] A very simple and effective method is the treatment with hydroiodic acid,[116] which is described in section 5.5.3.

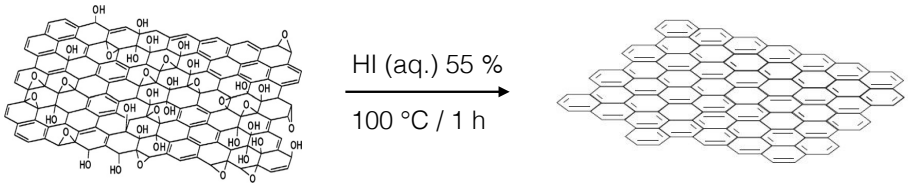

Figure 33: Reduction of graphene oxide to graphene. Adapted from [113].

Fibres treated in that way where tested in the same way as described above. In this case, as shown in Figure 34, the fluorescence of the solution was clearly reduced after the sonication. This leads to the conclusion that in this case the perylene system is absorbed onto the CFs, forming CF-nanohybrids, leading to self-diagnostic CFRC.

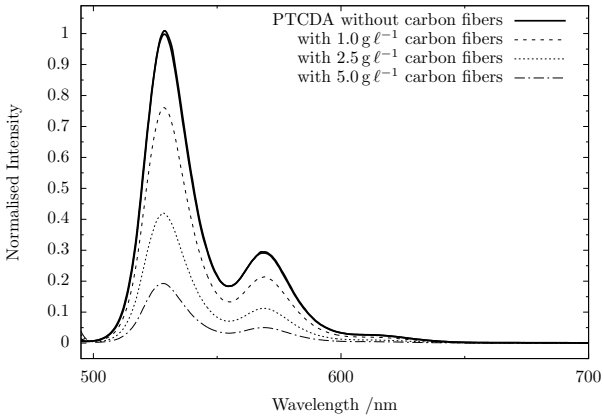

Figure 34: Absorption test with a saturated, filtered solution of functionalised PTCDA in THF, absorption time 2 h.

5.3.3 Testing in Epoxy Matrix

In order to test the suitability of the obtained CF-nanohybrids for the use in self-diagnostic CFRCs, CF-nanohybrids were embedded into a commercially available epoxy thermoset (epoxy resin EC 141 NF with curing agent W 241, obtained form ELANTAS Europe s.r.l., data sheet available in Appendix D). Samples prepared in that way, shown in Figure 35 and Appendix F, were subsequently broken using a universal testing machine.

Figure 35: Broken and intact samples of epoxy thermoset with (bottom) and without (top) CF-nanohybrids.

The fluorescence of the samples was surveyed before and after braking using fluorescence microscope as described in section 5.5.4. The images shown in Figure 36, taken from a sample containing CF-nanohybrids, show that after breaking the sample, a clear fluorescence signal is visible close to the breaking edge. Before breaking the sample, only a weak background signal is visible. Samples without CFs or containing unfunctionalised CFs show no fluorescence. See Appendix F for other images.

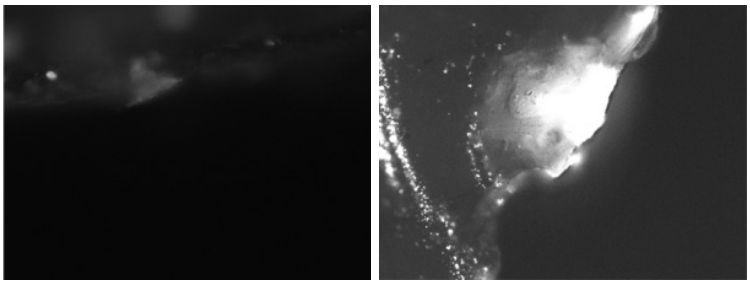

Figure 36: Fluorescence microscope pictures of the edge of intact (left) and broken (right) samples of a self-diagnostic CFRCs, containing CF-nanohybrids.

5.4 Conclusions

As shown in this section, CF-nanohybrids can, analogous to nanohybrids of other carbon materials, be formed. However, commercially available, surface treated CFs are not directly suitable for this process. In order to form nanohybrids, the oxidised surface of commercial CF need to be reduced; this can be performed by boiling CFs in concentrated hydroiodic acid.

Nanohybrids can be formed by sonication of reduced CFs in a THF solution of the perylene probe, the process can be monitored by measurement of the fluorescence emission of the solution.

Self-diagnostic CFRCs can be prepared using CF-nanohybrids instead of pristine CFs. Material prepared in this way show no fluorescence after preparation, but an intense fluorescence is visible by irradiation with a suitable wavelength after breaking the samples.

5.5 Experimental section

5.5.1 Synthesis of Perylene Probes

Bis(6-aminohexyl)-3,4,9,10-perylenetetracarboxy-3,4,9,10-diimide

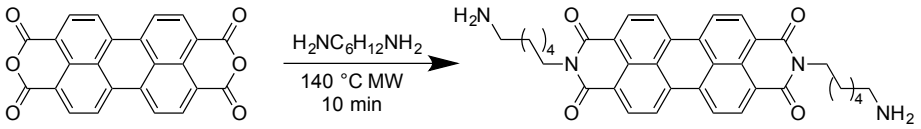

PTCDA (337 mg, 0.86 mmol) was suspended in 1,6-diaminohexane (6 mℓ) and in the microwave heated to 140 °C (P_{max} = 300 W) for 10 min in a sealed tube. The obtained crude was poured into water, the solid was filtered off and washed with water. The obtained soild was dried *in vacuo*, yielding the product as a dark purple solid (500 mg, 99 %). ^{1}H (300 MHz, DMSO-d$_6$ + TFA[1]) δ: 1.37 (bs, 8 H), 1.58 (bs, 8 H), 2.77 (bs, 4 H), 3.94 (bs, 4 H), 8.01 (bm, 8 H); MS (ESI) m/z: [M + H]$^+$ calcd for $C_{36}H_{37}N_4O_4$, 589.28; found, 589.26.

Other perylene probes
Perylene probes with other linker lengths can be synthesised replacing 1,6-hexanediamine with a suitable diamine. Bis(5-aminopentyl)-3,4,9,10-perylenetetracarboxy-3,4,9,10-diimide and bis(8-aminooctyl)-3,4,9,10-perylenetetracarboxy-3,4,9,10-diimide have successfully been prepared in quantitative yields using the same procedure.

5.5.2 Preparation of Nanohybrids

A suitable amount of of the perylene derivate is suspended in THF and sonicated, under frequent agitation, for at least 2 h. The obtained solution is filtered using a syringe tip filter unit (preferably with poly(1,1,2,2-tetrafluoroethylene) (PTFE) membrane with a pore size of 0.45 µm, but other filters can be used), and, together with carbon fibres, placed in a sealed container. The container is placed in an ultrasonic bath and sonicated, the temperature of the water is thereby kept below 20 °C by frequent additions of ice. The absorption process is monitored by measurements of the fluorescence of the solution, and the process stopped once the fluorescence remained stable. The fibres where removed from the solution, washed with THF and dried in air. Nanohybrides obtained in this way where processed as conventional CFs.

5.5.3 Treatment of Carbon Fibres

CFs were submerged in hydroiodic acid (57 %) in a pyrex tube and heated in the sealed tube to 100 °C for 1 h. The fibres were removed from the acid, washed

[1]Non-deuterated TFA was used to increase the solubility. Proper looking and shimming on the solvent mixture was not possible, leading to very broad signals.

with water until the washing water remained neutral an colourless, and dried in the oven at 100 °C.

5.5.4 Fluorescence Measurements

Spectra were recorded on a PerkinElmer LS 55 Fluorescence spectrometer using FL WinLab.[94] Data was plotted using Gnuplot.[95]

Following the mechanical treatment, the samples were examined using a Nikon XXX (Nikon Corp., Tokyo, Japan) equipped with an UV-1A ultraviolet excitation filter block (Nikon Corp., Tokyo, Japan; Excitation filter wavelengths: 475490 nm (bandpass, 483 CWL); Polychromatic mirror: 500-540 nm (bandpass) and 575-660 nm (bandpass); Barrier filter wavelengths: 503-530 nm (bandpass, 517 CWL) and 580-620 nm (bandpass, 600 CWL)) and a XYZ camera (Nikon Corp., Tokyo, Japan). Pictures were taken and processed using ImageJ.[97]

6 Cucurbit[8]uril complexes as probes for self-diagnostic epoxy thermosets

6.1 Introduction

Cucurbit[n]urils (CB[n]) are a class of macrocyclic compounds, synthesised by the condensation reaction between glycoluril and formaldehyde.[27] The most common form, cucurbit[6]uril (CB[6]), consists of 6 glycoluril units linked by 12 methylene bridges. Beside this, CB[n] with 5, 7, 8, or 10 glycoluril units are known.[28–30] The diameter of the cavity is increasing with the number of glycoluril units.

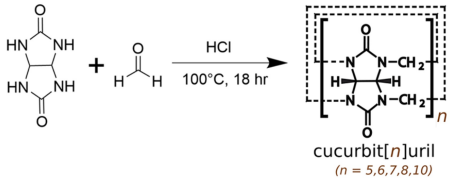

Figure 37: Reaction between glycoluril and formaldehyde, yielding CB[n]. Taken from Reference [32].

CB[n] are able to form a variety of complexes; some examples are shown in Figure 38. Number and position of the guest(s) is thereby depending on the diameter of the cavity and the nature of the guest(s). The major contribution to the binding of the guest is the presence of the highly hydrophobic inner cavity, which contains so called high-energy water, which is enthalpically

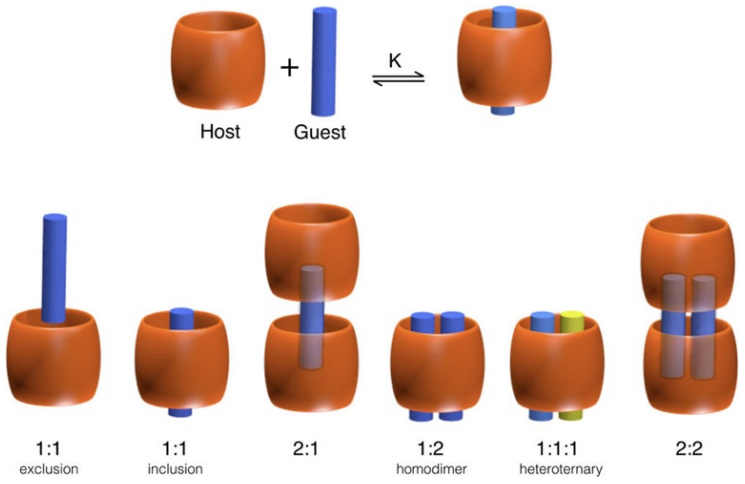

Figure 38: CB[n] inclusion and exclusion complexes. Taken from Reference [32].

and entropically unfavourable water molecules in the CB[n] cavities, not able to form hydrogen bond networks. This water molecules are by complexation superseded from the cavity, making the inclusion of guests, in the aqueous phase, highly favourable.[117] Moreover, the presence of carbonyl groups with a partial negative charge on the rims allow dipole-dipole and dipole-ion interactions with positively charged polar and ionic compounds. Therefore, small, doubly cationic molecules such as 1,1-di(hydrocarbyl)-4,4'-bipyridinium salts (viologens) are particularly good guests for CB[n].

From an physico-chemical point of view, 1:2 homodimeric and 1:1:1 heteroternary complexes are of particular interest; in those cases, two guests are forced into spacial proximity due to the complexation, favouring the interactions. In order to form those complexes, a CB[n] with a relatively large cavity, cucurbit[8]uril (CB[8]) or bigger, is needed. Based on the experience gained form the search for a suitable cavitand based system, described in sections 3 and 4, the search for suitable complexes for epoxy thermosets was performed starting from complexes known to show fluorescence quenching upon complexation. The main focus was, due to the experience with the cavitand based system, not on the design of new probes, suitable for the incorporation into the polymer network, but on testing the compatibly of the fluorophores with the epoxy matrix.

6.2 Pyrene - Viologen - CB[8] heteroternary complex

Two different systems using the interaction of pyrene as a fluorophore with 1,1-di(hydrocarbyl)-4,4'-bipyridinium salts (viologens) are described in literature. [118, 119] Both of them use the pyrene in the form of a 1-pyrenemethylammonium derivate, and discussion with Oren Scherman for the University of Cambridge revealed that the presence of the charged nitrogen species is essential to obtain the desired quenching of the fluorescence. Since no such compound was readily available, the compounds shown in Figure 39 were synthesised.

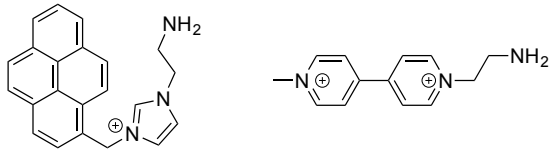

Figure 39: Pyrene (left) and viologen (right) used in the testing of the pyrene-viologen-CB[8] heteroternary complex.

Formation of the complex was first studied in water. As shown in Figure 40, a change in fluorescence is visible in the presence of CB[8] and the viologen, indicating that the complex is formed in the aqueous phase and that the compound could be suitable for the development of self-diagnostic polymers.

Transfer of the system into the epoxy phase was attempted with the procedure described in section 6.7.1. However, cured samples containing the pyrene-

viologen system showed no fluorescence emission, even for the pyrene in absence of any other components, leading to the conclusion that the compound is not compatible with the epoxy matrix. A closer investigation of the polymeric matrices used showed that the fluorescence of most pyrene derivates is most likely outside the transparent window of epoxy thermosets, making it impossible to observe a signal even if the pyrene compound is not destroyed by the matrix (Figure 28).

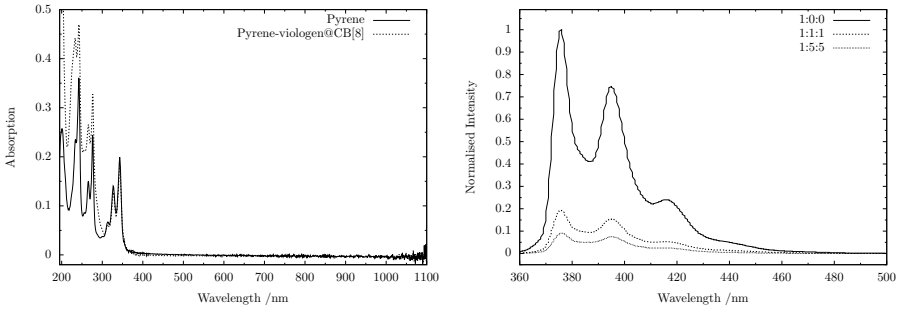

Figure 40: Absorption spectra of the pyrene and (pyrene + viologen)@CB[8] (1:1:1) in H_2O ($c = 1 \times 10^{-5}\,\mathrm{mol}\,\ell^{-1}$) (left) and Emission spectra of the pyrene in H_2O ($c = 5 \times 10^{-7}\,\mathrm{mol}\,\ell^{-1}$, $\lambda_{ex} = 342\,\mathrm{nm}$)) in the absence (1:0:0), equimolar presence (1:1:1) and with a five-fold excess (1:5:5) of viologen and CB[8](right). Addition of an excess of viologen and CB[8]leads to a slightly better quenching, likely due to weigthing inaccuracies for CB[8].

6.3 Methylene blue - CB[8] homodimer complex

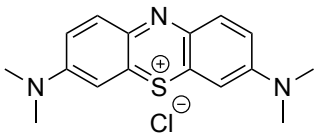

Figure 41: Structure of methylene blue.

A paper by Sun *et al.* showed the use of a homodimer consisting of two methylene blue molecules as guests inside a CB[8] as probe for the detection of paraquat (N,N'-dimethyl-4,4'-bipyridinium dichloride).[120] Due to the proximity inside the CB[8], the two methylene blue molecules are quenching their respective emission and absorption. Paraquat, which is an exceptionally good guest for CB[8], is displacing the methylene blue guests, and thereby restoring its fluorescence, giving way to an easy mode of detection. The change in absorbance can be easily demonstrated using a red laser pen ($\lambda_{max} = 625\,\mathrm{nm}$), as shown in Figure 42. Complexed methylen blue no longer absorbs the red light of the laser, making it clearly visible.

Upon transfer of this system into either component of the epoxy system, the colour changed from dark blue to pale pink. No fluorescence emission was observed after curing of the system, indicating that either the epoxy resin or the amine curing agent are reacting with methylene blue.

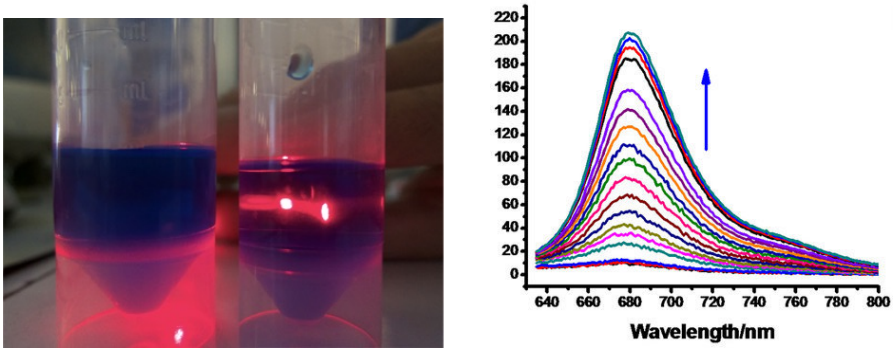

Figure 42: Absorption of an laser pen ($\lambda_{max} = 625\,\mathrm{nm}$) by aqueous solutions of methylene blue in the absence (left) and presence (right) of a half an equivalent of CB[8] (left). Emission spectra of (2 methylene blue)@CB[8] ($5 \times 10^{-6}\,\mathrm{mol\,dm^{-3}}$, $\lambda_{ex} = 620\,\mathrm{nm}$) upon addition of 0 to 50 equivalent of paraquat (right). Right image taken from [120].

6.4 Thiazole orange- viologen - CB[8] heteroternary complex

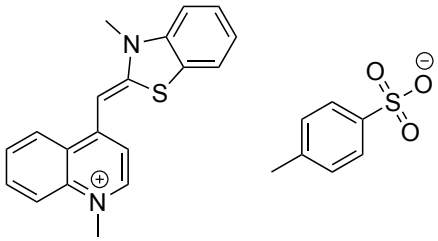

Figure 43: Structure of thiazole orange.

Thiazole orange (1-Methyl-4-[(3-methyl-2(3H)-benzothiazolylidene)methyl]-quinolinium p-tosylate) is a fluorescence dye widely used in biology for nucleic acid detection.[121, 122] In literature,[123] the interactions of thiazole orange and various CB[n] has been described, leading to the formation of linear supramolecular polymers and a change in the optical properties (Figure 44). Fluorescence investigations of thiazole orange with N,N'-dimethyl-4,4'-bipyridinium diiodide (MV) and CB[8] in water, shown in Figure 45, showed that com-

plexation leads to a clear change in colour and fluorescence, making this system eligible for the use in self-diagnostic polymers.

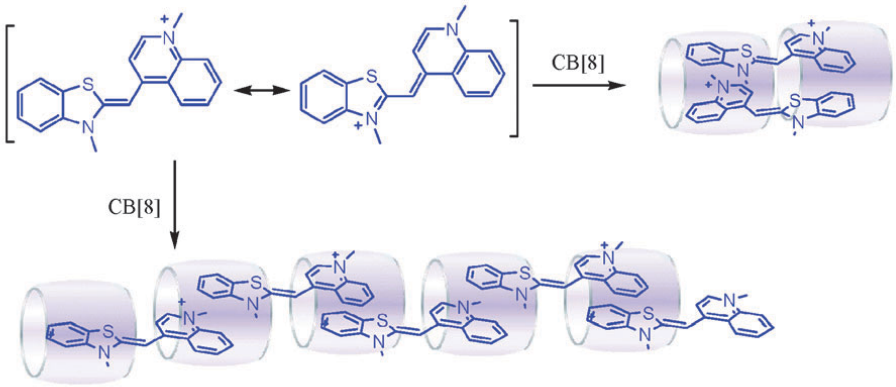

Figure 44: Supramolecular assemblies of thiazole orange and CB[8] as proposed by Xu *et al.*. Taken from [123].

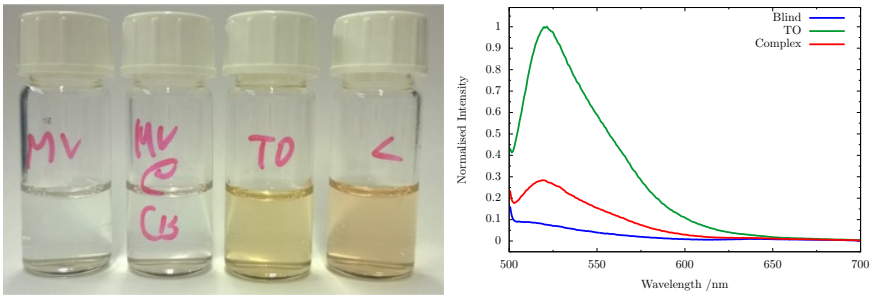

Figure 45: Picture of aqueous solutions of (form left to right) MV, MV@CB[8], thiazole orange and (thiazole orange + MV)@CB[8] (left). Emission spectra of water (Blank), thiazole orange (green) and (thiazole orange + MV)@CB[8] solutions ($c = 1 \times 10^{-6}\,\mathrm{mol\,dm^{-3}}$, $\lambda_{ex} = 485\,\mathrm{nm}$)(right).

Incorporation of the complex into either component of the epoxy matrix, as described in section 6.7.1, led to destruction of the system and the fluorescent dye. No fluorescence emission was observed in cured samples, neither in the presence nor the absence of MV and CB[8].

6.5 Cyanine Dyes - CB[8] homodimer complexes

Cyanine dyes are a class of polymethines dyes, general structure shown in Figure 46, widely used in biology as fluorescent labels.[124, 125] By extending the polymethine chain and by change in the aromatic system, the absorption and

emission can be tailored to the specific needs, while the two R-groups allow easy functionalisation and thus covalent linkage of the dye.

Cyanine dyes are known in literature to form 1:1 complexes with cucurbit[7]uril (CB[7]),[126] as well as to undergo self-quenching in spacial proximity, [127] making them ideal candidates for the development of a probe for self-diagnostic polymers.

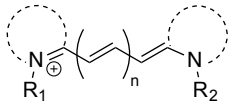

Figure 46: Generalised structure of cyanine dyes. Dashed lines are indicating quaternised heteroaromatic bases.

For the given experimental setup, which involves the fluorescence microscope with a FITC-TRITC filter cube, allowing the excitation between 540 nm and 565 nm, 1,3,3-trimethyl-2-((*E*)-3-((*E*)-1,3,3-trimethylindolin-2-ylidene)prop-1-en-1-yl)-3H-indol-1-ium (Cy3) with an absorption maxima at 558 nm[128] is the ideal choice. Since no derivate of Cy3 was readily available, a simple version, shown in Figure 47 was synthesised according to literature procedures.[129–131]

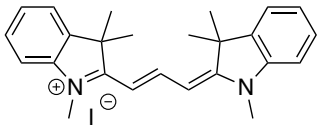

Figure 47: Structure of the Cy3 derivate used.

Preliminary tests in water, shown in Figure 48, were promising. However, transfer and curing in an epoxy system leads also in this case to destruction of the fluorophore.

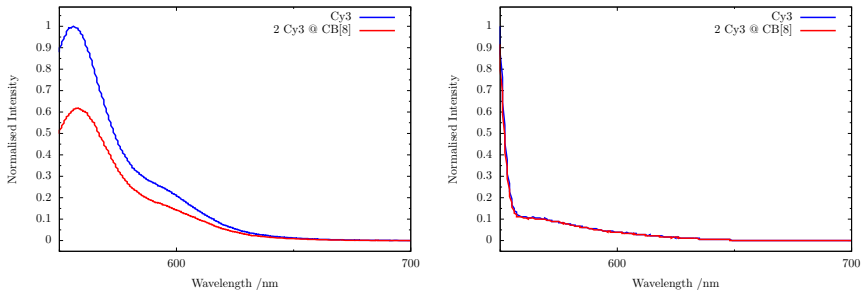

Figure 48: Emission spectra of Cy3 and Cy3@CB[8] in a water (left) and in EC141NF/W241 epoxy system (right).

6.6 Conclusions

As shown in this section, the transfer of CB[n] complexes from an aqueous phase into a epoxy type thermoset is rather difficult. The high reactivity of the components of the epoxy systems are the main obstacles on the quest for a suitable, CB[n]-based probe. In order to be able to work in the transparency window of the polymer, classical fluorescence dyes, absorbing and emitting in the visible range, are needed. Those dyes however are usually charged, heterocyclic compounds. The results obtained and presented in this section indicate however, that this class of compounds is very reactive towards the components of commercial epoxy systems, and therefore not suitable for standard amine-cured epoxy systems.

6.7 Experimental section

The essential step for the testing of CB[n] based complexes in an epoxy matrix is the transfer of the complex into a component of the matrix. Since water is, as explained in section 6.1, the driving force for the formation of CB[n] complexes, the complexes are preformed in water and subsequently transferred by evaporation into one of the components of the used two component epoxy system. The epoxy component containing the CB[n] complex is subsequently used for the preparation of an epoxy thermoset as directed by the manufacturer. The data sheet with curing conditions can be found in Appendix D.

6.7.1 General Procedure for the Transfer of CB[n] Complexes into Epoxy Systems

Aqueous solution of the components, usually of a concentration of $10^{-4}\,\mathrm{mol\,dm^{-3}}$ for the guests and $10^{-5}\,\mathrm{mol\,dm^{-3}}$ for the CB[n], where prepared using ultrapure water. Suitable amounts of those solutions where mixed together, then thoroughly mixed with a suitable amount of one of the epoxy components, usually the curing agent. The amount of the epoxy component was calculated in order to obtain the desired concentration in the final, cured thermoset, usually around $1 \times 10^{-6}\,\mathrm{mol\,kg^{-1}}$. The obtained emulsion was placed in the oven at 120 °C and homogenised frequently during the evaporation process. Once the component appeared completely transparent, the sample was removed from the oven and cooled to room temperature. The component containing the CB[n] complex is subsequently used as directed by the manufacturer.

6.7.2 Fluorescence Measurements

Polymeric samples for fluorescence measurements were cured at 40 °C overnight directly in cuvettes made of poly(methyl methacrylate) (pathlength 10 mm, Sigma-Aldrich Z188018). Spectra were recorded on a PerkinElmer LS 55 Fluorescence spectrometer using FL WinLab.[94]
Data was plotted using Gnuplot.[95]

7 Cucurbit[8]uril–perylene–azobenzene ternary complex as probe in self-diagnostic epoxy thermosets

7.1 Introduction

Based on the data presented in section 6, a neutral, non-heterocyclic system was searched as probe for self-diagnostic epoxy thermosets, with absorption and emission inside the transparency window of the used epoxy system. From the work with CF-nanohybrids described in Section 5, it turned out that PTCDA-derivates are stable towards curing conditions of the used epoxy thermosets and that their fluorescence persisted after curing of the samples. PTCDA-derivates are furthermore known to form excimers under suitable conditions,[132–134] which alter the fluorescence emission of the system. Based on this knowledge, it could be possible to use the spacial proximity of two PTCDA-derivate guests in a single CB[n] host to observe a strong excimer emission, and that the emission of the individual PTCDA could be restored by separation of the complex. However, a paper by Biedermann *et al.* [135] shows that only one perylene guest can be accommodated inside the cavity of CB[8], as shown in Figure 49. CB[n] derivates with bigger cavities, even though existing, are hard to obtain. The same paper mentions as a side note that the formation of heteroternary complexes with dibenzofuran- or azobenzene-derivates as the second guest leads to a quenching of the fluorescence emission of the perylene guest.

7.2 Probe Design

Since the probe reported by Biedermann *et al.* was not readily available, a simplified version of the system was synthesised. For the perylene bearing part, as for the original probe, PTCDA was selected as core. In order to facilitate the separation of the complex under stress/strain, monofunctionalisation is in this case preferred. For the incorporation into epoxy thermosets, either a primary

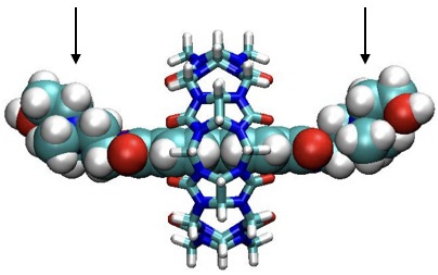

Figure 49: Geometry optimised structure for the system used by Biedermann *et al.* at DFT-B3LYP/6-31G* level of theory. Positions of the charged nitrogens are indicated by arrows. Adapted from Reference [135].

amine or an epoxide are suitable reactive end groups. Due to the poor solubility of PAHs, it is a advisable to choose a linker group which increases the solubility to connect the perylene core with the reactive end group.

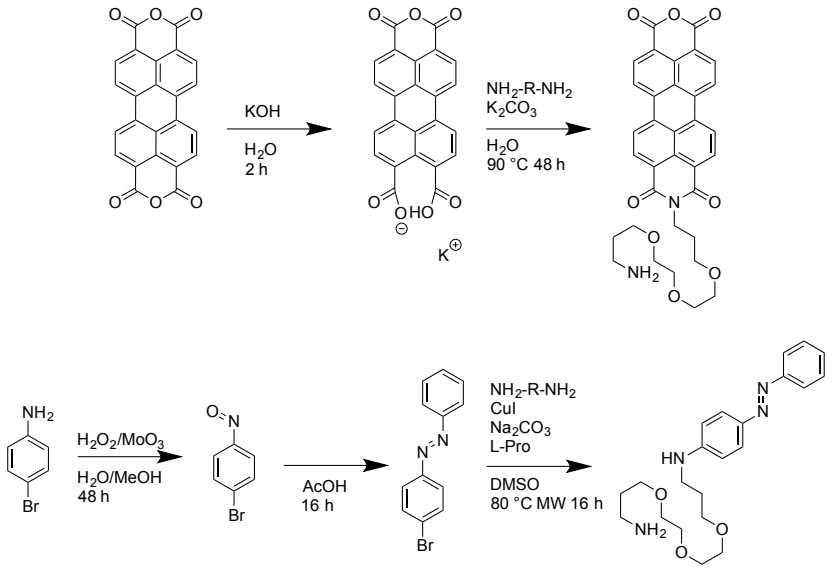

Scheme 2: Synthetic pathways for the preparation of the perylene and azobenzene based guests.

Therefore, the functionalisation of monoactivated PTCDA with a short, α,ω-diamino-terminated glycol leads to a suitable perylene compound, as shown in Scheme 2. This can be achieved by mono activating the PTCDA by opening one of the anhydrides with potassium hydroxide and subsequent reaction with the previously mentioned α,ω-diamino-terminated glycol. In this proposed guest, unlike in the one used by Biedermann *et al.*, no charged ammonium function is present; they have been omitted on purpose since they are likely to increase the reactivity towards the components of the epoxy system. A model of perylene@CB[8], visible in Figure 49, shows furthermore that the charges in the probe used by Biedermann *et al.* are located far from the CB[8]-host, which makes it likely that they have no major impact on the complexation of the perylene-guest.

For the second guest, the azobenzene was chosen over the dibenzofurane due to the availability of starting materials. Like in the case of the first guest, also here a linker group increasing the solubility as well as a reactive end group must be present. Therefore, the functionalisation of a halogenated azobenzene, which can be selectively synthesised by coupling of nitroso-benzene with an aniline, with a short, α,ω-diamino-terminated glycol by Ullmann-type coupling, using Cu(I) with *L*-proline as ligand, can lead to a suitable azobenzene guest, as shown in Scheme 2.

The synthesis of the individual compounds is described in section 7.7.1.

7.3 Initial Testing

In order to test the suitability of the newly designed system, a fluorescence titration experiment in water was performed. As shown in Figure 50, addition of equimolar amounts of CB[8] and the azobenzene guest (AB) to the perylene guest (Per) led to only a minor decrease in fluorescence emission and to a slight redshift of the emission. However addition of bigger amounts of AB leads to a further decrease in fluorescence. This behaviour could be explained by the presence of an equilibrium, as shown in Equation 11, in which the presence of Per@CB[8] + AB is favoured over the formation of heteroternary complex Per+AB)@CB[8]. Therefore, a large excess of AB is needed to obtain the desired heteroternary complex

$$CB[8] + Per + AB \rightleftharpoons Per@CB[8] + AB \rightleftharpoons (Per + AB)@CB[8] \quad (11)$$

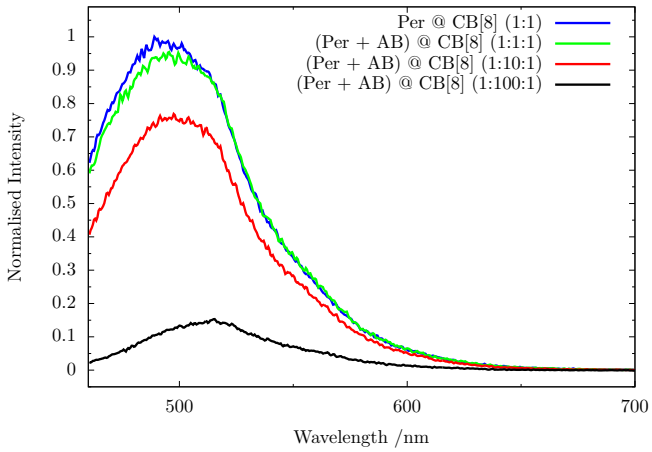

Figure 50: Emission spectra of (Per + AB)@CB[8] in a water system ($c(Per) \approx 1 \times 10^{-6}\,\mathrm{mol\,dm^{-3}}$, $\lambda_{ex} = 450\,\mathrm{nm}$).

After this first positive results, the system was transferred into an epoxy matrix using the method described in section 7.7.2. Excitation/emission maps were recorded to find the ideal settings for future measurements. The fluorescence characterisation, shown in Figure 51, shows that in this case, the fluorescence persists in the polymer. Furthermore, also the quenching in the presence of an equimolar amount of CB[8] and an excess of AB is still present, making this system a promising candidate for the development of self-diagnostic epoxy thermosets.

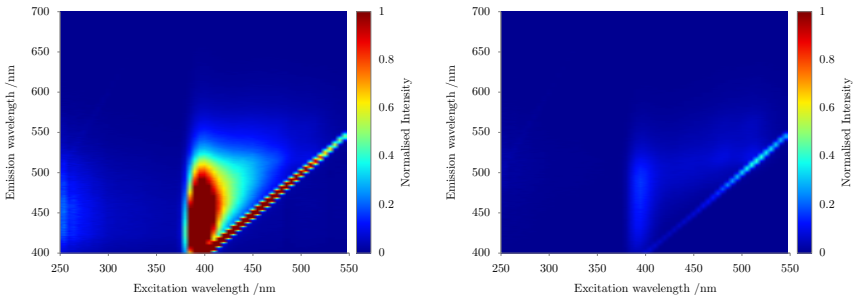

Figure 51: Emission spectra of a Per (left) and (Per+AB)@CB[8] (1:100:1, right) in a EC141NF/W241 epoxy system ($c(Per) \approx 1 \times 10^{-6}\,\mathrm{mol\,kg^{-1}}$).

7.4 Testing of the self-diagnostic properties

In order to test the suitability of the newly developed system for the use in self-diagnostic epoxy thermosets, samples, as shown in Figure 52, with $c(Per) \approx 1 \times 10^{-6}\,\mathrm{mol\,kg^{-1}}$ and a ratio Per:AB:CB[8] of 1:100:1 in a EC141NF/W241 epoxy system were prepared. This was done by pre-preparing the complex in water, mixing of the aqueous solution with the curing agent followed by evaporation of the water and subsequent curing of the samples, as described in detail in Section 7.7.2. Samples were prepared with and without CF fabric added, which was added to increase the force needed to break the samples.

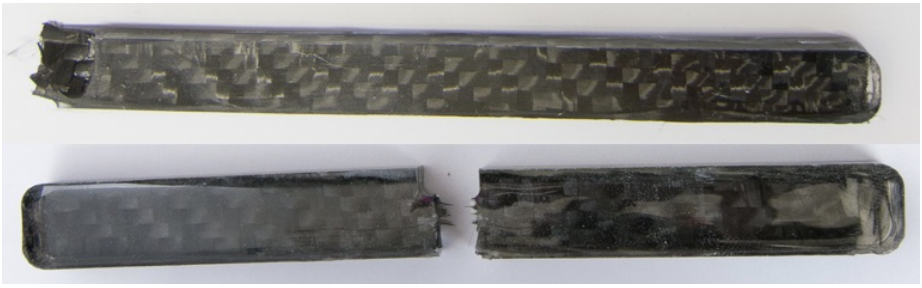

Figure 52: Samples used for testing of the self-diagnostic properties before (top) and after (bottom) breaking. Samples are prepared from EC141NF/W241 with $c(Per) \approx 1 \times 10^{-6}\,\mathrm{mol\,kg^{-1}}$ and a ratio Per:AB:CB[8] of 1:100:1.

Samples were investigated with the fluorescence microscope before and after breaking with a universal testing machine, and typical images before and after breaking are shown in Figure 53. In CF reinforced samples, a certain background fluorescence was present in intact sample, likely due to incomplete complexation of the Per guest. However, a clear increase of the fluorescence along the breaking edge was observed after breaking. The presence of fluorescence only in this region is likely due to the fact that a very rigid thermoset was used, in which

very little deformation is taking place before breaking. In samples not reinforced with CF, the turn-on of the fluorescence was hardly noticeable, likely because of the present background fluorescence. These results indicate that this self-diagnostic probe is more suitable for strain detection than for crack monitoring.

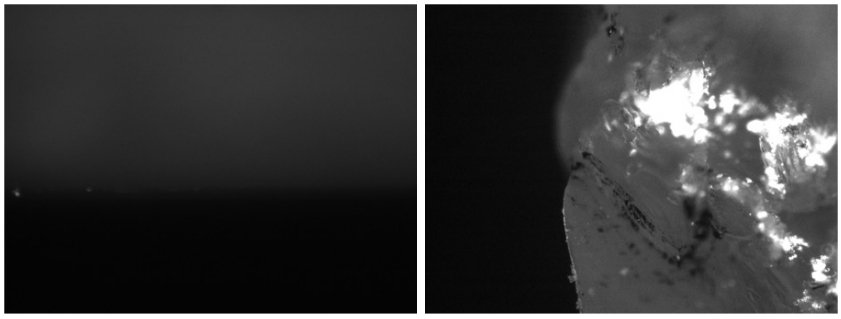

Figure 53: Fluorescence microscope images of the crack region of samples used for testing of the self-diagnostic properties before (left) and after (right) breaking. Additional fluorescence pictures of samples can be found in Appendix H.

7.5 Conclusions

In this section, the design, synthesis and characterisation of an (Per+AB)@CB[8] based probe for the use epoxy thermosets has been demonstrated. In addition, it has been shown that this probe can be transferred into an epoxy matrix and that the optical properties persist also in this matrix.

In additions, it has been successfully demonstrated that self-diagnostic materials can be prepared using the proposed (Per+AB)@CB[8] complex. Those materials show no fluorescence after preparation, but an intense fluorescence is visible by irradiation with a suitable wavelength after breaking the samples, giving a tool to indicated areas in polymers where high strains/stress is present. The fluorescence detection of cracks is persistent over time, therefore allowing the the detection of microfissures long after they occurred.

7.6 Outlook

As visible in Figure 52, samples containing the (Per+AB)@CB[8] systems are, due to the relatively high content of AB, slightly yellow. Depending on the application, this could be a problem for the user. In addition, the usage of the high concentration of AB is also an economical factor.

Use of a dibenzofurane based quencher, as the one used by Biedermann *et al.* [135], which can be expected to be colourless, could eliminate the problem caused by the colour of AB. In addition, dibenzofurane based quenchers showed a more efficient quenching over azobenzene quenchers in [135], therefore possibly reducing the excess of quencher needed.

As an alternative solution, the binding equilibrium, shown in Equation 11, could be optimised. The system mentioned in the paper of Biedermann *et al.* [135] exhibited an more efficient quenching of the fluorescence. Therefore, a system which closer resembles the system of Biedermann *et al.*, possibly with the charged ammonia groups shown in Figure 2 present, could maybe exhibit a more efficient quenching, since the charges may have an influence on the equilibria proposed in Section 7.3. It has yet to be tested if charges outside of an aromatic systems lead to the same problems with reactivity described in Section 6.6.

7.7 Experimental Part

7.7.1 Synthesis

(*E*)-1-(4-bromophenyl)-2-phenyldiazene
(*E*)-1-(4-bromophenyl)-2-phenyldiazene was prepared according to literature procedures[136, 137].

(*E*)-*N*-(3-(2-(2-(3-aminopropoxy)ethoxy)ethoxy)propyl)-4-(phenyldiazenyl)aniline
Procedure adapted from Reference [138]

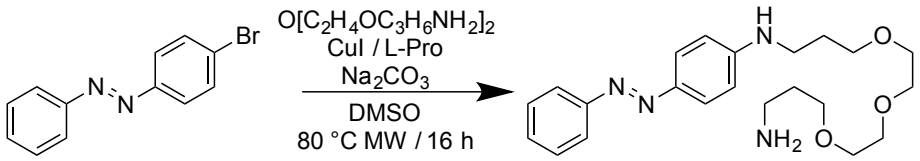

A mixture of (*E*)-1-(4-bromophenyl)-2-phenyldiazene (52 mg, 0.2 mmol) L-proline (46 mg, 0.4 mmol) copper(I) iodide (37 mg, 0.2 mmol) sodium carbonate (31 mg, 0.3 mmol) and 4,7,10-trioxa-1,13-tridecanediamine (1.75 mℓ, 7.9 mmol) in DMSO (2.3 mℓ) was heated under microwave irradiation for 16 h at 80 °C. DMSO and 4,7,10-trioxa-1,13-tridecanediamine were removed from the reaction mixutre and the remaining crude purified by flash chromatography (DCM/MeOH 9/1), yielding a orange solid (54 mg, 68 %). ^{1}H (300 MHz, $CDCl_3$) δ: 7.80-7.82 (m, 4H), 7.44-7.49 (m, 2H), 7.36-7.39 (m, 1H), 6.64–6.70 (m, 2H), 3.94 (bs, 4H), 3.31–3.61 (m, 14H), 2.61 (bs, 2H), 1.74–1.01 (m, 4H); MS (ESI) m/z: $[M + H]^+$ calcd for $C_{22}H_{33}N_4O_3$, 401.25; found, 401.26.

3,4,9,10-Perylenetetracarboxy-3,4-anhydride potassium salt
3,4,9,10-Perylenetetracarboxy-3,-anhydride potassium salt was prepared according to literature procedure[139].

9-(3-(2-(2-(3-aminopropoxy)ethoxy)ethoxy)propyl)-3,4,9,10-perylene-teracarboxy-3,4-anhydride-9,10-imide (Per)
Procedure adapted from Reference [139]

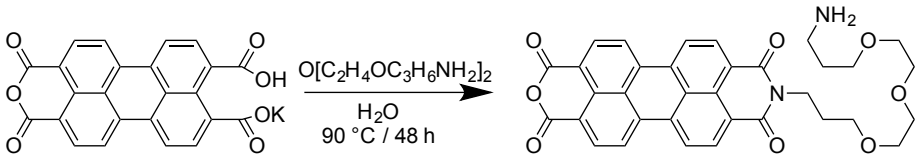

3,4,9,10-Perylenetetracarboxy-3,4-anhydride potassium salt (0.96 g, 2 mmol) and 4,7,10-trioxa-1,13-tridecanediamine (2.37 g, 10 mmol) were placed in a round bottom flask and water (40 mℓ) was added. The solution was stirred at 90 °C for 48 h before the addition of aqueous potassium carbonate (25 % w/w, 200 mℓ). The solution was heated at 90 °C for 3 h, over which time the colour changed from purple to green. The solid was filtered off and washed from the filter with a water (150 mℓ) and triethylamine (5 mℓ) mixture. The filtrate was diluted with HCl (2 mol dm^{-3}, 250 mℓ) and after sitting over night the precipitated solid was filtered off and washed with methanol. The product was obtained as a purple solid (0.77 g, 65 %) ^{1}H (400 MHz, DMSO-d$_6$) δ: 8.80 (d, J = 7.9 Hz, 2H), 8.47 (dd, J = 11.7, 8.0 Hz, 2H), 7.75-7.69 (m, 4H), 4.16-4.13 (m, 2H), 3.55-3.43 (m, 4H), 3.09 (dd, J = 7.1, 4.9 Hz, 2H), 2.83 (td, J = 6.4, 0.6 Hz, 2H), 1.93 (dd, J = 7.1, 6.4 Hz, 2H), 1.77 (dd, J = 13.2, 6.4 Hz, 2H); MS (ESI) m/z: $[M + H]^+$ calcd for $C_{22}H_{33}N_4O_3$, 595.21; found, 595.36.

7.7.2 Procedure for the Transfer of CB[8] Complexes into Epoxy Systems

The procedure descried in section 6.7.1 was applied. Samples were prepared to obtain a concentration of $c(Per) \approx 1 \times 10^{-6}$ mol kg^{-1} and a ratio Per:AB:CB[8] of 1:100:1.

7.7.3 Fluorescence Measurements

Spectra were recorded on a PerkinElmer LS 55 Fluorescence spectrometer using FL WinLab.[94] Data was plotted using Gnuplot.[95]

Following the mechanical treatment, the samples were examined using a Nikon XXX (Nikon Corp., Tokyo, Japan) equipped with an FITC-TRITC filter block (Nikon Corp., Tokyo, Japan; Excitation filter wavelengths: 475-490 nm (bandpass, 483 CWL); Polychromatic mirror: 500-540 nm (bandpass) and 575-660 nm (bandpass); Barrier filter wavelengths: 503-530 nm (bandpass, 517 CWL) and 580-620 nm (bandpass, 600 CWL)) and a XYZ camera (COMPANY). Pictures were taken and processed using ImageJ.[97]

Part II

Polymer Blending

8 Introduction

Triggered drug delivery, theragnostic devices, self healing polymeric insulators, phase separator membranes, are examples of applications that would benefit from polymeric film and matrices of controlled and tuned permeability. With this motivation, several systems have been proposed so far with response to light, pH, magnetic and electrical stimuli.[140]

Blending polymers is an economically attractive and convenient route to obtain materials with new, desirable properties.[141] Few polymers form homogeneous blends, while most polymers show low compatibility and thus microscopically segregate rather than forming a single-phase structure. Spreading of a solution of such immiscible polymers on a solid substrate produces a phase-separated film with a wide range of different possible morphologies, where horizontal segregation and/or vertical stratification can occur.[142–144] The final result depends on several factors:[145, 146] the physical properties of the polymers, the solvent and its evaporation speed, the hydrophilicity and roughness of the substrate, the temperature, *etc.*

By achieving control over a wide range of morphologies, it is possible to obtain a fine tuning of the physical properties of the system, *e.g.* their mechanical/thermal response[147], or the electrical percolation threshold when conductive nanostructures, such as graphene[148], carbon nanotubes[149, 150] or nanoparticles[151] are incorporated in one of the two phases.

Supramolecular interactions have been used to increase the interactions between different polymers, yielding uniform blends between otherwise incompatible polymers.[71, 152–154] By using a stimuli-responsive, supramolecular host-guest system as polymer compatibiliser for otherwise immiscible polymers, those interactions can be turned off, leading to a controlled disassembly of the blend. Tetraphosphonate cavitands form highly stable complexes with *N*-methylpyridinium compounds ($K_a = 5.8 \times 10^6\,\mathrm{M}^{-1}$ in 1,2-dichloroethane)[69] which can be dissociated both chemically[73] and electrochemically[155], making those systems ideal candidates for switchable host-guest polymer blends.

In previous studies[71, 156], the molecular recognition properties of tetra phosphonate cavitands were exploited to introduce supramolecular cross-links and, consequently, to induce the compatibilisation of two otherwise immiscible polymers, polystyrene (PS) and poly(butylmethacrylate) (PBMA). Host-Guest complexation in the polymer matrix has been demonstrated unambiguously with two control experiments, namely decompatibilisation driven by an ineffective PBMA-pyridine guest and by replacement with a competitive monomeric guest.[71] Upon compatibilisation, spin coated films of a 1:1 mixture of the polymers exhibited a macro- and microscopically uniform, flat surface. Phase separation was restored using either a competing agent[71] or pH,[156] as function of the nature of the polymeric guest. In both cases, the disassembly required dissolution of the blend in a suitable solvent. The procedure is unfeasible for practical

Parts of this chapter have been published in: Orsi, D.; Früh, A. E.; Giannetto, M.; Cristofolini, L.; Dalcanale, E. *Soft Matter* **2016**, *12*, 5353–5358

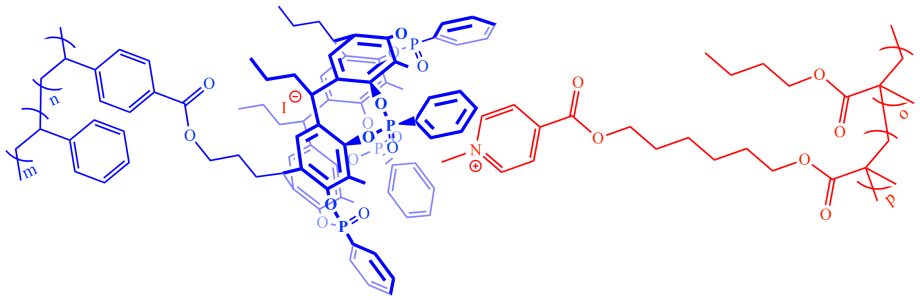

Figure 54: Structures of PS-HOST (left, blue) and PBMA-GUEST (right, red) copolymers.

applications, for which the stimuli-responsive decompatibilisation must work on the polymers in the solid state, either bulk or thin films. This work aims to test the ability to induce phase-separation directly in the solid phase by means of electrochemistry on supported films produced by means of either spin-coating or Langmuir techniques.

9 Materials and Methods

9.1 Compatibilisation of two immiscible polymers

The syntheses of PS-HOST and PBMA-GUEST incorporating 2.5 mol % and 8 mol % of cavitand host and *N*-methyl pyridinium guests respectively (Fig. 54) were described previously.[71]

9.2 Deposition on gold substrate

Films of 1:1 molar mixtures of PS-HOST and PBMA-GUEST were prepared using spin coating (SC) and Langmuir-Schaefer (LS) deposition techniques.

9.2.1 Spin coating

A drop of a 0.5 mM dichloromethane solution of a 1:1 mixture of PS-HOST and PBMA-GUEST 2.5 mol % was cast on a 1 cm^2 gold substrate spinning at 1500 rpm on a Chemat Technology Spin Coater KW-4A.

9.2.2 Langmuir-Schaefer films

LS films have been deposited using a KSV5000 Langmuir trough with maximum surface $A = 300\,cm^2$. A 0.5 g ℓ^{-1} 1:1 chloroform-hexane solution of a 1:1 molar mixture of the two polymers (8 mol % functionalisation) was spread at room temperature on pure water (resistivity $\geq 18.2\,M\Omega\,cm$). The film was compressed up to a deposition surface pressure $\Pi = 7.5\,mN\,m^{-2}$; at this pressure,

the surface pressure – area isotherm shows that the film has reached its compact phase. Compression was stopped, the Wilhelmy balance was removed and the surface was partitioned using plastic masks with rectangular holes. Using the LS deposition technique, up to 20 layers were transferred on 1 cm^2 gold substrates.

9.3 Null-ellipsometry

Null-ellipsometry was performed using an Optrel Multiskop ellipsometer in the PCSA configuration, equipped with a 5 mW laser at 633 nm. Inversion of the ellipsometric angles Δ and Ψ to retrieve sample thickness was performed using the effective medium approximation (EMA)[157] assuming a common value for the refractive index of the film ($n = 1.58$), equal to the average value of the refractive index for PS and PBMA.

9.4 Atomic Force Microscopy

Surface topography was examined, at a controlled temperature of 21 °C, using an atomic force microscope Thermomicroscope Autoprobe CP Research equipped with a small-area (5 µm × 5 µm) scanner. All measurements were performed in contact mode employing silicon nitride probes (Veeco OTR4-35, typical spring constant 50 mN m^{-1}). The images were analysed using ThermoMicroscopes' proprietary software[158], Gwyddion[159], and in selected cases our own code developed in Matlab.

The thickness of the films were measured using AFM and null-ellipsometry. Fig. 55a shows the topography of a portion of a SC sample where the film was partially removed by scratching it with a toothpick soaked with solvent; the film height is found to be of 40 nm to 50 nm. Fig. 55b shows the analogous AFM topography of a scratched LS film made of 20 layers: we find a thickness of approximately 16 nm.

The height profiles measured along the black segments shown in Fig. 55a+b, both corresponding to a length of 1.5 µm, are reported in Fig. 55c. Null-ellipso metry measurements performed on LS samples with increasing number of layers confirm the results of the AFM measurements, as shown in figure Fig. 55d: Data are compatible with a thickness-per-layer of (0.9 ± 0.1) nm (dashed line).

9.5 Electrochemistry

Electrochemical treatments of the polymeric films were performed using a Eco Chemie PGSTAT 20 electrochemical workstation controlled by a customised version of Autolab GPES[160]. Square 1 cm^2 gold plates with deposited polymer films were used as working electrodes in a 10 mℓ cell equipped with a platinum rod and an Ag/AgCl/3 M KCl as counter and reference electrodes, respectively. 0.1 mol ℓ^{-1} NaCl in water was used as electrolyte. Two different protocols, mainly differing in the potential scan modes, were used:

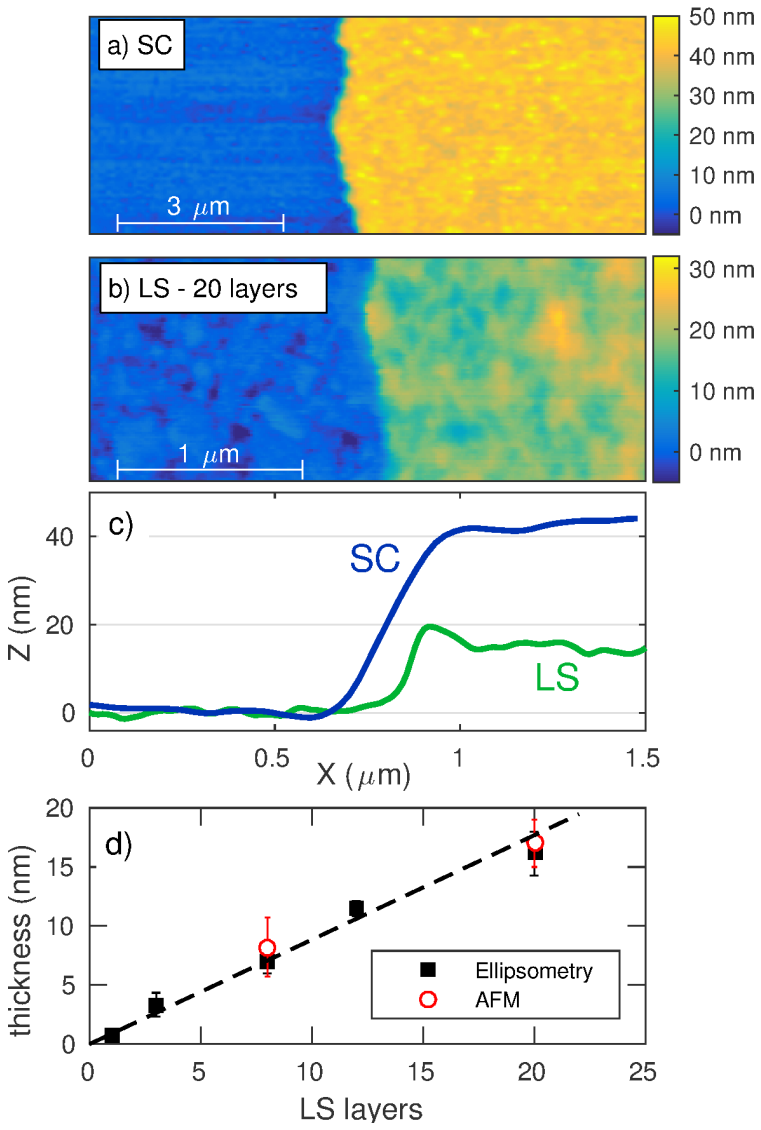

Figure 55: Characterisation of the thickness of the two samples, using AFM and Null-Ellipsometry. a) AFM image of a spin-coated sample, in a region where the film was scratched; the film is approx. 40 nm thick. b) AFM image of 20 Langmuir layers of sample, in a region where the film was scratched. c) height profiles of SC and LS samples, measured along the black segments shown in panels a)-b). d) thickness of LS samples deposited on gold substrate as for increasing number of layers deposited. Error-bars are standard deviations over several regions of the same film, and over different samples. The dashed line is a linear fit to the data, yielding a thickness-per-layer of (0.9 ± 0.1) nm.

9.5.1 Protocol A

- Potentiostatic preconditioning at 0.5 V for 1 min;
- Five Cyclic Voltammetry (CV) scans between 0 V and −1 V with a scan rate of $0.1\,\mathrm{V\,s^{-1}}$;
- Potentiostatic reduction at −0.90 V (chronoamperometry) until the current reached steady-state;
- Immersion in water at 90 °C – above the glass transition temperature (T_g) of PS-HOST – for 1 h.

9.5.2 Protocol B

This protocol avoids the preconditioning step and reduces the number of CV scans.

- Two CV scans between 0 V and −1 V with a scan rate of $0.1\,\mathrm{V\,s^{-1}}$;
- Potentiostatic reduction at −0.85 V (chronoamperometry) until the current reached steady-state;
- Immersion in water at 90 °C – above the T_g of PS-HOST – for 1 h.

10 Results and Discussion

The starting point was the electrochemical disassembly of complexes between *N*-methylpyridinium salts and phosphonate cavitands, previously known to be working in solution.[155] The one-electron reduction of the guest leads to a radical species with no affinity for the host, as shown in Fig. 56. Based on this foreknowledge, we reasoned that this approach could be appropriate to trigger polymer blend segregation in the solid state.

We have characterised the topography of films of the compatibilised polymers before and after the application of reducing electrochemical treatment, using

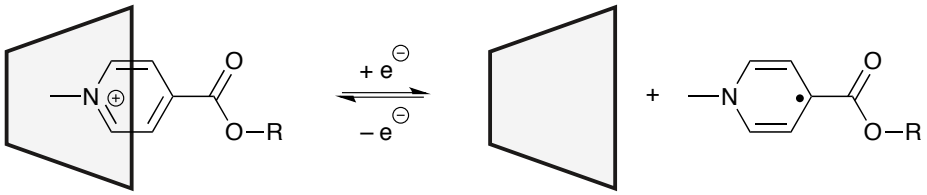

Figure 56: Schematic representation of the electrochemical activity of the *N*-methylpyridinium guest function for the guest function complexed by a phosphonate cavitand (schematically drawn as a trapezoid), which leads to decomplexation.

atomic force microscopy (AFM). By comparing the final morphology to that obtained using the pristine polymer blends, we can accurately check the degree of disassembly achieved.

Careful quantitative analysis of the morphology was used in order to assess the disassembly process. First, the typical morphology of a pristine PS-PBMA mixture, transferred on the gold substrate with our experimental conditions, was identified; An image is shown in Fig. 57a. In agreement with the literature[145], the morphology of the film consists of grains of irregular shape and low eccentricity. On the contrary, polymer functionalisation results in homogeneous surfaces in which no grains observed, as shown in Fig. 57b. In this case, the AFM topography shows a flat morphology in which the only features are those of the nanoscopic structure of the gold substrate (conformal roughness).

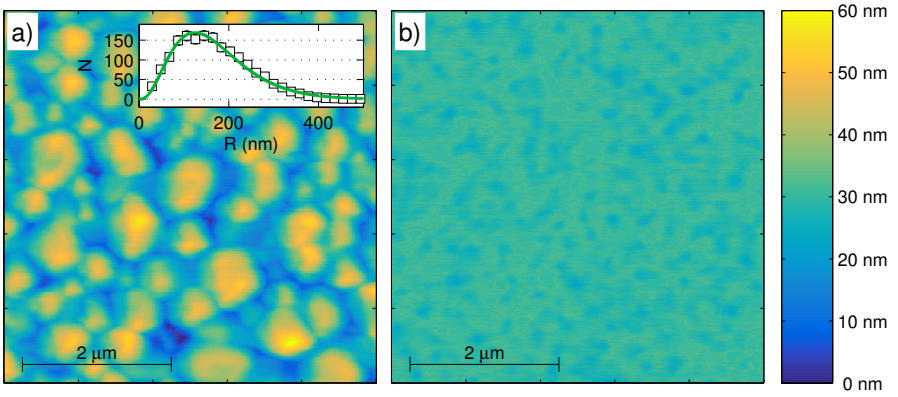

Figure 57: a) AFM topography of the phase-segregated morphology of a non-functionalised PS-PBMA solution, spin-coated on gold substrate. The inset shows the histogram of the features' radius R (points), fitted to a Gamma distribution (Eq. 12, solid green line). b) Topography of a functionalised PS-PBMA sample.

In the inset of Fig. 57a, a statistic of the equivalent radius R of the grains visible in unfunctionalised blends, obtained by the analysis of six 10 µm × 10 µm AFM images, is shown. The size distribution of those grains, characterised by pronounced skewness, could be well described by the Gamma distribution:

$$P(k,\theta;R) = \frac{1}{\Gamma(k)\theta^k} x^{k-1} e^{-x/\theta} \tag{12}$$

whose mean value is given by $\mu = k\theta$ and the standard deviation by $\sigma = k\theta^2$. The solid green line in the inset is the best fit to the data. Its mean value is $\mu = (169 \pm 12)$ nm and standard deviation is $\sigma = (87 \pm 5)$ nm.

Similar results are found using the same analysis on AFM images of spin-coated PS-PMMA (50 wt%-50 wt%, $M_w = 10000Da$ blend films on silicon

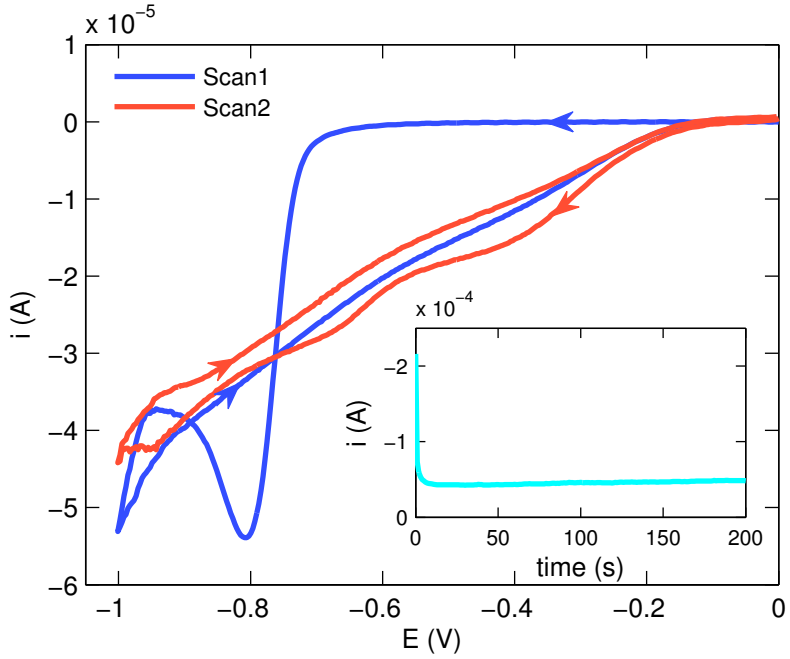

Figure 58: CV characterisation of a 20-cycles LS-deposed film. Inset: chronoamperogram recorded upon potentiostatic reduction at −0.85 V.

wafers[146]; a best fit of the radii distribution of the almost-circular features observed yields $\mu_{PS-PMMA} = (177 \pm 50)$ nm and $\sigma_{PS-PMMA} = (99 \pm 20)$ nm.

To induce phase separation of the PS-HOST/PBMA-GUEST functionalised supported films, the electrochemical protocols described above were applied to induce separation of pyridinium guests from the cavitand hosts.

The LS-deposed PS-Host/PBMA-Guest coatings were initially characterised by cyclic voltammetry (CV) in order to investigate the reaction mechanism and the reversibility of the process. A strong cathodic signal, ascribable to reduction of the N-methylpiridinium (NMP^+) moieties of PBMA-GUEST, was recorded at −0.8 V in the first CV scan. This signal disappeared in the following scans, indicating the chemical irreversibility of the process. The voltammetric pattern is ascribable to a classical EC mechanism of the electrodic process, in which the electrodic reaction (E) is rapidly followed by chemical reaction (C). A mono-electronic transfer involving NMP^+ ions produces 1-methyl-1,4-dihydropyridinyl radicals, which undergo to a rapid dimerisation with bimolecular rate constant of about $1 \times 10^7\,\mathrm{M}^{-1}\,\mathrm{s}^{-1}$, as reported in literature [161]. On the basis of these results, a potentiostatic reduction at −0.85 V (Protocol B) was carried in order to achieve decompatibilisation. Figure 58 shows the CV characterisation of a 20-cycles LS-deposed film, evidencing that the reduction peak was observed only in the first scan. The chronoamperogram recorded upon potentiostatic

reduction at $-0.85\,\mathrm{V}$ is reported in the inset.

Protocol A was applied to SC samples; this causes the appearance of voids in the surface of the treated film: round portions of sample in which the height of the film is lower than half of the original average thickness. Interestingly, electrochemistry without the exposure to high temperature does not cause any measurable effect, indicating that it is necessary to increase the mobility of molecules to achieve phase separation. The required mobility is achieved by annealing at a temperature above the T_g of PS-HOST, which represents the component with the highest T_g in this system. As control measurements, exposure to this temperature without previous electrochemistry treatment was tested, as well as the application of electrochemistry without high temperature treatment: both do not cause any modification of surface of the film. Fig. 59a shows the comparison of the film as-cast with a film exposed to protocol A (EC+HT) and to the two control protocols, electrochemistry without high temperature (EC) and high temperature only (HT).

For LS films, due to their lower thickness and to the presence of vertical ordering imparted by the deposition process, the less-invasive Protocol B was sufficient to induce phase segregation and polymer migration, which causes the growth of features that closely resembles the ones found in the non-function alised sample, as shown in Fig. 59b. In this case, even in the absence of a heat treatment, electrochemistry is effective in inducing segregation. Further exposure of the treated sample to temperatures above the lass transition point of PS-HOST (90 °C for 1 h) increases the size and height of the features. Again, the thermal control protocol alone (*i.e.* in the absence of a previous EC cycle) does not affect the deposited sample.

In order to compare the morphology changes induced by polymer migration on SC and LS films and in the non-functionalised sample, the histograms of characteristic size of the observed features were calculated; the zero of the height was set to the mean value of the flat surface. The histograms are reported in Fig. 60; the size $\mathcal{W}$ of bins in each histogram has been calculated using the Freedman-Diaconis rule[162]:

$$\mathcal{W}(x) = 2irq(x)n^{-\frac{1}{3}} \tag{13}$$

where irq is the interquartile range of the data and n the number of observations.

The data in Fig. 60 has been fitted to the Gamma distribution (Eq. 12), already used to characterise the size distribution of features in the film of immiscible copolymers. Mean value and variance of the fits are reported in Table 2; in panel a) the best fit values of the distribution of heights, in panel b) those of the distribution of radii.

The average effect of the electrochemistry protocols and control tests on the surface can be estimated by measuring the root mean square roughness of the surface of several portions of many different films; results are reported as an histogram in Fig. 61. In both cases, the driving force is phase segregation and polymer long range migration. In spin coated samples, the limited depth and

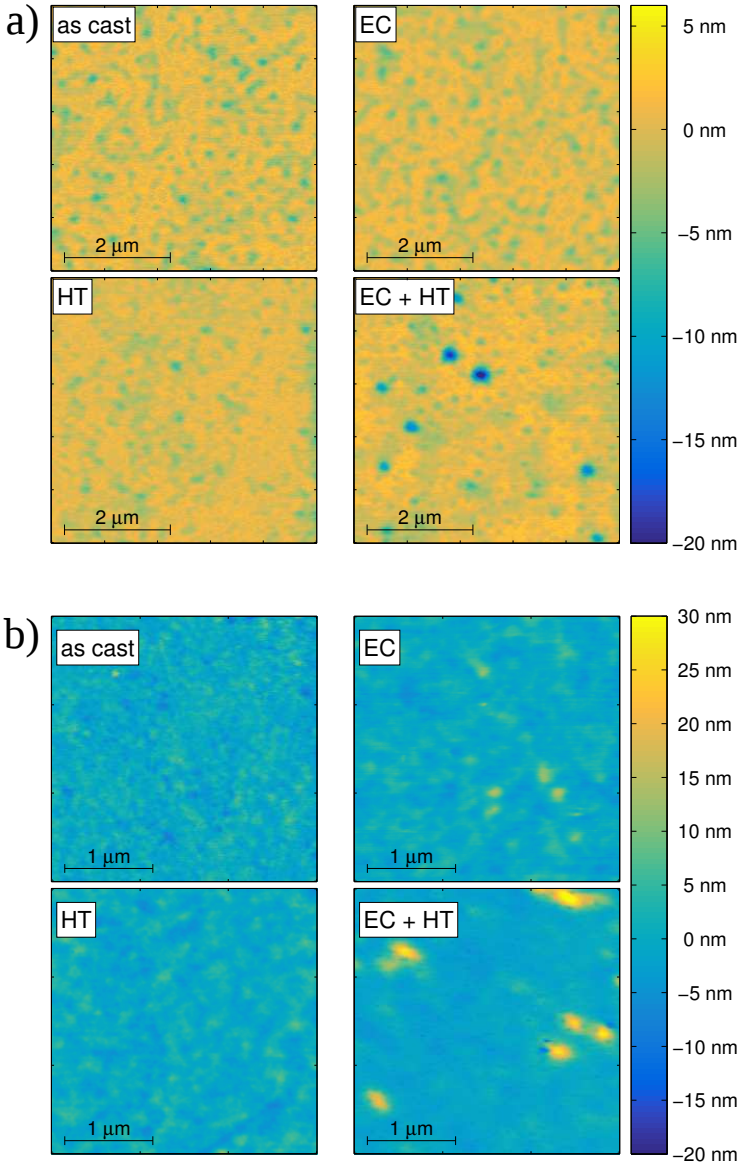

Figure 59: Comparison of typical AFM topography images of a) SC and b) LS deposited samples, as cast and after the three steps of sample treatment: high temperature (HT), electrochemistry cycle (EC), electrochemistry followed by exposure to high temperature (EC+HT). Colour-bars indicate the height of the sample with respect to the median height, set to zero.

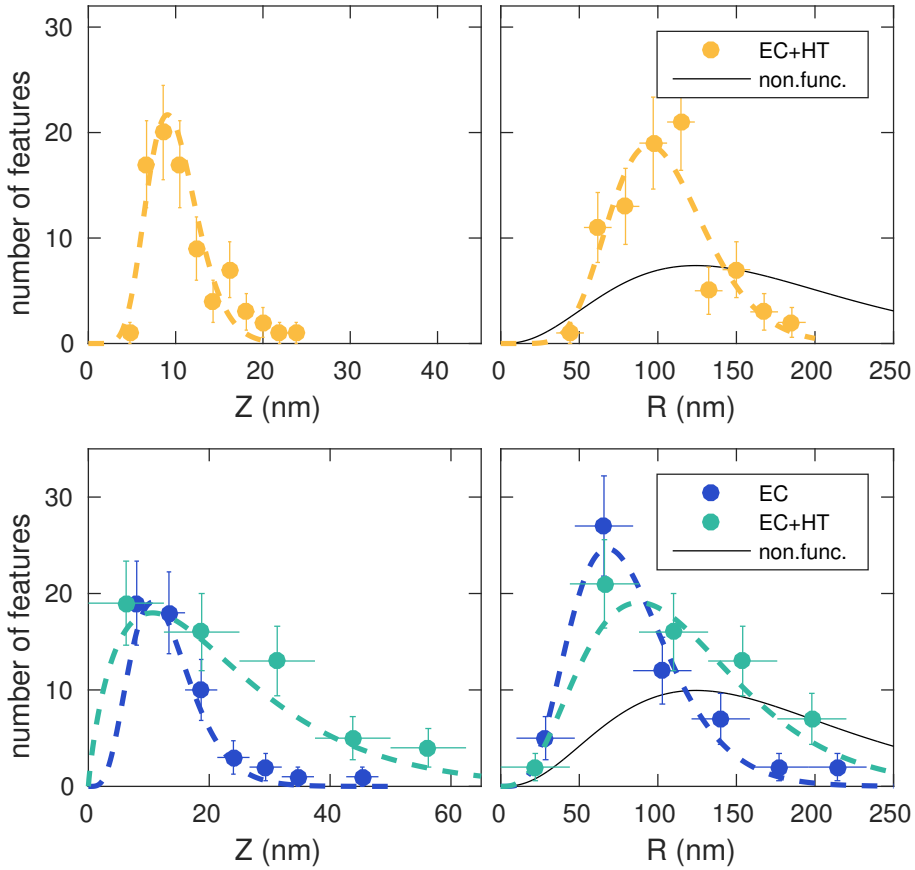

Figure 60: Electrochemistry can be used to induce phase segregation and hence lateral migration of the polymer, which causes the formation either of voids or of grains on the surface of the blend films. Top: Histogram of depth Z and radius R of voids produced in the film surface of Spin coated films by electrochemistry followed by exposure to high-T. Bottom: Histogram of height Z and radius R of the grains observed in Langmuir-Schaefer films by electrochemistry (blue) and electrochemistry followed by high-T treatment. Vertical error-bars are the square root of the counts, horizontal bars indicate the width of the bins. Dashed lines are fits to Eq. 12, while black solid lines are the distribution of features in the non-functionalised sample.

Table 2: Mean value μ and standard deviation σ of the distributions reported in Fig. 60 and fitted using Eq. 12. Panel a) refers to the distributions of depth/height Z of voids/grains in LC and LS samples respectively. Panel b) refers to the radius R of voids/grains; for the sake of comparison, the values found on the non-functionalised samples are reported in the last row.

(a) Best fits of the distribution of heights.

Sample	Treatment	μ(Z) /nm	σ(Z) /nm
SC	EC + HT	10.0 ± 4.1	2.9 ± 0.9
LS	EC	12.9 ± 7.5	5.4 ± 2.3
LS	EC + HT	23 ± 10	16 ± 8

(b) Best fits of the distribution of radii.

Sample	Treatment	μ(R) /nm	σ(R) /nm
SC	EC + HT	104 ± 50	31 ± 11
LS	EC	81 ± 34	33 ± 11
LS	EC + HT	115 ± 67	55 ± 25
Non-functionalised		167 ± 12	87 ± 5

size of the features induced by protocol A do not cause any measurable change in the roughness of the film, compared to the value found in the as-cast sample. This is also due to the fact that the surface density of features is low. On the other hand, in LS films treated following protocol B show that the RMS roughness doubles, due to the large value of height and surface density of the features.

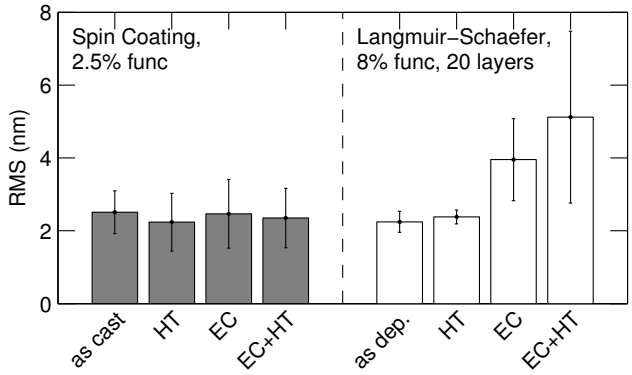

Figure 61: The appearance of grains after the electrochemical treatment causes an increase of average roughness in the LS sample, while the roughness of the spin-coated one remains unchanged. Each bars represent the average roughness of samples subject to different treatments, calculated from the analysis of 16 or more images; error bars are standard deviations.

11 Conclusions

This work demonstrated important morphological changes due to solid-state decompatibilisation of a supramolecularly stabilised polymer blend; this is achieved by means of electrochemical stimulus. The electrochemical PS-HOST/PDMA-GUEST segregation has been thoroughly investigated by AFM microscopy and detailed statistical analysis of the resulting morphologies: starting from a previously homogeneous and flat morphology, we observe long range migration of the polymers resulting in the formation of retreats and accumulations. This holds true both for the Langmuir-Schaefer films and the spin coated ones. The main difference between the two types of films is that the Langmuir-Schaefer films, due to the layered deposition process, are typical 2D structures- They are homogeneous only in the lateral direction, with little or no entanglements between polymer chains belonging to different stacks. On the contrary, spin cast films are supposed to be homogeneous in all the directions, and in particular the polymer chains are entangled to form 3D structures as in the bulk. This difference explains why in the Langmuir-Schaefer films we observe a more pronounced effect, than in the spin coated film: in the former, morphology rearrangement is triggered by the electrochemical stimulus alone, with no need for the subsequent temperature treatment above the T_g, which is needed for the latter. We speculate that this is due to enhanced mobility of the polymeric backbones in the Langmuir-Schaefer films is due to their less entangled initial state. This correlates with the well known effect of lowering of the T_g in thin films either free standing[163] or with unfavourable interaction with the substrate [164] which clearly corresponds to accelerated dynamics [165]. This also suggests that other layered structures, produced by the LS technique or by the layer-by-layer technique in the case of polyelectrolites, could give even more sensitive systems.

12 Additional characterisation

12.1 DSC analysis

For PS and PS-HOST, the samples were heated from 30 °C to 150 °C (10 °C min^{-1} as rate), followed by cooling from 150 °C to 30 °C (rate of 20 °C min^{-1}), isotherm at 30 °C for 3 min and another heating until 150 °C. For PBMA and PBMA-GUEST, instead, the heating steps are from −30 °C to 150 °C. (10 °C min^{-1}), cooling from 150 °C to −30 °C with rate of 20 °C min^{-1} and isotherm at −30 °C for 3 min. In the following values were obtained:

Table 3: Polymers and their blends analysed by differential scanning calorimetry (DSC).

Components (molar ratio)	T_g $^{\circ}C^{-1}$
PS	95
PS-HOST-2.5 %	97
PBMA	26
PBMA-GUEST-2.5 %	20
PS/PBMA (1:1)	25/97
PS-HOST-2.5 %/PBMA-GUEST-2.5 %	56

Bibliography

[1] Nič, M.; Jirát, J.; Košata, B.; Jenkins, A.; McNaught, A. *IUPAC Compendium of Chemical Terminology*; IUPAC: Research Triagle Park, NC, 2009.

[2] Pauling, L. *General chemistry*; Dover Publications, Inc: New York, 1988.

[3] Steed, J. W.; Atwood, J. L. *Supramolecular Chemistry*; Wiley, 2013.

[4] van der Waals, J. D.; Ph.d. thesis; Universiteit Leiden; 1873.

[5] Fischer, E. *Berichte der Dtsch. Chem. Gesellschaft* **1895**, *28*, 1429–1438.

[6] Moore, T. S.; Winmill, T. F. *J. Chem. Soc. Trans.* **1912**, *101*, 1635.

[7] Latimer, W. M.; Rodebush, W. H. *J. Am. Chem. Soc.* **1920**, *42*, 1419–1433.

[8] Kossel, W. *Ann. Phys.* **1916**, *354*, 229–362.

[9] Lewis, G. N. *J. Am. Chem. Soc.* **1916**, *38*, 762–785.

[10] Keesom, W. H. *Proc. Sect. Sci. K. Akad. van Wet. te Amsterdam* **1912**, *15*, 256–273.

[11] Debye, P. *Phys. Zeitschrift* **1912**, *13*, 97–100.

[12] Meyer, E. A.; Castellano, R. K.; Diederich, F. *Angew. Chemie Int. Ed.* **2003**, *42*, 1210–1250.

[13] Feynman, R. P. *Eng. Sci.* **1960**, *23*, 22–36.

[14] Lehn, J.-M. *Supramolecular Chemistry*; Wiley-VCH Verlag GmbH & Co. KGaA: Weinheim, 1995.

[15] Lehn, J. M.; Sauvage, J. P. *J. Am. Chem. Soc.* **1975**, *97*, 6700–6707.

[16] Kang, S. O.; Llinares, J. M.; Day, V. W.; Bowman-James, K. *Chem. Soc. Rev.* **2010**, *39*, 3980.

[17] Saenger, W.; Jacob, J.; Gessler, K.; Steiner, T.; Hoffmann, D.; Sanbe, H.; Koizumi, K.; Smith, S. M.; Takaha, T. *Chem. Rev.* **1998**, *98*, 1787–1802.

[18] Del Valle, E. *Process Biochem.* **2004**, *39*, 1033–1046.

[19] Crini, G. *Chem. Rev.* **2014**, *114*, 10940–10975.

[20] Böhmer, V. *Angew. Chemie Int. Ed. English* **1995**, *34*, 713–745.

[21] Gutsche, C. D. *Calixarenes*; Monographs in Supramolecular Chemistry; Royal Society of Chemistry: Cambridge, 2008.

[22] Cram, D. J. *Science* **1983**, *219*, 1177–1183.

[23] Lippmann, T.; Dalcanale, E.; Mann, G. *Tetrahedron Lett.* **1994**, *35*, 1685–1688.

[24] Delangle, P.; Dutasta, J.-P. *Tetrahedron Lett.* **1995**, *36*, 9325–9328.

[25] Dutasta, J.-P. In *New Asp. Phosphorus Chem. IV*; Springer Berlin Heidelberg, 2004; pp 55–91.

[26] Pinalli, R.; Suman, M.; Dalcanale, E. *Eur. J. Org. Chem.* **2004**, *2004*, 451–462.

[27] Freeman, W. A.; Mock, W. L.; Shih, N. Y. *J. Am. Chem. Soc.* **1981**, *103*, 7367–7368.

[28] Kim, J.; Jung, I.-S.; Kim, S.-Y.; Lee, E.; Kang, J.-K.; Sakamoto, S.; Yamaguchi, K.; Kim, K. *J. Am. Chem. Soc.* **2000**, *122*, 540–541.

[29] Day, A.; Arnold, A. P.; Blanch, R. J.; Snushall, B. *J. Org. Chem.* **2001**, *66*, 8094–8100.

[30] Day, A. I.; Blanch, R. J.; Arnold, A. P.; Lorenzo, S.; Lewis, G. R.; Dance, I. *Angew. Chemie Int. Ed.* **2002**, *41*, 275–277.

[31] Masson, E.; Ling, X.; Joseph, R.; Kyeremeh-Mensah, L.; Lu, X. *RSC Adv.* **2012**, *2*, 1213–1247.

[32] Barrow, S. J.; Kasera, S.; Rowland, M. J.; del Barrio, J.; Scherman, O. A. *Chem. Rev.* **2015**, *115*, 12320–12406.

[33] Assaf, K. I.; Nau, W. M. *Chem. Soc. Rev.* **2015**, *44*, 394–418.

[34] Benvin, A. L.; Creeger, Y.; Fisher, G. W.; Ballou, B.; Waggoner, A. S.; Armitage, B. A. *J. Am. Chem. Soc.* **2007**, *129*, 2025–2034.

[35] Rood, M. T. M.; Spa, S. J.; Welling, M. M.; ten Hove, J. B.; van Willigen, D. M.; Buckle, T.; Velders, A. H.; van Leeuwen, F. W. B. *Sci. Rep.* **2017**, *7*, 39908.

[36] Freitag, M.; Yang, W.; Fredin, L. A.; D'Amario, L.; Karlsson, K. M.; Hagfeldt, A.; Boschloo, G. *ChemPhysChem* **2016**, *17*, 3845–3852.

[37] Chai, Z.-y.; Xie, Z.; Zhang, P.; Ouyang, X.; Li, R.; Gao, S.; Wei, H.; Liu, L.-h.; Shuai, Z.-j. *Chinese J. Polym. Sci.* **2016**, *34*, 850–857.

[38] Brunsveld, L.; Folmer, B. J. B.; Meijer, E. W.; Sijbesma, R. P. *Chem. Rev.* **2001**, *101*, 4071–4098.

[39] Chen, G.; Jiang, M. *Chem. Soc. Rev.* **2011**, *40*, 2254–2266.

[40] Yang, S. K.; Ambade, A. V.; Weck, M. *Chem. Soc. Rev.* **2011**, *40*, 129–137.

[41] Klok, H.-A.; Lecommandoux, S. *Adv. Mater.* **2001**, *13*, 1217–1229.

[42] Pitet, L. M.; van Loon, A. H. M.; Kramer, E. J.; Hawker, C. J.; Meijer, E. W. *ACS Macro Lett.* **2013**, *2*, 1006–1010.

[43] Wu, D. Y.; Meure, S.; Solomon, D. *Prog. Polym. Sci.* **2008**, *33*, 479–522.

[44] van Gemert, G. M. L.; Peeters, J. W.; Söntjens, S. H. M.; Janssen, H. M.; Bosman, A. W. *Macromol. Chem. Phys.* **2012**, *213*, 234–242.

[45] Herbst, F.; Döhler, D.; Michael, P.; Binder, W. H. *Macromol. Rapid Commun.* **2013**, *34*, 203–220.

[46] Jain, A.; George, S. J. *Mater. Today* **2015**, *18*, 206–214.

[47] Peurifoy, S. R.; Guzman, C. X.; Braunschweig, A. B. *Polym. Chem.* **2015**, *6*, 5529–5539.

[48] Zhou, T.-Y.; Qi, Q.-Y.; Zhao, Q.-L.; Fu, J.; Liu, Y.; Ma, Z.; Zhao, X. *Polym. Chem.* **2015**, *6*, 3018–3023.

[49] Clough, J. M.; Balan, A.; Sijbesma, R. P. In *Polym. Mechanochemistry*; Springer International Publishing, 2015; pp 209–238.

[50] Black, A. L.; Lenhardt, J. M.; Craig, S. L. *J. Mater. Chem.* **2011**, *21*, 1655–1663.

[51] Li, J.; Nagamani, C.; Moore, J. S. *Acc. Chem. Res.* **2015**, *48*, 2181–2190.

[52] Pucci, A.; Bizzarri, R.; Ruggeri, G. *Soft Matter* **2011**, *7*, 3689–3700.

[53] Ciardelli, F.; Ruggeri, G.; Pucci, A. *Chem. Soc. Rev.* **2013**, *42*, 857–870.

[54] Lee, C. K.; Davis, D. A.; White, S. R.; Moore, J. S.; Sottos, N. R.; Braun, P. V. *J. Am. Chem. Soc.* **2010**, *132*, 16107–16111.

[55] O'Bryan, G.; Wong, B. M.; McElhanon, J. R. *ACS Appl. Mater. Interfaces* **2010**, *2*, 1594–1600.

[56] Davis, D. A.; Hamilton, A.; Yang, J.; Cremar, L. D.; Van Gough, D.; Potisek, S. L.; Ong, M. T.; Braun, P. V.; Martínez, T. J.; White, S. R.; Moore, J. S.; Sottos, N. R. *Nature* **2009**, *459*, 68–72.

[57] Klajn, R. *Chem. Soc. Rev.* **2014**, *43*, 148–184.

[58] Chen, Y.; Spiering, A. J. H.; Karthikeyan, S.; Peters, G. W. M.; Meijer, E. W.; Sijbesma, R. P. *Nat. Chem.* **2012**, *4*, 559–562.

[59] Clough, J. M.; Balan, A.; van Daal, T. L. J.; Sijbesma, R. P. *Angew. Chemie Int. Ed.* **2016**, *55*, 1445–1449.

[60] Chen, Y.; Sijbesma, R. P. *Macromolecules* **2014**, *47*, 3797–3805.

[61] Robb, M. J.; Li, W.; Gergely, R. C. R.; Matthews, C. C.; White, S. R.; Sottos, N. R.; Moore, J. S. *ACS Cent. Sci.* **2016**, *2*, 598–603.

[62] Rossi, N. A. A.; Duplock, E. J.; Meegan, J.; Roberts, D. R. T.; Murphy, J. J.; Patel, M.; Holder, S. J. *J. Mater. Chem.* **2009**, *19*, 7674.

[63] Yang, L.; Han, J. *Phys. Rev. Lett.* **2000**, *85*, 154–157.

[64] Leeuw, T. K.; Tsyboulski, D. A.; Nikolaev, P. N.; Bachilo, S. M.; Arepalli, S.; Weisman, R. B. *Nano Lett.* **2008**, *8*, 826–831.

[65] Zeng, S.; Zhang, D.; Huang, W.; Wang, Z.; Freire, S. G.; Yu, X.; Smith, A. T.; Huang, E. Y.; Nguon, H.; Sun, L. *Nat. Commun.* **2016**, *7*, 11802.

[66] Boyce, M. C.; Arruda, E. M. *Rubber Chem. Technol.* **2000**, *73*, 504–523.

[67] Fond, C. *J. Polym. Sci. Part B Polym. Phys.* **2001**, *39*, 2081–2096.

[68] Biavardi, E.; Favazza, M.; Motta, A.; Fragalà, I. L.; Massera, C.; Prodi, L.; Montalti, M.; Melegari, M.; Condorelli, G. G.; Dalcanale, E. *J. Am. Chem. Soc.* **2009**, *131*, 7447–7455.

[69] Menozzi, D.; Biavardi, E.; Massera, C.; Schmidtchen, F.-P.; Cornia, A.; Dalcanale, E. *Supramol. Chem.* **2010**, *22*, 768–775.

[70] Delangle, P.; Mulatier, J.-C.; Tinant, B.; Declercq, J.-P.; Dutasta, J.-P. *Eur. J. Org. Chem.* **2001**, *2001*, 3695–3704.

[71] Dionisio, M.; Ricci, L.; Pecchini, G.; Masseroni, D.; Ruggeri, G.; Cristofolini, L.; Rampazzo, E.; Dalcanale, E. *Macromolecules* **2014**, *47*, 632–638.

[72] Orsi, D.; Früh, A. E.; Giannetto, M.; Cristofolini, L.; Dalcanale, E. *Soft Matter* **2016**, *12*, 5353–5358.

[73] Biavardi, E.; Battistini, G.; Montalti, M.; Yebeutchou, R. M.; Prodi, L.; Dalcanale, E. *Chem. Commun.* **2008**, 1638–1640.

[74] Wang, P.; Yao, Y.; Xue, M. *Chem. Commun.* **2014**, *50*, 5064–5067.

[75] Shao, Y.; et al. *Phys. Chem. Chem. Phys.* **2006**, *8*, 3172–3191.

[76] Koh, K. N.; Araki, K.; Ikeda, A.; Otsuka, H.; Shinkai, S. *J. Am. Chem. Soc.* **1996**, *118*, 755–758.

[77] Zincke, T.; Heuser, G.; Möller, W. *Justus Liebig's Ann. der Chemie* **1904**, *333*, 296–345.

[78] Zincke, T. *Justus Liebig's Ann. der Chemie* **1904**, *330*, 361–374.

[79] Zincke, T.; Weißpfenning, G. *Justus Liebig's Ann. der Chemie* **1913**, *396*, 103–131.

[80] Moracci, F.; Liberatore, F.; Tortorella, S.; Di Rienzo, B. *Tetrahedron* **1979**, *35*, 809–812.

[81] Wu, Y.-L.; Tancini, F.; Schweizer, W. B.; Paunescu, D.; Boudon, C.; Gisselbrecht, J.-P.; Jarowski, P. D.; Dalcanale, E.; Diederich, F. *Chem. - An Asian J.* **2012**, *7*, 1185–1190.

[82] Yebeutchou, R. M.; Tancini, F.; Demitri, N.; Geremia, S.; Mendichi, R.; Dalcanale, E. *Angew. Chemie Int. Ed.* **2008**, *47*, 4504–4508.

[83] Pinalli, R.; Brancatelli, G.; Pedrini, A.; Menozzi, D.; Hernández, D.; Ballester, P.; Geremia, S.; Dalcanale, E. *J. Am. Chem. Soc.* **2016**, *138*, 8569–8580.

[84] Pinalli, R.; Dalcanale, E. *Acc. Chem. Res.* **2013**, *46*, 399–411.

[85] Moretto, H.-H.; Schulze, M.; Wagner, G. In *Ullmann's Encycl. Ind. Chem.*; Wiley-VCH Verlag GmbH & Co. KGaA: Weinheim, Germany, 2000.

[86] Misztal, K.; Tudisco, C.; Sartori, A.; Malicka, J. M.; Castelli, R.; Condorelli, G. G.; Dalcanale, E. *Eur. J. Inorg. Chem.* **2014**, *2014*, 2687–2694.

[87] Bibal, B.; Tinant, B.; Declercq, J.-P.; Dutasta, J.-P. *Supramol. Chem.* **2003**, *15*, 25–32.

[88] Lin, Y.; Hui, C. *Int. J. Fract.* **2004**, *126*, 205–221.

[89] Lev, Y.; Volokh, K. Y. *J. Appl. Mech.* **2016**, *83*, 044501.

[90] Jie, M.; Tang, C.; Li, Y.; Li, C. *Theor. Appl. Fract. Mech.* **1998**, *28*, 165–174.

[91] Kanninen, M. *Advanced fracture mechanics*; Oxford University Press: New York, 1985.

[92] Creager, M.; Paris, P. *Int. J. Fract. Mech.* **1967**, *3*.

[93] Rondeau, R. E. *J. Chem. Eng. Data* **1966**, *11*, 124–124.

[94] *FL WinLab*; 2001.

[95] Williams, T.; Kelley, C.; *gnuplot*; 2016.

[96] Blaber, J.; Adair, B.; Antoniou, A. *Exp. Mech.* **2015**, *55*, 1105–1122.

[97] Schneider, C. A.; Rasband, W. S.; Eliceiri, K. W. *Nat. Methods* **2012**, *9*, 671–675.

[98] Ehrenstein, G. W.; Kabelka, J. In *Ullmann's Encycl. Ind. Chem.*; Wiley-VCH Verlag GmbH & Co. KGaA: Weinheim, Germany, 2000.

[99] Drechsler, K.; Heine, M.; Mitschang, P.; Baur, W.; Gruber, U.; Fischer, L.; Öttinger, O.; Heidenreich, B.; Ltzenburger, N.; Voggenreiter, H. In *Ullmann's Encycl. Ind. Chem.*; Wiley-VCH Verlag GmbH & Co. KGaA: Weinheim, Germany, 2009.

[100] Johnson, D. J. *J. Phys. D. Appl. Phys.* **1987**, *20*, 286–291.

[101] Martín-Gomis, L.; Karousis, N.; Fernández-Lázaro, F.; Petsalakis, I. D.; Ohkubo, K.; Fukuzumi, S.; Tagmatarchis, N.; Sastre-Santos, Á. *Photochem. Photobiol. Sci.* **2017**, *16*, 596–605.

[102] Wang, S.; Singh, A.; Walsh, N.; Redmond, G. *Nanotechnology* **2016**, *27*, 245601.

[103] Ehli, C.; Oelsner, C.; Guldi, D. M.; Mateo-Alonso, A.; Prato, M.; Schmidt, C.; Backes, C.; Hauke, F.; Hirsch, A. *Nat. Chem.* **2009**, *1*, 243–249.

[104] Schuster, D. I.; Megiatto, J. D. *Nat. Chem.* **2009**, *1*, 182–183.

[105] Biver, T.; Criscitiello, F.; Di Francesco, F.; Minichino, M.; Swager, T.; Pucci, A. *RSC Adv.* **2015**, *5*, 65023–65029.

[106] Stevens, B.; Ban, M. I. *Trans. Faraday Soc.* **1964**, *60*, 1515–1523.

[107] Dixon, J. M.; Taniguchi, M.; Lindsey, J. S. *Photochem. Photobiol.* **2007**, *81*, 212–213.

[108] Hunger, K.; Herbst, W. In *Ullmann's Encycl. Ind. Chem.*; Wiley-VCH Verlag GmbH & Co. KGaA: Weinheim, Germany, 2000.

[109] Dodabalapur, A.; Katz, H. E.; Torsi, L. *Adv. Mater.* **1996**, *8*, 853–855.

[110] Ehli, C.; Ph.D. thesis; Friedrich-Alexander-Universität Erlangen-Nürnberg (FAU); 2009.

[111] Fitzer, E.; Foley, A.; Frohs, W.; Hauke, T.; Heine, M.; Jäger, H.; Sitter, S. In *Ullmann's Encycl. Ind. Chem.*; Wiley-VCH Verlag GmbH & Co. KGaA: Weinheim, Germany, 2012.

[112] Jones, F. R. *J. Adhes. Sci. Technol.* **2010**, *24*, 171–202.

[113] Pei, S.; Cheng, H.-M. *Carbon* **2012**, *50*, 3210–3228.

[114] Chua, C. K.; Pumera, M. *Chem. Soc. Rev.* **2014**, *43*, 291–312.

[115] Singh, R. K.; Kumar, R.; Singh, D. P. *RSC Adv.* **2016**, *6*, 64993–65011.

[116] Pei, S.; Zhao, J.; Du, J.; Ren, W.; Cheng, H.-M. *Carbon* **2010**, *48*, 4466–4474.

[117] Biedermann, F.; Uzunova, V. D.; Scherman, O. A.; Nau, W. M.; De Simone, A. *J. Am. Chem. Soc.* **2012**, *134*, 15318–15323.

[118] Jiao, D.; Geng, J.; Loh, X. J.; Das, D.; Lee, T.-C.; Scherman, O. A. *Angew. Chem.* **2012**, *124*, 9771–9775.

[119] Chen, H.; Yang, H.; Xu, W.-C.; Tan, Y.-B. *Chinese Chem. Lett.* **2013**, *24*, 857–860.

[120] Sun, S.; Li, F.; Liu, F.; Wang, J.; Peng, X. *Sci. Rep.* **2014**, *4*, 3570.

[121] Lee, L. G.; Chen, C.-H.; Chiu, L. A. *Cytometry* **1986**, *7*, 508–517.

[122] Nygren, J.; Svanvik, N.; Kubista, M. *Biopolymers* **1998**, *46*, 39–51.

[123] Xu, Y.; Guo, M.; Li, X.; Malkovskiy, A.; Wesdemiotis, C.; Pang, Y. *Chem. Commun.* **2011**, *47*, 8883–8885.

[124] Ernst, L. A.; Gupta, R. K.; Mujumdar, R. B.; Waggoner, A. S. *Cytometry* **1989**, *10*, 3–10.

[125] Pisoni, D. S.; Todeschini, L.; Borges, A. C. A.; Petzhold, C. L.; Rodembusch, F. S.; Campo, L. F. *J. Org. Chem.* **2014**, *79*, 5511–5520.

[126] Nau, W. M.; Mohanty, J. *Int. J. Photoenergy* **2005**, *7*, 133–141.

[127] Zhegalova, N. G.; He, S.; Zhou, H.; Kim, D. M.; Berezin, M. Y. *Contrast Media Mol. Imaging* **2014**, *9*, 355–362.

[128] Bestvater, F.; Spiess, E.; Stobrawa, G.; Hacker, M.; Feurer, T.; Porwol, T.; Berchner-Pfannschmidt, U.; Wotzlaw, C.; Acker, H. *J. Microsc.* **2002**, *208*, 108–115.

[129] Corey, E.; Suggs, J. *Tetrahedron Lett.* **1975**, *16*, 2647–2650.

[130] Zimmermann, T.; Brede, O. *J. Heterocycl. Chem.* **2004**, *41*, 103–108.

[131] Gu, J.; Anumala, U. R.; Heyny-von Haußen, R.; Hölzer, J.; Goetschy-Meyer, V.; Mall, G.; Hilger, I.; Czech, C.; Schmidt, B. *ChemMedChem* **2013**, *8*, 891–897.

[132] Seko, T.; Ogura, K.; Kawakami, Y.; Sugino, H.; Toyotama, H.; Tanaka, J. *Chem. Phys. Lett.* **1998**, *291*, 438–444.

[133] Johnson, P.; Offen, H. *Chem. Phys. Lett.* **1973**, *18*, 258–260.

[134] Katoh, R.; Sinha, S.; Murata, S.; Tachiya, M. *J. Photochem. Photobiol. A Chem.* **2001**, *145*, 23–34.

[135] Biedermann, F.; Elmalem, E.; Ghosh, I.; Nau, W. M.; Scherman, O. A. *Angew. Chemie Int. Ed.* **2012**, *51*, 7739–7743.

[136] Defoin, A. *Synthesis* **2004**, 706–710.

[137] Nguyen, T. H. L.; Gigant, N.; Delarue-Cochin, S.; Joseph, D. *J. Org. Chem.* **2016**, *81*, 1850–1857.

[138] Puig de la Bellacasa, R.; Roué, G.; Balsas, P.; Pérez-Galán, P.; Teixidó, J.; Colomer, D.; Borrell, J. I. *Eur. J. Med. Chem.* **2014**, *86*, 664–675.

[139] Kitto, H. J.; Schwartz, E.; Nijemeisland, M.; Koepf, M.; Cornelissen, J. J. L. M.; Rowan, A. E.; Nolte, R. J. M. *J. Mater. Chem.* **2008**, *18*, 5615.

[140] Stuart, M. A. C.; Huck, W. T. S.; Genzer, J.; Müller, M.; Ober, C.; Stamm, M.; Sukhorukov, G. B.; Szleifer, I.; Tsukruk, V. V.; Urban, M.; Winnik, F.; Zauscher, S.; Luzinov, I.; Minko, S. *Nat. Mater.* **2010**, *9*, 101–113.

[141] Utracki, L. A. *Polym. Eng. Sci.* **1982**, *22*, 1166–1175.

[142] Heriot, S. Y.; Jones, R. A. L. *Nat. Mater.* **2005**, *4*, 782–786.

[143] Steiner, U.; Böltau, M.; Walheim, S.; Mlynek, J. J.; Krausch, G.; Boltau, M.; Walheim, S.; Mlynek, J. J.; Krausch, G.; Steiner, U. *Nature* **1998**, *391*, 877–879.

[144] Dalnoki-Veress, K.; Forrest, J. A.; Stevens, J. R.; Dutcher, J. R. *Physica A* **1997**, *239*, 87–94.

[145] Walheim, S.; Böltau, M.; Mlynek, J.; Krausch, G.; Steiner, U. *Macromolecules* **1997**, *30*, 4995–5003.

[146] Li, X.; Han, Y.; An, L. *Polymer* **2003**, *44*, 8155–8165.

[147] Wu, D.; Yuan, L.; Laredo, E.; Zhang, M.; Zhou, W. *Ind. Eng. Chem. Res.* **2012**, *51*, 2290–2298.

[148] Mao, C.; Zhu, Y.; Jiang, W. *ACS Appl. Mater. Interfaces* **2012**, *4*, 5281–5286.

[149] Göldel, A.; Kasaliwal, G. R.; Pötschke, P.; Heinrich, G. *Polymer* **2012**, *53*, 411–421.

[150] Chen, J.; Shi, Y.-y.; Yang, J.-h.; Zhang, N.; Huang, T.; Chen, C.; Wang, Y.; Zhou, Z.-w. *J. Mater. Chem.* **2012**, *22*, 22398–22404.

[151] Zhao, X.; Zhao, J.; Cao, J. P.; Wang, X.; Chen, M.; Dang, Z. M. *J. Phys. Chem. B* **2013**, *117*, 2505–2515.

[152] Park, T.; Zimmerman, S. C. *J. Am. Chem. Soc.* **2006**, *128*, 11582–11590.

[153] Feldman, K. E.; Kade, M. J.; de Greef, T. F. A.; Meijer, E. W.; Kramer, E. J.; Hawker, C. J. *Macromolecules* **2008**, *41*, 4694–4700.

[154] Feldman, K. E.; Kade, M. J.; Meijer, E. W.; Hawker, C. J.; Kramer, E. J. *Macromolecules* **2010**, *43*, 5121–5127.

[155] Gadenne, B.; Semeraro, M.; Yebeutchou, R. M.; Tancini, F.; Pirondini, L.; Dalcanale, E.; Credi, A. *Chem. Eur. J.* **2008**, *14*, 8964–8971.

[156] Masseroni, D.; Rampazzo, E.; Rastrelli, F.; Orsi, D.; Ricci, L.; Ruggeri, G.; Dalcanale, E. *RSC Adv.* **2015**, *5*, 11334–11342.

[157] Tompkins, H. G. *A user's guide to ellipsometry*; Academic Press, San Diego: Boston, 1993.

[158] Thermomicroscopes *Thermomicroscopes ProScan Image Processing Software*; Veeco Digital Instrument: Plainview, NY, 2000.

[159] Nečas, D.; Klapetek, P. *Open Phys.* **2012**, *10*, 181–188.

[160] Eco *GPES*; Eco Chemie B.V.: Utrecht, NL, 2004.

[161] Gaudiello, J. G.; Larkin, D.; Rawn, J.; Sosnowski, J. J.; Bancroft, E. E.; Blount, H. N. *J. Electroanal. Chem. Interfacial Electrochem.* **1982**, *131*, 203–214.

[162] Freedman, D.; Diaconis, P. *Z. Wahrscheinlichkeit* **1981**, *57*, 453–476.

[163] Forrest, J.; Dalnoki-Veress, K.; Stevens, J. R.; Dutcher, J. R. *Phys. Rev. Lett.* **1996**, *77*, 2002–2005.

[164] Keddie, J. L.; Jones, R. A. L.; Cory, R. A. *EPL* **1994**, *27*, 59–64.

[165] Cristofolini, L.; Arisi, S.; Fontana, M. P. *Phys. Rev. Lett.* **2000**, *85*, 4912–4915.

Appendices

A NMR titration of *N*-Methyl-5-(oct-1-yn-1-yl)-iso-quinolin-2-ium iodide and Tiiii[C_3H_7,CH_3,C_2H_5]

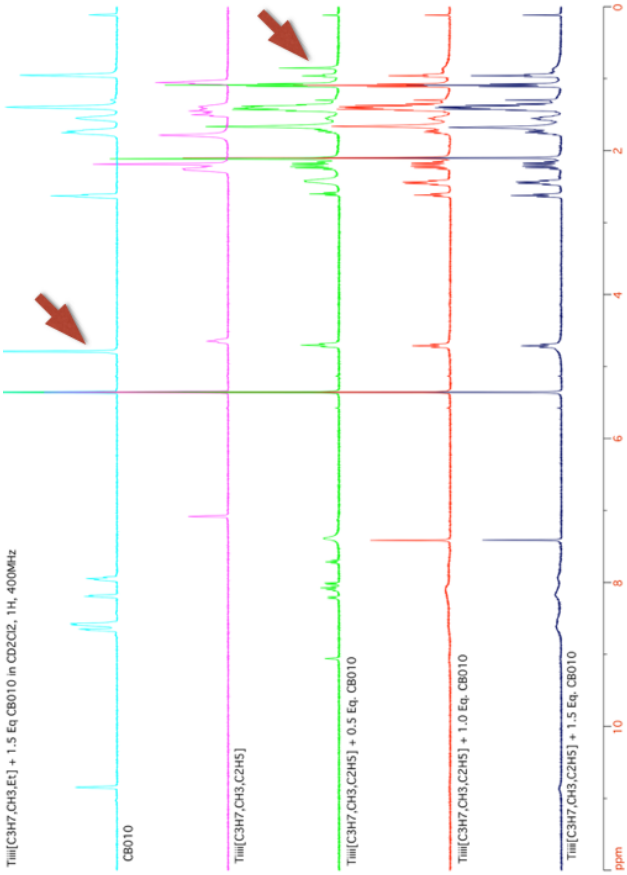

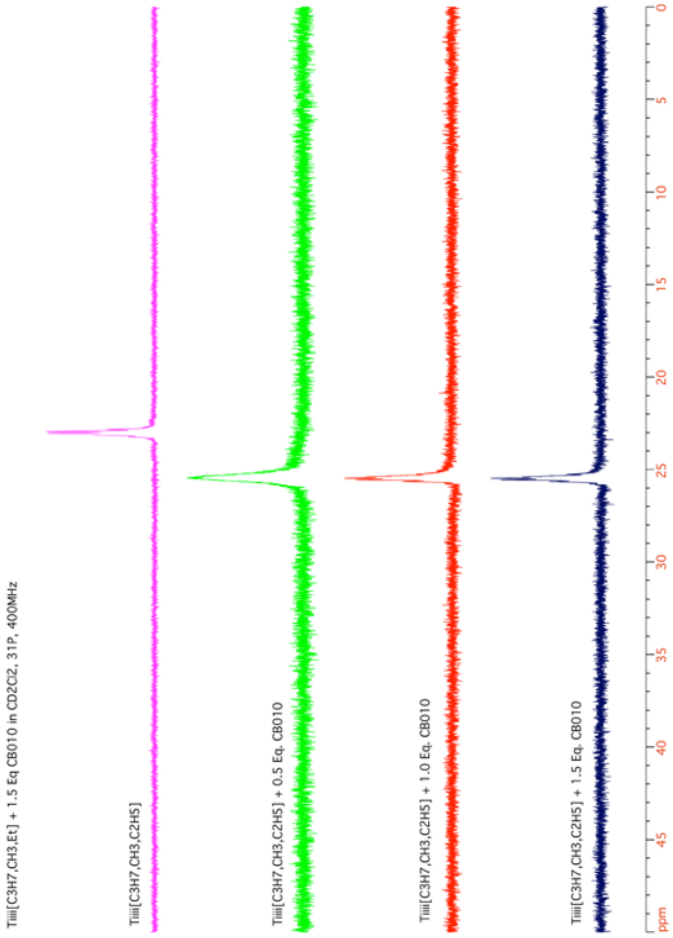
Tiii[C3H7,CH3,Et] + 1.5 Eq CB010 in CD2Cl2, 31P, 400MHz
Tiii[C3H7,CH3,C2H5]
Tiii[C3H7,CH3,C2H5] + 0.5 Eq. CB010
Tiii[C3H7,CH3,C2H5] + 1.0 Eq. CB010
Tiii[C3H7,CH3,C2H5] + 1.5 Eq. CB010
ppm
45
40
35
30
25
20
15
10
5
0

B NMR titrations of various guests with cavitands

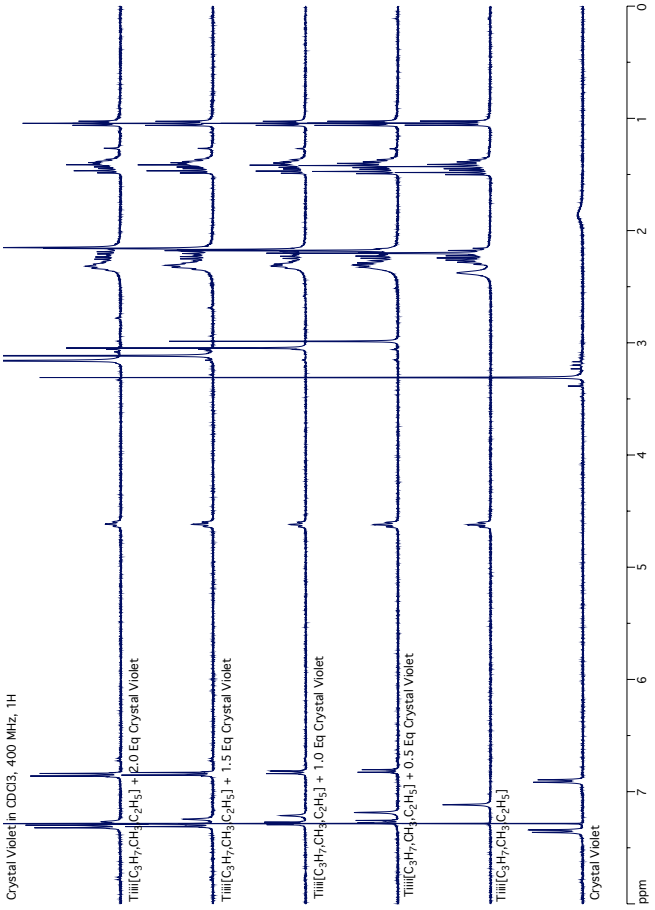

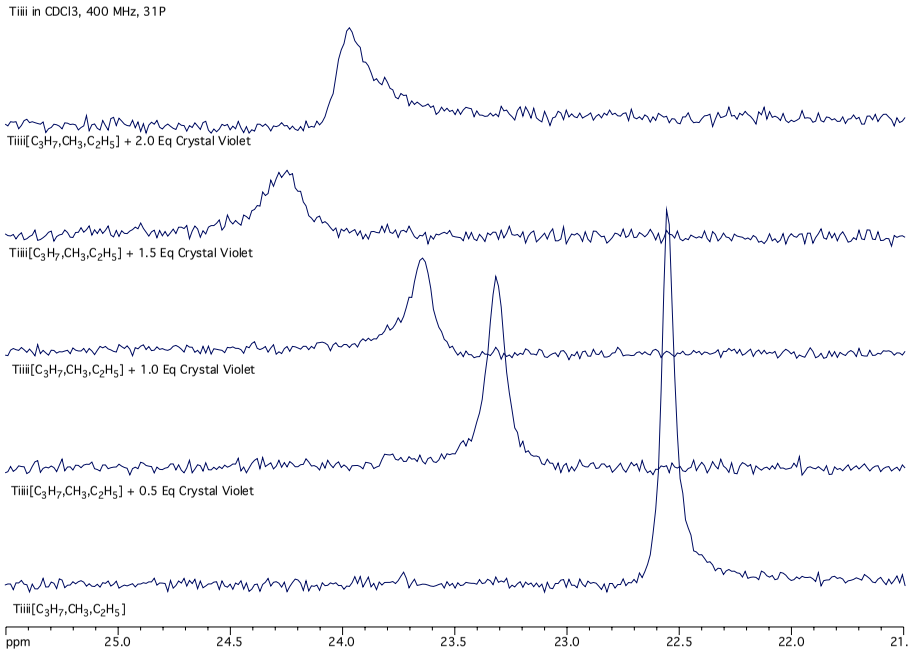
Tiii in CDCl3, 400 MHz, 31P
Tiiii[C3H7,CH3,C2H5] + 2.0 Eq Crystal Violet
Tiiii[C3H7,CH3,C2H5] + 1.5 Eq Crystal Violet
Tiiii[C3H7,CH3,C2H5] + 1.0 Eq Crystal Violet
Tiiii[C3H7,CH3,C2H5] + 0.5 Eq Crystal Violet
Tiiii[C3H7,CH3,C2H5]
ppm
25.0
24.5
24.0
23.5
23.0
22.5
22.0
21.

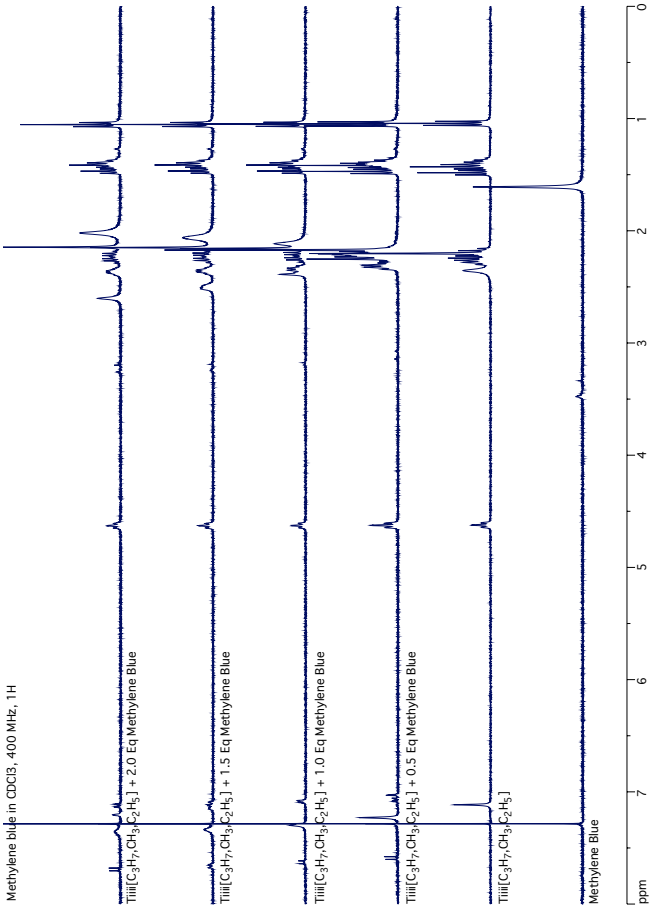
Methylene blue in CDCl3, 400 MHz, 1H
Tiiii[C3H7,CH3-C2H5] + 2.0 Eq Methylene Blue
Tiiii[C3H7,CH3-C2H5] + 1.5 Eq Methylene Blue
Tiiii[C3H7,CH3-C2H5] + 1.0 Eq Methylene Blue
Tiiii[C3H7,CH3-C2H5] + 0.5 Eq Methylene Blue
Tiiii[C3H7,CH3-C2H5]
Methylene Blue
ppm
7
6
5
4
3
2
1
0

Tiiii in CDCl3, 400 MHz, 31P
Tiiii[C3H7,CH3,C2H5] + 2.0 Eq Methylene Blue
Tiiii[C3H7,CH3,C2H5] + 1.5 Eq Methylene Blue
Tiiii[C3H7,CH3,C2H5] + 1.0 Eq Methylene Blue
Tiiii[C3H7,CH3,C2H5] + 0.5 Eq Methylene Blue
Tiiii[C3H7,CH3,C2H5]
ppm
25.5
25.0
24.5
24.0
23.5
23.0
22.5
22.

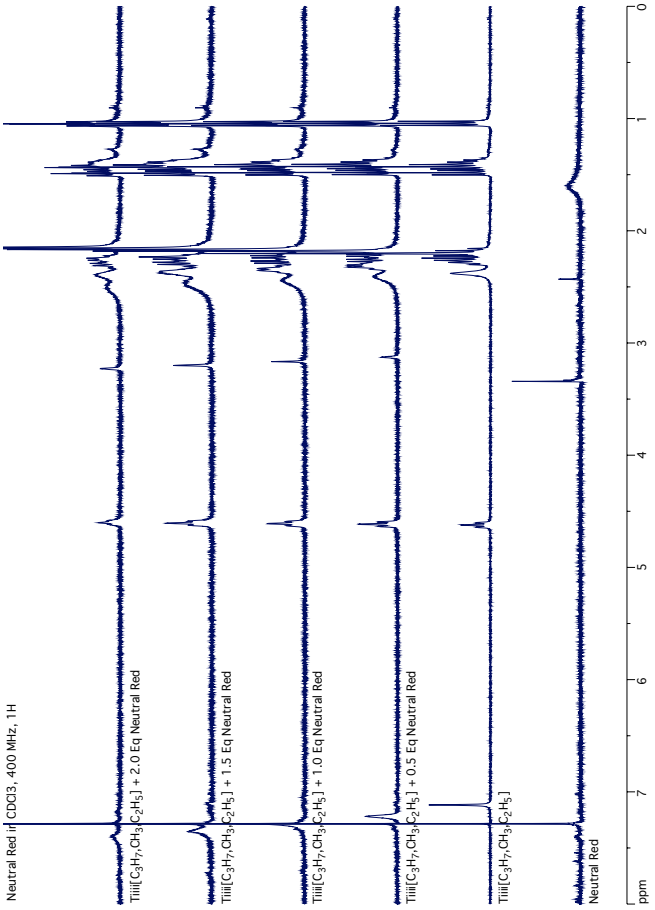
Neutral Red in CDCl3, 400 MHz, 1H
Tiiii[C3H7,CH3,C2H5] + 2.0 Eq Neutral Red
Tiiii[C3H7,CH3,C2H5] + 1.5 Eq Neutral Red
Tiiii[C3H7,CH3,C2H5] + 1.0 Eq Neutral Red
Tiiii[C3H7,CH3,C2H5] + 0.5 Eq Neutral Red
Tiiii[C3H7,CH3,C2H5]
Neutral Red
ppm
7
6
5
4
3
2
1
0

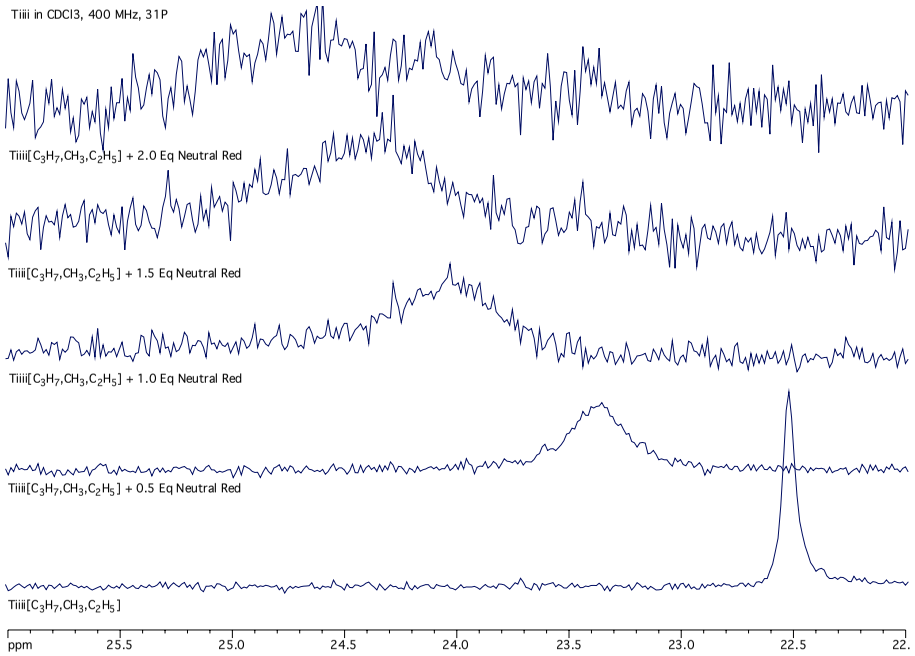
Tiii in CDCl3, 400 MHz, 31P
Tiii[C3H7,CH3,C2H5] + 2.0 Eq Neutral Red
Tiii[C3H7,CH3,C2H5] + 1.5 Eq Neutral Red
Tiii[C3H7,CH3,C2H5] + 1.0 Eq Neutral Red
Tiii[C3H7,CH3,C2H5] + 0.5 Eq Neutral Red
Tiii[C3H7,CH3,C2H5]
ppm
25.5
25.0
24.5
24.0
23.5
23.0
22.5
22.

C Fluorescence titrations of various guests with cavitands

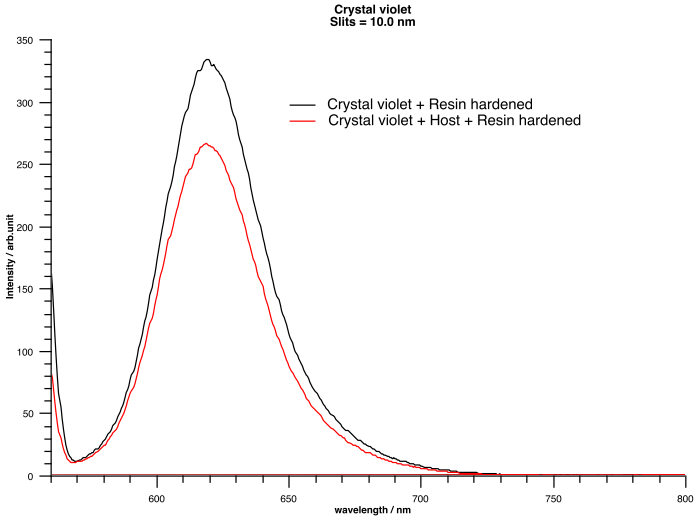

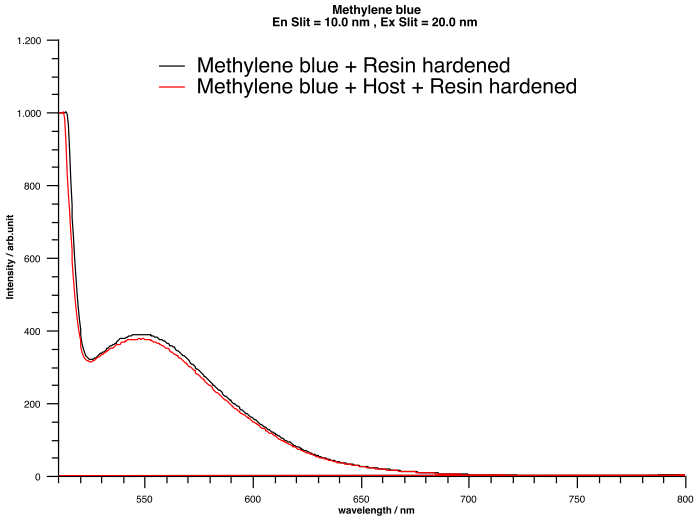

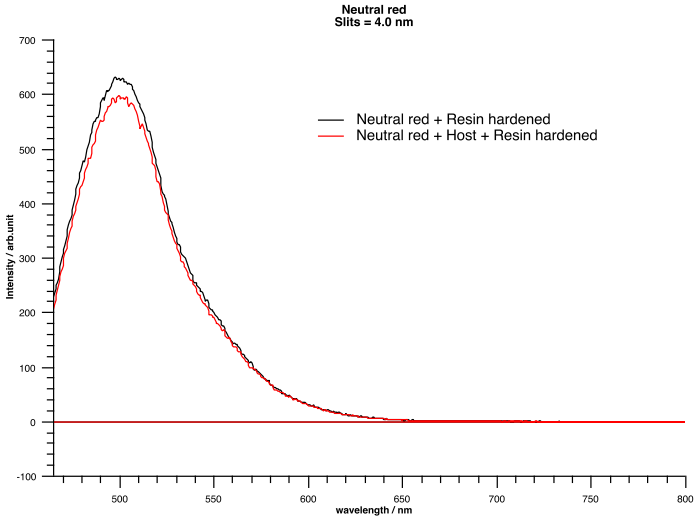
Neutral red
Slits = 4.0 nm
Neutral red + Resin hardened
Neutral red + Host + Resin hardened
Intensity / arb.unit
wavelength / nm
700
600
500
400
300
200
100
0
-100
500
550
600
650
700
750
800

D Data sheet for EC141NF/W241

ELANTAS

EN **Product Information**

Elan-tech®

EC 141 NF/W 241	**100:45**
EC 141 NF/W 242 NF	**100:45**

Epoxy system resistant to yellowing, protected with UV filters

ELANTAS Italia S.r.l.
Strada Antolini n°1 loc. Lemignano
43044 Collecchio (PR)
Italy
Tel +39 0521 304777
Fax +39 0521 804410
EEMEurope.ELANTAS@altana.com
info.elantas.italia@altana.com
www.elantas.com

A member of ALTANA

ELANTAS

Resin	Hardener	Mixing ratio by weight
EC 141 NF	**W 241**	**100:45**
	W 242 NF	**100:45**

Application: Castings and encapsulation which need true transparency and resistance to yellowing.

Processing: Manual casting. Under vacuum casting. Room temperature curing.
W 241: Maximum racommended thickness 100 mm.
W 242NF: Maximum racommended thickness 10 mm.

Description: Two component colourless, transparent epxy sistem. The system is based on a low viscosity unfilled resin and an amine hardener.
W 241: Long pot-life. Low exothermic peak. The system can be used for casting to a maximum of 3-5 cm on furniture/surface tops or casting to a maximum of 10 cm in thickness for a mass of 1 litre.
W 242NF: The product W 242NF is an accelerated version of the product W 241. The system can be used for casting to a maximum of 1 cm in thickness and for surface finishing (e.g. lenticular labels). Good resistance towards UV, however, exposure to UV for long time causes a yellowing of the material.

SYSTEM SPECIFICATIONS

Resin				
Viscosity at:	25°C	IO-10-50 (EN13702-2)	mPas	650 950
Hardener W 241				
Viscosity at:	25°C	IO-10-50 (EN13702-2)	mPas	180 300
Hardener W 242 NF				
Viscosity at:	25°C	IO-10-50 (EN13702-2)	mPas	250 350

TYPICAL SYSTEM CHARACTERISTICS

Resin					
Resin Colour				Colourless	
Density resin	25°C	IO-10-51 (ASTM D 1475)	g/ml	1,10 1,14	
Hardeners				**W 241**	**W 242 NF**
Hardener Colour				Colourless	Colourless
Density	25°C	IO-10-51 (ASTM D 1475)	g/ml	0,99 1,01	0,98 1,02
Processing Data					
Mixing ratio by weight		for 100 g resin	g	100:45	100:45
Mixing ratio by volume		for 100 ml resin	ml	100:50	100:50
					55 65
					45 55
Pot life (doubled initial viscosity)	25°C	O-10-50 (EN13702-2) (*)	min	75 95	35 45
					130 150
					170 190
Initial mixture viscosity at:	25°C		mPas	400 700	400 600
Gelation time	25°C (15ml;6mm)	IO-10-73 (*)	h	10 12	4 5
Gelation time	25°C 100ml	IO-10-52a (UNI 8701)	min	140 180	50 70
Demoulding time	25°C (15ml;6mm)	(*)	h	36 48	18 24
Post-curing	60°C	(**)	h	(15)	(15)

EC 141 NF

TYPICAL CURED SYSTEM PROPERTIES

Properties determined on specimens cured: 24 h TA + 15 h 60°C

			W 241		W 242 NF	
Colour			Colourless		Colourless	
Density 25°C	IO-10-54 (ASTM D 792)	g/ml	1,08	1,12	1,08	1,12
Hardness 25°C	IO-10-58 (ASTM D 2240)	Shore D/15	80	85	80	85
Glass transition (Tg)	IO-10-69 (ASTM D 3418)	°C	61	67	52	58
Water absorption (24h RT)	IO-10-70 (ASTM D 570)	%	0,15	0,25		
Water absorption (2h 100°C)	IO-10-70 (ASTM D 570)	%	0,95	1,15		
Max recommended operating temperature	(***)	°C	55		50	
Flexural strength	IO-10-66 (ASTM D 790)	MN/m²	90	102	69	78
Maximum strain	IO-10-66 (ASTM D 790)	%	4,0	5,5	3,5	5,5
Strain at break	IO-10-66 (ASTM D 790)	%	>	15	>	15
Flexural elastic modulus	IO-10-66 (ASTM D 790)	MN/m²	2.900	3.200	2.200	2.700
Tensile strength	IO-10-63 (ASTM D 638)	MN/m²	51	58	38	47
Elongation at break	IO-10-63 (ASTM D 638)	%	6,0	9,0	9	13

IO-00-00 = Elantas Italia's test method. The correspondent international method is indicated whenever possible.
nd = not determined na = not applicable RT = TA = laboratory room temperature (23±2°C)
Conversion units: 1 mPas = 1 cPs 1MN/m2 = 10 kg/cm2 = 1 MPa

(*) for larger quantities pot life is shorter and exothermic peak increases
(**) the brackets mean optionality
(***) The maximum operating temperature is given on the basis of laboratory information available being it function of the curing conditions used and of the type of coupled materials. For further possible information see post-curing paragraph.

EC 141 NF

Instructions: Add the appropriate quantity of hardener to the resin, mix carefully. Avoid air trapping. For some applications it can be useful to pre-heat the components and/or carry on a deaeration step under vacuum of the mixture before casting.

Curing / Post-curing: For a room temperature curing system post-curing allows fast stabilization of the material and obtainment of the best electrical and mechanical properties. During the curing process it is advisable to avoid thermal variations higher than 10°C/hour.

Storage: Epoxy resins and their hardeners can be stored for one year in the original sealed containers stored in a cool, dry place. The hardeners are moisture sensitive therefore it is good practice to close the vessel immediately after each use.

Handling precautions: Refer to the safety data sheet and comply with regulations relating to industrial health and waste disposal.

emission date: May 2012
revision n° 00

Manufactured: ELANTAS Italia S.r.l. Sito di Strada Antolini n°1, 43044 Collecchio (PR), Italy
www.elantas.com

A member of ALTANA

E Fluorescence microscope picture of self-diagnostic PDMS samples

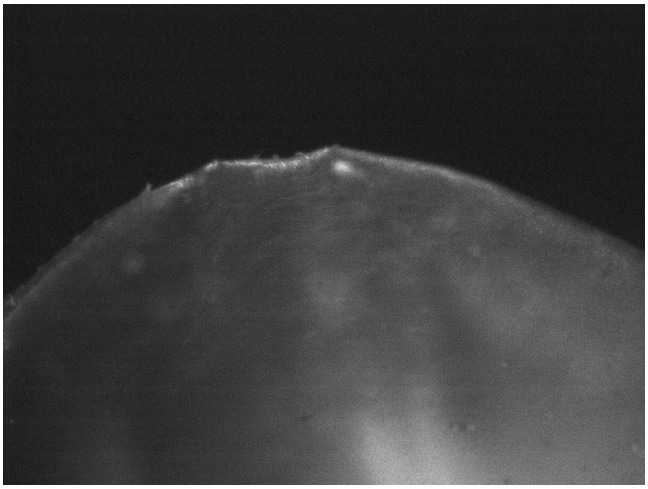

F Fluorescence microscope pictures of self-diagnostic samples containing CF-nanohybrids

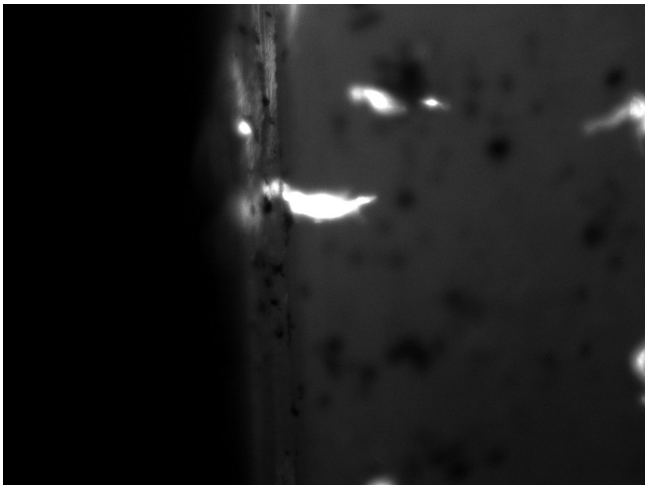

G Aborption spectrum of PyPyr

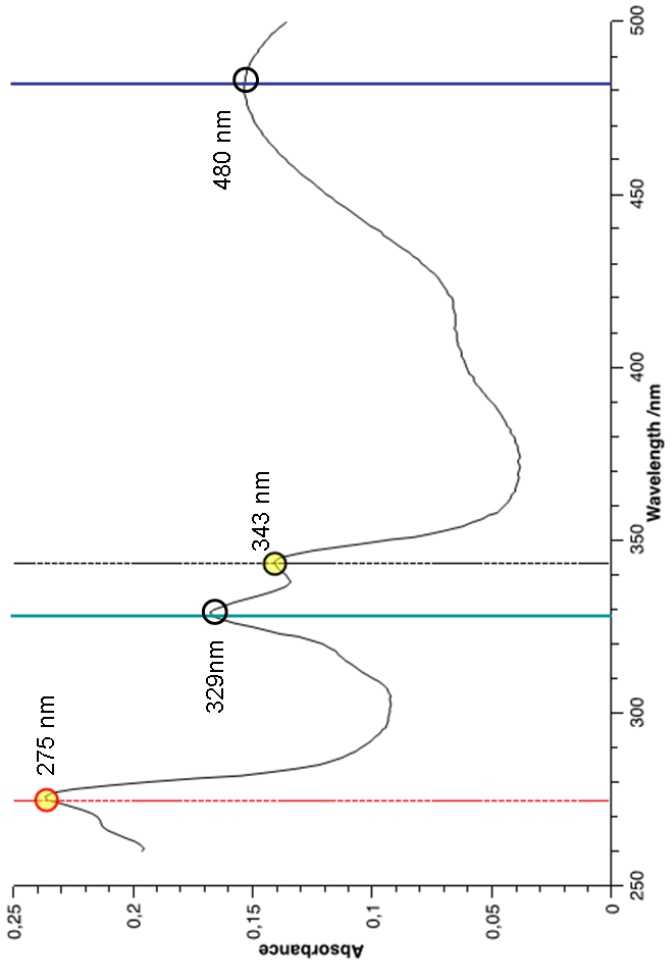

H Fluorescence microscope pictures of self-diagnostc samples containing (AB+Per)@CB[8]